Copyright Undertaking

This thesis is protected by copyright, with all rights reserved.

By reading and using the thesis, the reader understands and agrees to the following terms:

1. The reader will abide by the rules and legal ordinances governing copyright regarding the use of the thesis.
2. The reader will use the thesis for the purpose of research or private study only and not for distribution or further reproduction or any other purpose.
3. The reader agrees to indemnify and hold the University harmless from and against any loss, damage, cost, liability or expenses arising from copyright infringement or unauthorized usage.

If you have reasons to believe that any materials in this thesis are deemed not suitable to be distributed in this form, or a copyright owner having difficulty with the material being included in our database, please contact lbsys@polyu.edu.hk providing details. The Library will look into your claim and consider taking remedial action upon receipt of the written requests.

Pao Yue-kong Library, The Hong Kong Polytechnic University, Hung Hom, Kowloon, Hong Kong

http://www.lib.polyu.edu.hk

FABRICATION AND CHARACTERIZATION OF FERROELECTRIC FIELD EFFECT TRANSISTOR

SUBMITTED BY

SO KING SING

FOR THE DEGREE OF

MASTER OF PHILOSOPHY IN PHYSICS

AT

THE HONG KONG POLYTECHNIC UNIVERSITY

OCTOBER 2000

Pao Yue-Kong Library
PolyU • Hong Kong

ABSTRACT

Manganese oxide $La_{0.7}Sr_{0.3}MnO_3$ (LSMO) films and all-perovskite epitaxial $Pb(Zr_{0.52}Ti_{0.48})O_3$ (PZT)/$La_{0.7}Sr_{0.3}MnO_3$ heterostructure on single crystal $LaAlO_3$ (LAO) substrates have been fabricated by Pulsed Laser Deposition (PLD) method. It is found that the electrical transport properties of LSMO is very sensitive to the film's oxygen content, which can be tuned easily during deposition by controlling the ambient oxygen pressure. They are, however, very stable and remain unchanged in further thermal treatments. Epitaxial LSMO films are obtained at processing temperature as low as 500°C. Excellent crystalline quality of PZT(500 nm)/LSMO(40 nm) heterostructures have been realized. High remnant polarization (48 $\mu C/cm^2$), low coercive field (57 kV/cm), low polarization loss (~8% up to 2×10^9 switching cycles) and long retention ($>10^5$ s) are demonstrated for the ferroelectric PZT films. The leakage current in the Au/PZT/LSMO structure is about 5×10^{-7} A/cm^2. The results of both structural and electrical properties of PZT/LSMO heterostructures show that this material system is a suitable candidate for use in non-volatile ferroelectric field effect transistor (FeFET). A small remnant field effect modulation (5.6%) has been obtained and further optimizations in developing FeFET are using PZT/LSMO heterostructures suggested.

ACKNOWLEDGEMENTS

I would like to acknowledge Dr. K. H. Wong, for his close supervision, fruitful discussion and his enthusiasm in research during the past two years. I specially thank Dr. W. B. Wu, for giving me enlightening suggestions and helps in many experiments. I would also like to thank my research companions, Mr. Marcos Lam and Mr. K. M. Yeung, for their useful suggestions. I wish to thank Miss Yoyo Yeung and Dr. J. Wang for helping me in some electrical measurements. Special thanks should be given to Mr. M. N. Yeung for his assistance in SEM characterization. I also wish to thank Mr. T. L. Chan for his help in printing out this thesis. Finally, I would like to thank my brothers and sisters in Christ for their earnest prayers and encouragement. This project is supported by a research grant under code: B-Q213 of the Hong Kong Polytechnic University.

TABLE OF CONTENTS

ABSTRACT i

ACKNOWLEDGEMENTS ii

CHAPTER 1 INTRODUCTION 1

CHAPTER 2 PULSED LASER DEPOSITION (PLD) 5

2.1 Introduction 5

2.2 Historical development of the pulsed laser deposition 7

2.3 Mechanisms of pulsed laser deposition 9

CHAPTER 3 FERROELECTRIC MEMORY 14

3.1 Introduction 14

3.2 Conventional memory and ferroelectric memory 15

3.2.1 Random access memory (RAM) 15

3.2.2 From conventional RAM to non-volatile ferroelectric RAM 17

3.3 Theory of ferroelectric memory 19

3.3.1 Basic operation of MOSFET 19

3.3.2 Basic ferroelectric physics 21

3.3.3 Physics of ferroelectric capacitor 23

3.3.4 Physics of ferroelectric field effect transistor 24

CHAPTER 4 EXPERIMENTS AND SET-UP 28

4.1 Pulsed laser deposition (PLD) 28

4.1.1 The experimental set-up of PLD 28

4.1.2 Procedure of fabricating thin films by PLD 31

4.2 Sample characterization and measurements 32

4.2.1 Structural characterization 32

4.2.1.1 X-ray diffractometry (XRD) 32

4.2.1.2 Scanning electron microscope (SEM) 39

4.2.1.3 Thickness measurement 42

4.2.2 Electrical properties measurement 43

4.2.2.1 Resistivity–temperature measurement (R-T) 43

4.2.2.2 Hall effect measurement 49

4.2.2.3 Leakage current measurement 51

4.2.2.4 Polarization-voltage measurement, fatigue and retention test 51

4.2.2.5 Modulation 53

CHAPTER 5 FABRICATION AND STRUCTURAL CHARACTERIZATION OF LSMO/LAO AND PZT/LSMO/LAO HETEROSTRUCTURES 54

5.1 Target fabrication and characterization 54

5.2 Structural analysis of $La_{0.7}Sr_{0.3}MnO_3$ thin films 56

5.2.1 Substrate temperature dependence 56

5.2.2 Deposition oxygen pressure dependence 61

5.2.3 Post-annealing temperature effect 63

5.3 Structural characterization of $PbZr_{0.52}Ti_{0.48}O_3$ /$La_{0.7}Sr_{0.3}MnO_3$ heterostructures 65

5.4 Surface morphology analysis of $PbZr_{0.52}Ti_{0.48}O_3$ /$La_{0.7}Sr_{0.3}MnO_3$ heterostructures 70

CHAPTER 6 ELECTRICAL MEASUREMENTS OF LSMO/LAO AND PZT/LSMO/LAO HETEROSTRUCTURES 74

6.1 Electrical transport properties of LSMO films 74

6.2 Ferroelectric properties of the Au/PZT/LSMO heterostructures 84

6.2.1 Fabrication of Au/PZT/LSMO on LAO 84

6.2.2 Ferroelectric properties measurement 85

6.2.3 Other electrical properties of Au/PZT/LSMO heterostructures 93

CHAPTER 7 CONCLUSIONS AND FUTURE WORK 95

REFERENCES 98

CHAPTER 1

INTRODUCTION

In recent years, there is a great deal of interests in ferroelectric memory devices. Due to their unique properties of nonvolatility, fast switching and radiation hardness, this kind of memory devices is more desirable than their semiconductor counterparts. Ferroelectric dynamic random access memory (DRAM) consists of an array of many capacitors and their access transistor. By making use of the remnant polarization in the ferroelectric capacitor, the memory states "0" and "1" can be stored in the cell of memory. The charges stored in capacitor, however, are disturbed by interrogating the memory states. For this reason a different data storage mechanism based on ferroelectric field effect transistor (FeFET) are proposed [1]. In this FeFET the ferroelectric acts as the insulator. The polarization of the gate modifies the magnitude of the source-to-drain currents in the transistor, which permits a nondestructive read-out of the memory by interrogating the conductance of the semiconductor channel. In this way the FeFET is more superior than ferroelectric capacitor used in ferroelectric DRAM. Although ferroelectric FETs have been studied for a few years, an acceptable nonvolatile, nondestructive read memory with adequate retention and write-erase speed has not been demonstrated yet. It is attributed to the fact that the interface between a perovskite ferroelectric and a semiconductor such as silicon is difficult to control. Recently, some reports have proposed to use an epitaxial all-perovskite heterostructures. An improved gate channel interface and better FET performance are obtained.

In 1995, Watanabe [1] reported on a device in which $La_{2-x}Sr_xCuO_4$ was used as the semiconductor channel and a maximum modulation of 10% was achieved. This device exhibited a retention period of over 10 days at room temperature. Later, Ann *et al.* [2] reported on a device in which $Sr_{1-x}CuO_2$ was used as a semiconductor. Modulation of 3.5% and retention of only 10 min., were reported. In 1996, Ann *et al.* observed a ferroelectric field effect in the conducting oxide $SrRuO_3$ using $Pb(Zr_{0.52}Ti_{0.48})O_3/SrRuO_3$ epitaxial heterostructures. A 9% change in channel resistance was measured and this change was nonvolatile for a period of 3 days. In 1997, Mathews *et al.* [3] reported on a transistor in which $La_{0.7}Ca_{0.3}MnO_3$ (a doped rare-earth manganate with colossal magnetoresistance) was used as the semiconductor and $Pb(Zr_{0.2}Ti_{0.8})O_3$ as the ferroelectric gate. This device exhibited a modulation of 300% and a retention at room temperature on the order of hours. In all these studies, a pulse of low voltage (less than 10 volts) was usually applied to the ferroelectric thin film gate. It is clear that marked improvements in device performances have been obtained as compared with the previous ferroelectric FETs [4].

In the present study, ferroelectric field effect in epitaxial $Pb(Zr_{0.52}Ti_{0.48})O_3/La_{1-x}Sr_xMnO_3$ heterostructures on LAO single crystal substrate was investigated. The perovskite $La_{1-x}Sr_xMnO_3$ (LSMO) transforms from an antiferromagnetic insulator to a ferromagnetic metal as x increases to about 0.17. The carrier concentration of this material varies with both the La:Sr and oxygen content. LSMO was found to possess a high stability against post-deposition thermal treatment and can be grown at a

temperature as low as 500°C, which is compatible with the processing temperature in silicon technology. A sharp interface between the LSMO and $Pb(Zr_{0.52}Ti_{0.48})O_3$ PZT was observed due to the lattice matching of both materials. The detail of the PZT/LSMO heterostructures will be discussed in the following chapters.

Pulsed laser deposition (PLD) was used throughout to fabricate the aforesaid PZT/LSMO heterostructures with good structural properties on lattice-matched single crystal substrates. PLD has proved to be a very successful technique for growing oxides such as superconductor YBCO, ferroelectric PZT and other transition metal compounds, eg. LSMO. LSMO films with different carrier concentration can be grown by PLD with different partial oxygen pressure during the deposition process. Through our experimental investigations, we have identified the growth condition of epitaxial LSMO films. Subsequently PZT/LSMO and Au/PZT/LSMO heterostructures have been fabricated and their electrical properties such as the leakage current, hysteresis loop, modulation and retention have been examined.

A brief history and mechanism of pulsed laser deposition (PLD) will be presented in chapter 2. The advantages and limitations of PLD for fabricating high quality thin film will be discussed.

In chapter 3 the development of semiconductor memory and the transition from

conventional memory to ferroelectric memory will be discussed. The physics of ferroelectric memory and the principles of ferroelectric capacitor will be described. Several proposed ferroelectric FETs configuration will be defined. The motivation of the present work will also be explained.

The experimental set-up and instrumentation for PLD will be presented in chapter 4. The working principle of some major measuring and characterization equipment such as X-ray diffractometry (XRD) and four-point probe resistivity measurement will be described. Procedures for the fabrication of LSMO films as well as the PZT/LSMO heterostructures by PLD will be described.

In the following two chapters, the fabrication and characterization of LSMO and PZT/LSMO on single crystal LAO substrates will be described in details. Important results and major findings will be discussed and explained.

Conclusion of our present experimental results and suggestion for future investigation and development are will be presented in the last chapter of this report.

CHAPTER 2

PULSED LASER DEPOSITION (PLD)

2.1 Introduction

High precision, reliability and extreme small size are the crucial requirements in modern integrated circuit (IC) industry. According to the scaling rule, the thickness of device must be thin while photolithography, a patterning technology, provides a very small area device. For this reason, the interest and the number of researches in making thin film increase tremendously. Thin films can be produced by both chemical vapour deposition (CVD) and physical vapour deposition (PVD) methods.

CVD method, which involves chemical reaction between a carrier gas and an organometallic precursor, includes hydride CVD, trichloride CVD, and metal-organic CVD [5]. On the other hand, there are numerous methods of PVD such as electron-beam sputtering, ion-beam sputtering, magnetron sputtering [6, 7], thermal evaporation, molecular beam epitaxy (MBE) [8] and pulsed laser deposition (PLD). In the present study, we choose the pulsed laser deposition method to fabricate all our thin films and heterostructures.

Laser, a powerful tool in many applications, is especially useful in material

processing [9]. It possesses many unique properties such as narrow frequency bandwidth, coherence and high power density. Often the light beam is intense enough to vaporize the hardest and most heat resistant materials. Besides, due to its high precision, reliability and spatial resolution, it is widely used in the industry to process material like machining of the thin film, modification of materials, heat treatment, welding and micro-patterning. Apart from these, polycomponent materials can be ablated and deposited onto substrate to form stoichiometric thin films. It is the so-called pulsed laser deposition technique.

In general, the method of the pulsed laser deposition is simple. Only a few parameters need to be controlled during process. The equipment used in PLD system will be described in chapter 4. The targets used in PLD are small compared with the large size required for other sputtering techniques. It is quite easy to produce multi-layer film of different materials. Besides, by controlling the number of pulses, a fine control of film thickness can be achieved. Thus a fast response in exploiting new material system is a unique feature of PLD among other deposition methods. The most important feature of PLD is that the stoichiometry of the target can be retained in the deposited films. This is the result of the extremely high heating rate of the target surface (10^8 K/s) due to pulsed laser irradiation. It leads to the congruent evaporation of the target irrespective of the evaporating point of the constituent elements or compounds of the target. And because of the high heating rate of the ablated materials, laser deposition of crystalline film demands a much lower temperature than other mentioned

film growth techniques. For this reason the semiconductor and the underlying integrated circuit can refrain from thermal degradation.

In spite of the said advantages of PLD, some shortcomings have been identified in using this deposition technique. One of the major problems is the splashing or the particulates deposition on the film. The physical mechanisms leading to splashing include the surface boiling, expulsion of the liquid layer by shock wave recoil pressure and exfoliation. The size of particulates may be as large as a few microns. Such particulates will greatly affect the growth of the subsequent layers as well as the electrical properties of the film and should be eliminated. Another problem is the narrow angular distribution of the ablated species, which is generated by the adiabatic expansion of laser produced plasma plume and the pitting of the target surface. These features limit the use of PLD in producing a large area uniform thin film, and PLD has not been full deployed in industry. Recently remedial measures, such as inserting a shadow mask to block off the particulates and rotating both target and substrate in order to produce a larger uniform film, have been developed to minimize some of the PLD problems.

2.2 Historical development of the pulsed laser deposition

Albert Einstein postulated the stimulated emission process in as early as 1916. The first optical maser using a rod of ruby as the lasing medium was, however,

constructed in 1960 by Theodore H. Maiman at Hughes Research Laboratories, a lapse of 44 years. Using laser to ablate material has to be traced back to 1962 when Breech and Cross [10], used ruby laser to vaporize and excite atoms from a solid surface. Three years later, Smith and Turner [11] used ruby laser to deposit thin films. This marked the very beginning of the development of the pulsed laser deposition technique.

However, the development and investigations of pulsed laser deposition did not gather the expected momentum. In fact, the laser technology was immature at that time. The availability of the types of laser was limited; the stability output was poor and the laser repetition rate was too low for any realistic film growth processes. Thus the development of PLD in thin film fabrication was slow comparing with other techniques such as MBE, which can produce much better thin film quality.

The rapid progress of the laser technology [12, 13], however, enhanced the competitiveness of PLD in the following decade. The lasers having a higher repetition rate than the early ruby lasers made the thin film growth possible. Subsequently, reliable electronic Q-switches laser became available for generation of very short optical pulses. For this reason PLD can be used to achieve congruent evaporation of the target and to deposit stoichiometric thin films. The absorption depth is shallower for UV radiation. Subsequent development led to laser with high efficient harmonic generator and excimer lasers delivering UV radiation. From then on, non-thermal laser ablation of the target material became highly efficient.

Pulsed laser deposition as a film growth technique has attained its reputed fame and has attracted wide spread interest after it has been used successfully to grow high-temperature Tc superconducting films in 1987. During the late decade, pulsed laser deposition has been employed to fabricate crystalline thin films with epitaxy quality. Ceramic oxide, nitride films, metallic multilayers, and various superlattices grown by PLD have been demonstrated. Recently, using PLD to synthesis buckminster fullerness [14] and nanopowers have also been reported. Production-related issues concerning reproducibility [15], large-area scale-up [16] and multiple-level have begun to be addressed. It may start up another era of thin film fabrication in industry.

2.3 Mechanisms of pulsed laser deposition

The principle of pulsed laser deposition, in contrast to the simplicity of the system set-up, is a very complex physical phenomenon. It does not only involve the physical process of the laser-material interaction of the impact of high-power pulsed radiation on solid target, but also the formation plasma plume with high energetic species and even the transfer of the ablated material through the plasma plume onto the heated substrate surface. Thus the thin film formation process in PLD generally can be divided into the following four stages.

1. Laser radiation interaction with the target
2. Dynamic of the ablation materials

3. Deposition of the ablation materials with the substrate

4. Nucleation and growth of a thin film on the substrate surface

Each stage in PLD is critical to the formation of quality epitaxial crystalline, stoichiometric, uniform and small surface roughness thin film.

In the first stage, the laser beam is focused onto the surface of the target. At sufficiently high flux densities and short pulse duration, all elements in the target are rapidly heated up to their evaporation temperature. Materials are dissociated from the target surface and ablated out with stoichiometry as in the target. The instantaneous ablation rate is highly dependent on the fluences of the laser shining on the target. The ablation mechanisms involve many complex physical phenomena such as collisional, thermal, and electronic excitation, exfoliation and hydrodynamics.

During the second stage the emitted materials tend to move towards the substrate according to the laws of gas-dynamic and show the forward peaking phenomenon [17]. R. K. Singh [18] reported that the spatial thickness varied as a function of $cos\theta$. The spot size of the laser and the plasma temperature have significant effects on the deposited film uniformity. The target-to-substrate distance is another parameter that governs the angular spread of the ablated materials. Hanabusa [19] also found that a mask placed close to the substrate could reduce the spreading.

The third stage is important to determine the quality of thin film. The ejected high-energy species impinge onto the substrate surface and may induce various type of damage to the substrate. The mechanism of the interaction is illustrated in figure 2.1. These energetic species sputter some of the surface atoms and a collision region is formed between the incident flow and the sputtered atoms. Film grows after a thermalized region is formed. The region serves as a source for condensation of particles. When the condensation rate is higher than the rate of particles supplied by the sputtering, thermal equilibrium condition can be reached quickly and film grows on the substrate surface at the expenses of the direct flow of the ablation particles and the thermal equilibrium obtained.

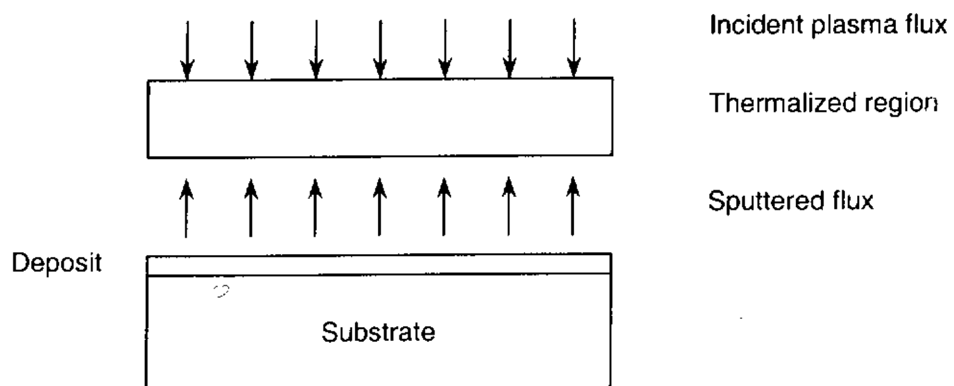

Figure 2.1 Schematic diagram of plasma-substrate interaction

Nucleation-and-growth of crystalline films depends on many factors such as the density, energy, ionization degree, and the type of the condensing material, as well as the temperature and the physico-chemical properties of the substrate. The two main thermodynamic parameters for the growth mechanism are the substrate temperature T

and the supersaturation Δm. They can be related by the following equation

$$\Delta m = kT\,ln(R/R_e)$$

where k is the Boltzmann constant, R is the actual deposition rate, and R_e is the equilibrium value at the temperature T.

The nucleation process depends on the interfacial energies between the three phases present – substrate, the condensing material and the vapour. The minimum-energy shape of a nucleus is like a cap. The critical size of the nucleus depending on the driving force, i.e. the deposition rate and the substrate temperature. For the large nuclei, a characteristic of small supersaturation, they create isolate patches (islands) of the film on the substrate which subsequently grow and coalesce together. As the supersaturation increases, the critical nucleus shrinks until its height reaches on atomic diameter and its shape is that of a two-dimensional layer. For large supersaturation, the layer-by-layer nucleation will happen for incompletely wetted foreign substrates.

The crystalline film growth depends on the surface mobility of the adatom (vapour atoms). Normally, the adatom will diffuse through several atomic distances before sticking to a stable position within the newly formed film. The surface temperature of the substrate determines the adatom's surface diffusion ability. High temperature favours rapid and defect free crystal growth, whereas low temperature or large supersaturation crystal growth may be overwhelmed by energetic particle impingement,

resulting in disordered or even amorphous structures.

Metev and Veiko [9, 20] suggested that the N_{99}, the mean thickness at which the growing, thin and discontinuous film reaches continuity is given by the formula

$$N_{99} = A(1/R)^{1/3} \exp(-1/T),$$

where R is the deposition rate (supersaturation related) and T is the temperature of the substrate and A is a constant related to the materials.

In the PLD process, due to the short laser pulsed duration (~10 ns) and hence the small temporal spread (≤10 μs) of the ablated materials, the deposition rate can be enormous (~10 μm/s). Consequently a layer-by-layer nucleation is favoured and ultra-thin and smooth film can be produced. In addition the rapid deposition of the energetic ablation species helps to raise the substrate surface temperature. In this respect PLD tends to demand a lower substrate temperature for crystalline film growth.

CHAPTER 3

FERROELECTRIC MEMORY

3.1 Introduction

Since the first bipolar transistor have been successfully fabricated in 1948 by Bardeen, Brattain and Shockley at the Bell Telephone Laboratories, the semiconductor industry was running in a very rapid pace in the following decades. Semiconductor device produced during the early 1960s, which marked the initial era of integrated circuit (IC), contained fewer than 30 transistors on a silicon die. These simple ICs were products of the small-scale integration (SSI) era. The pioneer in this field, Jack S. Kilby, is awarded the Nobel Prize in Physics of this year (2000). Following the fast development of lithographic technology, transistors became smaller from about 10 microns of SSI down to micron size, and the number of transistors per a single chip exceeded 1 million in the mid-1980s, the era of very-large-scale integration (VLSI). Nowadays, due to the introduction of deep ultraviolet (DUV) lithography, the device can be shrunk to sub-micron size, say 180 nm node for 248 nm UV source [21]. The devices down to 70 nm by using a shorter wavelength UV source lithography can be foreseen in the year of 2008 [21]. On the other hand, the development of copper interconnects and low k dielectric technologies are also fast in order to reduce RC delays of multilevel wiring that connects individual devices of silicon ICs [22]. They allow a very fast

response between devices. Therefore, with the lithographic technologies mentioned above, they will lead to smaller, faster and less power consumption devices in the coming future.

Semiconductor memory, which stores the digital signal "0" and "1", has been used in computer for several decades. It is basically divided into permanent memory, read only memory (ROM), in which the information is written at the time of manufacture, and the memory that allows temporary storage for reading/writing instructions and data from/to computer, read access memory (RAM). All of them are the product of ICs, and millions memory cells are bundled in a single IC chip. In this chapter, we will focus on the discussion of conventional memory, especially in RAM and nonvolatile memory, the so-called ferroelectric memory.

3.2 Conventional memory and ferroelectric memory

3.2.1 Random access memory (RAM)

RAM, becoming a common term in our daily life, is developing in the same pace with the computer technology. It provides great storage capacity for computer but is volatile. Also, it is utilized in a wide range of electronic products, for example, personal computer, electronic diary, hi-fi and digital camera. It consists of an array of memory cells, together with the logic circuit that specific contents in RAM can be accessed directly in a very short time regardless of the sequence in which they were recorded.

There are two types of RAM. They are static-random-access memory (SRAM) and dynamic random-access memory (DRAM), shown in figure 3a and 3b respectively, and primarily fabricated with metal-oxide semiconductor (MOS) technology.

In a SRAM chip, each memory cell consists of six transistors. The information in this memory is stored in a pair of cross-couple inverters. The inverter pair forms a "flip-flop", which force one inverter to be high potential while the other is low and vice versa. The memory logic state is determined by which of the two inverters is high. In a DRAM, however, each cell only consists of a single capacitor and a transistor. The charge stored in capacitor represents a binary bit '1', which is fully charged, or '0', which is discharged. The charge is stored and sensed by the transistor to write or read the memory capacitor cell, but the memory must be refreshed frequently to restore the charge to its intended value due to the discharge property of capacitor, hence the name dynamic memory. Because it has fewer components, DRAM requires a smaller area on a chip than does SRAM, and hence a DRAM chip can have a greater memory capacity, though its access time is slower than that of SRAM.

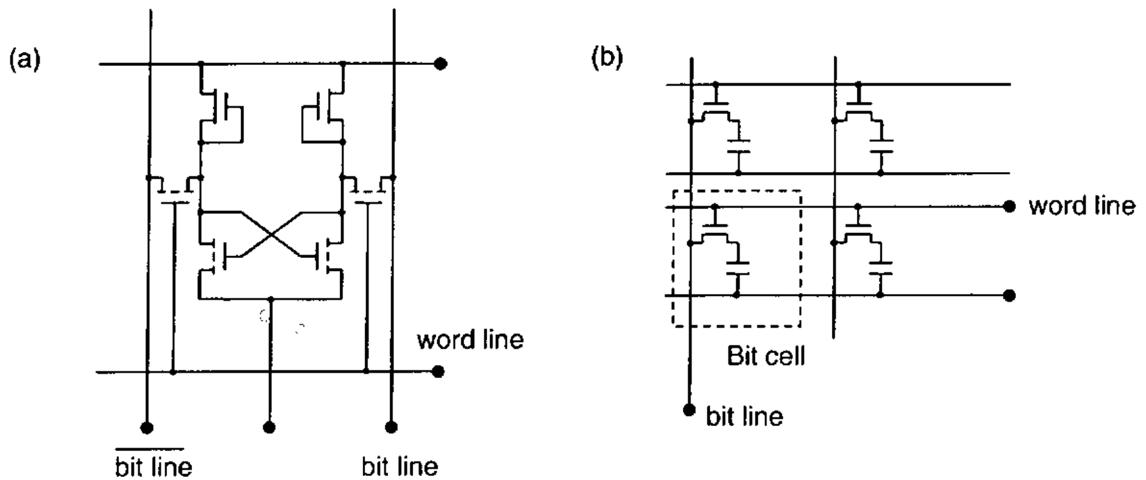

Figure 3.1 The circuits of (a) SRAM and (b) DRAM.

3.2.2 From conventional RAM to non-volatile ferroelectric RAM (FeRAM)

As mentioned before, MOS technology plays an important role in the fabrication of semiconductor memory. Field effect transistor (FET) in the MOS type, called MOSFET, is one of the useful semiconductor components like its bipola counterpart. It is a three-terminal device which terminals are named as 'source', 'drain' and 'gate'. The current flowing through source and drain is controlled by a voltage at the gate, and that current involves only majority carriers. Since the control voltage is applied across an insulator, the MOSFET is characterized as a high input impedance device. It is particularly suited for controlled switching between a conducting state and a nonconducting state so is useful in digital circuits. In fact, millions of MOSFETs are commonly used together in semiconductor memory devices.

Silicon dioxide (SiO_2) has been commonly used as the insulating oxide layer in MOSFET and its dielectric constant is around 7. With the scaling down technology

developing rapidly, the thickness of the oxide layer of MOSFET becomes thinner. Consequently there is a large leakage current out of the insulator. The charge-up process must be refreshed many times per second to sustain the memory states. Thus a high dielectric constant, high breakdown field and good resistance to charge injection material is needed.

However, the memory based on MOSFETs is still a volatile one and will lose the stored data once the electric field is removed. For non-volatility replacement of the conventional dielectric material by ferroelectric material is proposed. The ferroelectrics generally have high permittivity, which can be exploited to store information as charges. Ferroelectrics also exhibit polarization-voltage hysteresis and retain large remnant polarization even after the external electric field is being removed. Memory of this kind is called ferroelectric memory or ferroelectric RAM (FeRAM).

Ferroelectric memory has been studied for a long time after the initial proposals in 1957 [23-26], but an acceptable retention and read/write speed of such memories have not been demonstrated yet. Basically, it can be fabricated in the form of capacitor [27-48] in DRAM and ferroelectric field effect transistor (FeFET) [1, 2, 49-61]. They both possess nonvolatility, fast switching and radiation hardness. For ferroelectric capacitor, which consists of a ferroelectric layer with top and bottom electrodes, it simply utilises the hysteresis characteristics of ferroelectric material. The electric dipoles in the layer are aligned by an externally applied electric field and remain almost unchanged when

the field is withdrawn. The logic "0" and "1" can thus be stored in the capacitors as either a "+" or "-" polarization state of the ferroelectric layer. On the other hand, the remnant polarization of ferroelectric layer in the FeFET configuration will modulate the semiconducting channel. In fact, the FeFET can perform non-destructive readout and has a smaller footprint than ferroelectric capacitor with its access transistor, it is the preferred structure for use in memory cell.

3.3 Theory of ferroelectric memory

3.3.1 Basic operation of MOSFET

The schematic diagram of MOSFET is shown in figure 3.2 for the case of an enhanced n-type channel formed on a p-type Si substrate. The source and drain regions are heavily doped by diffusion of n-type material into the p-type substrate. There is no current flowing through from drain to source because of the oppositely directed p-n junctions in the drain-substrate-source series. Nevertheless, when a positive voltage is applied to the gate relative to the substrate, positive charges are deposited on the gate metal. In response, the same amount of negative charges is induced in the underlying Si forming a depletion region and a thin surface region of mobile electrons. These electrons form an n-type conducting channel between source and drain. The channel eventually eliminates the p-n junctions, and allows current to flow from drain to source. The effect of the gate voltage is to vary the conductance of the induced channel. In general, the positive gate voltage of an n-channel MOSFET must be larger than the

threshold voltage, which is the minimum gate voltage required to induced a conducting channel. Similarly, a p-channel MOSFET required a gate voltage more negative than some threshold value to induced the required positive charge (mobile holes) in the channel. There are exceptions to this general rule. For example, some n-channel MOSFETs have a conducting channel already in zero electric field, and a negative voltage at gate with respect to substrate is required to turn the device off. Such MOSFET is called a depletion-mode MOSFET. However, the MOSFET operating in the enhancement-mode is more common than operating in depletion-mode.

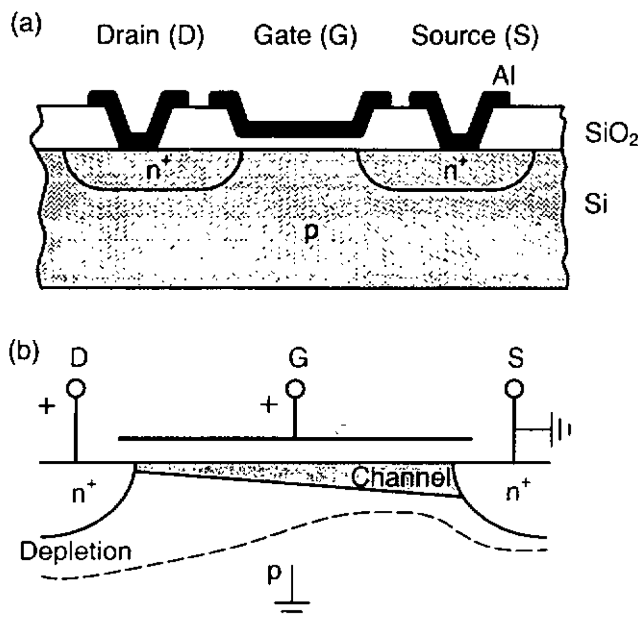

Figure 3.2 An enhancement-type n-channel MOS transistor (a) cross section of the device; (b) schematic diagram of the induced n-channel and the depletion region.

In fact, MOSFET is particularly useful in digital circuit, in which only logic states "on" and "off" are involved. The drain current is modulated by the gate voltage, and the gate terminal is in fact insulated from the source and drain by the oxide. Thus the d-c input impedance of a MOS circuit can be very large, usually in the order of 10^{11} ohms.

The n-channel MOSFET is generally preferred because the mobility of electron in n-channel is larger than the mobility of hole in p-channel.

3.3.2 Basic ferroelectric physics

Ferroelectricity, the property of ferroelectric, is named by analogy with ferromagnetism, which occurs in ferrous metals. Ferroelectric materials are a class of crystals, which has low symmetry along one or more crystal axes and has a spontaneous polarization. The polarization vectors of ferroelectric crystals can be oriented in two opposite directions by the application of an external electric field. As shown in figure 3.3, for example, lead zirconate titanate $Pb(Zr_xTi_{1-x})O_3$ (PZT), the positive and negative states in a ferroelectric crystal are due to displacements of positive metallic and negative oxygen ions in opposite directions. The symmetry of the crystal is distorted from a cubic structure to a tetragonal structure. Nevertheless, the ferroelectric behavior depends on temperature. This behavior will be lost in a given ferroelectric at above a characteristic temperature called Curie temperature.

The dipoles in ferroelectric can be lined up by an external electric field and their polarization can be retained even after removing the field. The orientation of one dipole will influence the surrounding dipoles to have an identical alignment. A ferroelectric hysteresis loop is shown in figure 3.4. When an electric field is applied across the ferroelectric, the dipoles begin to line up with the applied field. At a point of the maximum or saturation, all of the dipoles are lined up, polarization P_{sat} is obtained.

When the field is reduced back to zero, a remnant polarization P_R remains due to the coupling between the dipoles. In the same way, if an electric field is applied in the opposite direction, the dipoles are reversed. As the field continues to alternate, a hysteresis loop representing how the polarization of the ferroelectric varies with the field is obtained.

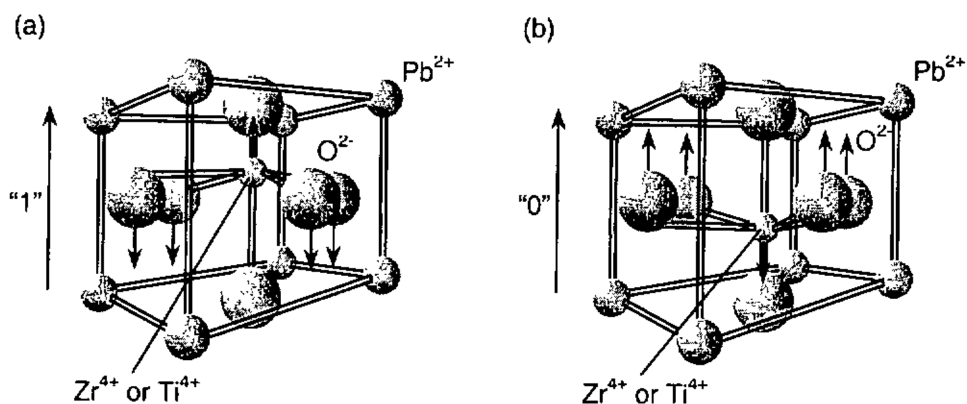

Figure 3.3 Unit cells of ferroelectric crystals of the cubic pervoskite $Pb(Zr_xTi_{1-x})O_3$ shows polarization up (a) or down (b) corresponding to logics "1" or "0".

Domains, being regions in the material in which all the dipoles are aligned, occur in as-grown ferroelectric crystal, and they have a mixture of random polarizations. The process of orienting all the domains in one direction is called poling. Thus, after the poling process, the ferroelectric can be switched from one stable state to another stable state that provides the basis for the binary code-based nonvolatile ferroelectric memory.

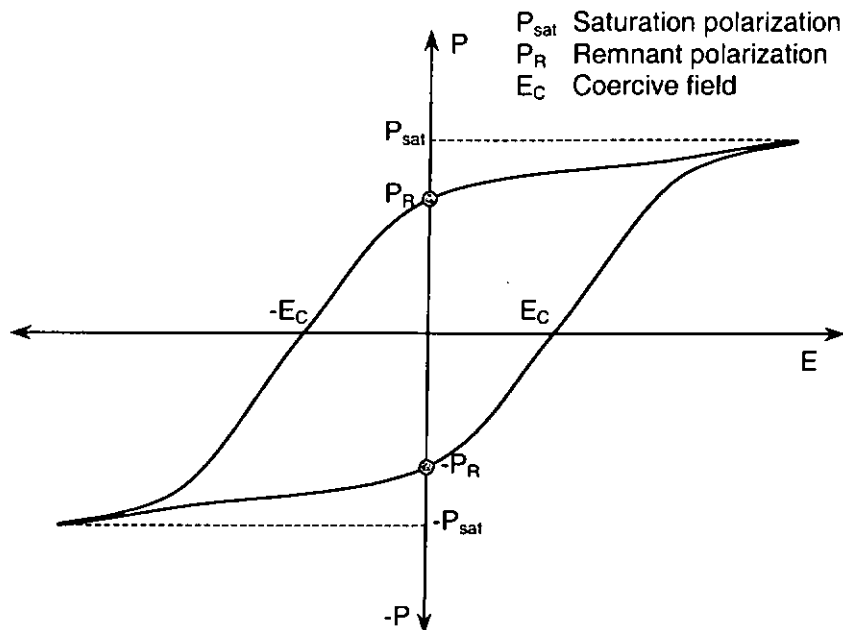

Figure 3.4 A typical ferroelectric hysteresis loop.

3.3.3 Physics of ferroelectric capacitor

Non-volatile ferroelectric capacitor utilises property of remnant polarization. As shown in figure 3.5, it composes of a ferroelectric layer sandwiched between a top and a bottom electrodes. When an external electric field is applied across the two electrodes, the ferroelectric layer is poled either positive or negative representing the binary logic "0" or "1".

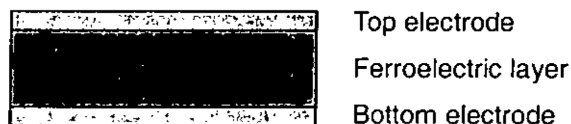

Figure 3.5 A typical ferroelectric capacitor

A typical ferroelectric layer material is PZT, which has a perovskite structure with lattice constant of about 4 Å. In some previous researches, platinum (Pt) was used as

electrode [29, 35, 36, 44]. Pt has high electrical conductivity. Highly oriented (111)Pt films can be grown on silicon (001). It has been widely used in semiconductor industry. Recently, the applications of conductive oxides like IrO_2, $SrRuO_3$, $LaSrCoO_3$, $LaCaMnO_3$ and $LaNiO_3$ [27-30, 40, 44-46, 48] as the electrodes have been reported. These oxides are also of perovskite structure. They can provide a better lattice matching and an enhanced chance for epitaxial growth of ferroelectric. An improved interface between the ferroelectric layer and electrodes can reduce the trapped charges that cause polarization switching fatigue. Fatigue-free operation of PZT up to 10^{12} switching cycles was achieved by using the conductive oxide electrode [28, 48]. On the other hand, the ferroelectric fatigue occurs at about 10^5 switching cycles when using Pt electrodes [35, 36]. In fact, the conductive oxide-based ferroelectric capacitors with excellent electrical cha acteristics have been fabricated. Integration of these capacitors on silicon has also shown good crystalline structure [48].

3.3.4 Physics of ferroelectric field effect transistor

More complicated than the ferroelectric capacitor, a ferroelectric field effect transistor (FeFET) involves field effect like the metal-oxide-silicon FET. The simplest structure of FeFET is based on metal-ferroelectric-silicon FET (MFSFET) [23, 60], However, the ferroelectric/Si interface is hard to control. For example, it is well known that PZT reacts easily with Si and the interdiffusion of Pb and Si at the PZT/Si interface occurs even at temperature as low as 500°C [61]. Therefore, in order to improve the interface, a very thin buffer layer such as SiO_2 [52, 54], $SrTaO_6$ [56] or even silicon

nitride [55] needs to be introduced in between the ferroelectric layer and silicon forming a metal-ferroelectric-insulator-semiconductor (MFIS) structure as shown in figure 3.6. The thin buffer layer can improve the interface and slow down the interdiffusion. Besides, it does not affect the induction of field effect in the semiconductor because it is sufficiently thin.

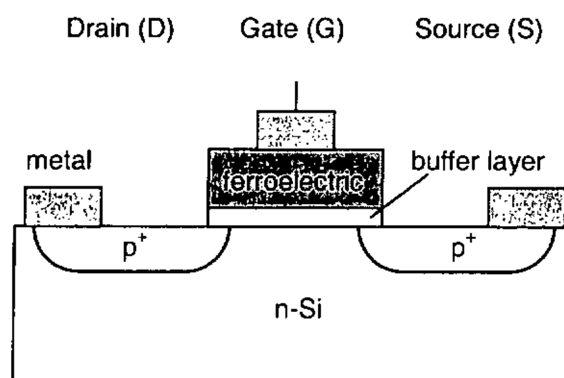

Figure 3.6 The structure of metal- ferroelectric-insulator-semiconductor (MFIS) FET.

There is another structure called metal-ferroelectric-metal-insulator-semiconductor (MFMIS) [37, 57], that is illustrated in figure 3.7. This type of FeFET, in fact, comprises a ferroelectric capacitor and a conventional MOSFET. The retained charges at the bottom electrode of the capacitor due to the remnant polarization of the ferroelectrics is coupled to the semiconductor and the conducting channel is then induced to allow the current flowing through from drain to source. The logic states can be represented by the conduction conditions in the channel.

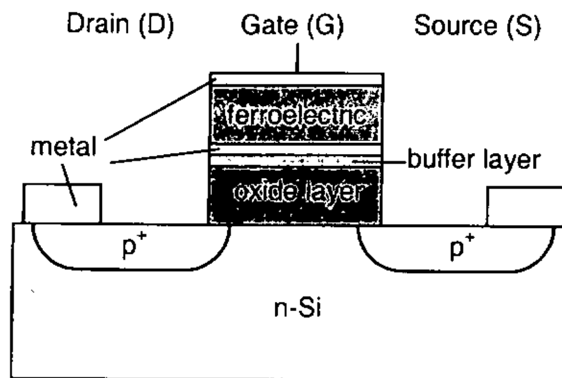

Figure 3.7 The structure of metal- ferroelectric-metal-insulator-semiconductor (MFMIS) FET.

Recently, a novel approach to FeFET was proposed [1, 2] to further improve the interface between the ferroelectrics and semiconductor. These FeFET heterostructures use, instead of Si, a semiconductor-like perovskite oxide such as such as $LaSrCuO_3$ (LSCO) or the doped rare-earth manganates (eg. $LaCaMnO_3$ (LCMO)) as the semiconductor layer. The carrier concentration of these oxides varies widely with both La:Sr or La:Ca and the oxygen content. In addition they have lattice constants which are closely matched with many ferroelectrics. A typical structural layout of these FeFET is shown in figure 3.8.

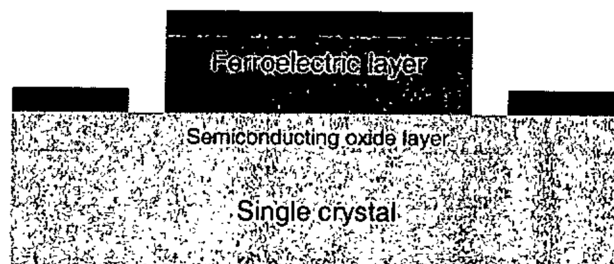

Figure 3.8 The structure of the FeFET by use of semiconducting oxide layer.

The operation of such novel FeFET is quite different from MFIS and MFMIS FETs. In such FeFET there is no pre-diffusion of other type semiconductor into the semiconductor. Instead, the remnant polarization modulates the region of semiconductor just below the ferroelectric. When a positive voltage is applied to the gate and p-type semiconducting layer, it polarizes the ferroelectrics. The electric dipole moments of the ferroelectric point downwards towards the semiconducting oxide (shown in figure 3.9). This action actually causes the buildup of a positive charge on the bottom side of the ferroelectric that will be compensated by the same amount of negative carriers in the channel, thereby reducing the channel of positive holes. The channel resistance therefore increases under positive poling. Similar argument is true for the negative poling and the channel resistance becomes smaller.

In this program, we attempted to fabricate such FeFET using $LaSrMnO_3$ (LSMO) as the semiconducting layer. LSMO has shown to have high thermal stability and can be fabricated at relatively low processing temperature.

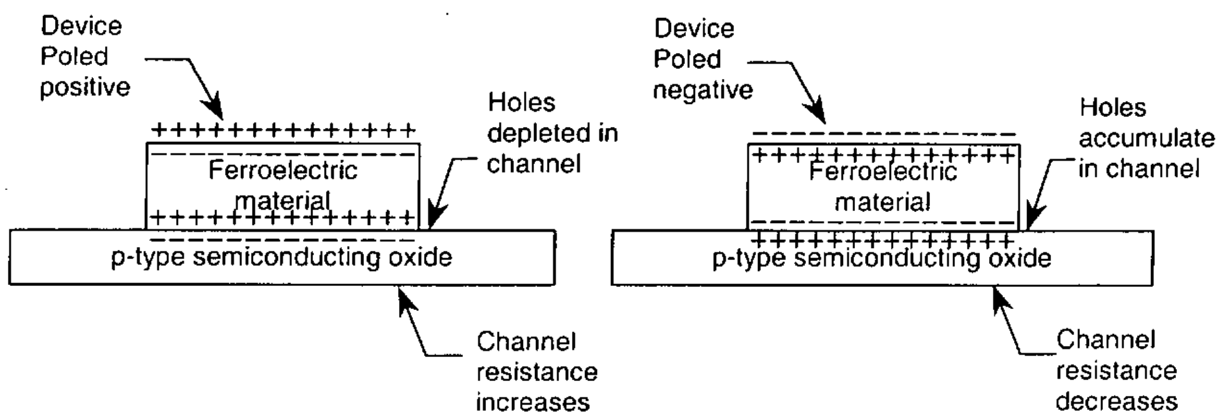

Figure 3.9 Schematic diagram of a simplified model of the field effect in p-type ferroelectric FET.

CHAPTER 4

EXPERIMENTS AND SET-UP

4.1 Pulsed Laser Deposition (PLD)

4.1.1 The experimental set-up of PLD

A Krypton Fluoride (KrF) excimer laser with a wavelength of 248 nm (Lambda Physik COMPex 205) was used for the fabrication of all samples. The excimer molecules are formed in a gaseous mixture of the component gasses of Kr, F_2, He and Ne. The total pressure in the laser chamber is 3400 mbar in which the partial pressure of Kr, F_2, He and Ne are130 mbar, 4 mbar, 56 bar and 3210 mbar respectively. The ionic and electronically excited species are created by the avalanche electric discharge excitation (~40 kV). The excited species react chemically to produce the excimer molecules, of which the ground state is repulsive and tends to dissociate rapidly. The maximum output of the laser is about 550 mJ per pulse for a pulse duration of 25 ns.

The laser beam was first reflected by a mirror and then focused by a convex lens through a fuse silica window on a rotating target, mounted inside a vacuum chamber. The laser intensity after passing through the window and lens was about 60% of the original laser output. The laser spot size on the target surface was estimated to be about 3 mm^2. The schematic diagram of the pulsed laser deposition system is shown in figure

4.1.

A mechanical rotary pump (ULVAC D-330K) and a cryro pump (CTI-CRYOGENICS CRYO-TORR 8) (not shown) were used to evacuate the vacuum chamber system. The chamber could be pumped down to a base pressure of 5×10^{-7} Torr. The attached baratron (MSK Type 122A) and ionization gauge (ULVAC type WIT) were used to detect the pressure of the chamber in a range of 10^{-3} – 10 Torr and 10^{-7} - 10^{-3} Torr, respectively.

All ablation targets were in the form of a circular disc of 1" diameter and 0.25" thick. They were strung onto the end of a rotating shaft, which was driven by a dc motor and could be slided in and out of the chamber for selection of an appropriate ablation target. The focused laser beam was directed on the circular surface of the target as shown in figure 4.1. In this way our PLD system allows us to in situ fabricate of multi-layers of different materials. The laser induced plasma plume from the target was aligned perpendicularly with the normal of the substrate. The target-substrate distance was kept about 45 mm during the deposition for different materials.

The heating filament was formed by a length of Kanthal wire (25% chromium, 5% aluminium, 3% cobalt and 67% iron) with 0.559 mm diameter and a resistance per unit length of 5.1 Ωm^{-1}. The wire was wound inside the substrate holder box. A K-type stainless steel shielded thermocouple was inserted right underneath where the substrate

was attached. A steady temperature control was provided by a PID controller (Shimaden SR-19) and power regulator (PAC25-0321). Good thermal contact between the substrate holder and the substrate itself was guaranteed by the adhesion of the quick drying silver paint (G3691). The temperature gradient between the thermocouple and the

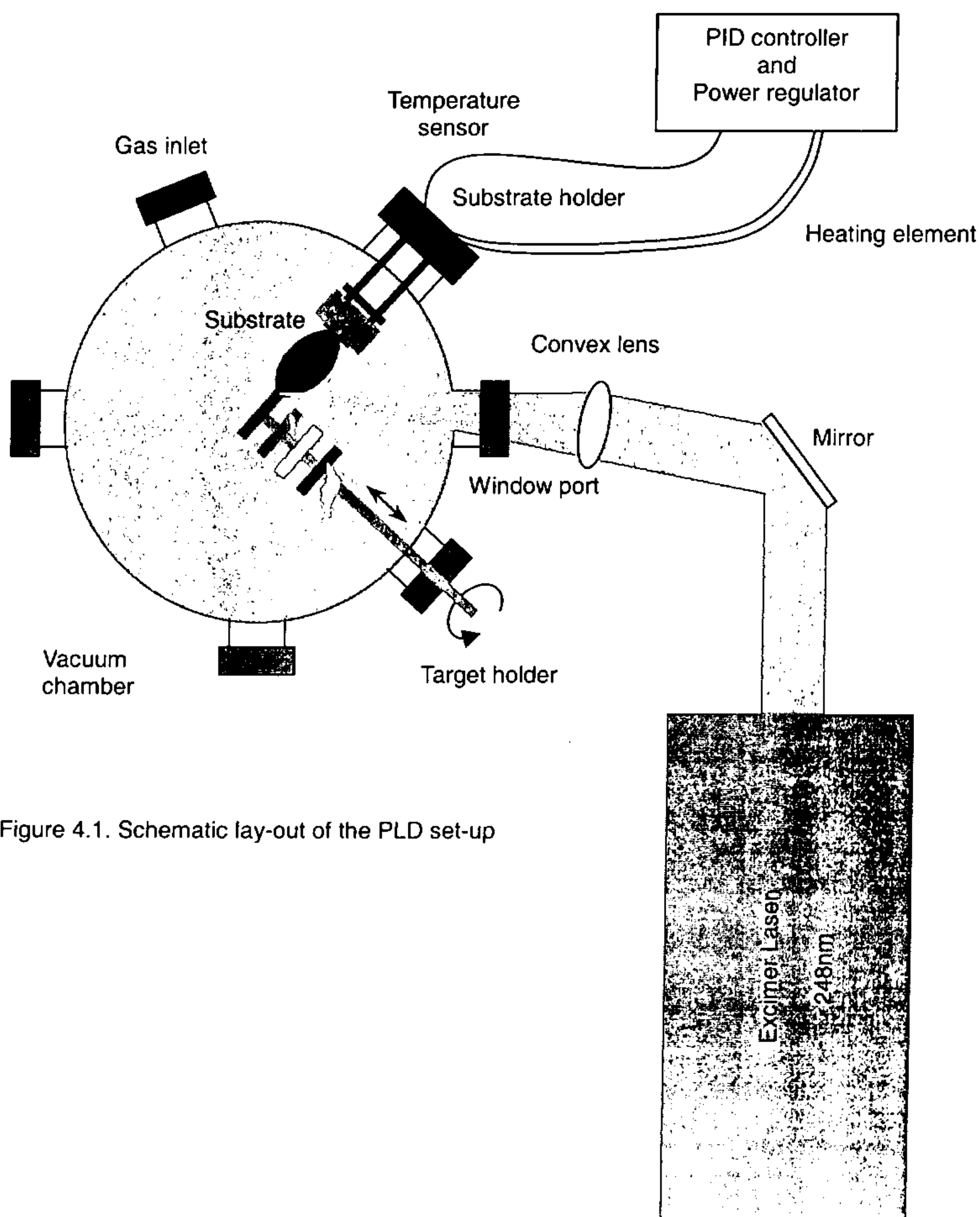

Figure 4.1. Schematic lay-out of the PLD set-up

heating sample was reduced. The actual temperature of the substrate was estimated to be 30°C lower than the measured temperature from the PID controller at an absolute temperature of 600°C. All quoted processing temperature in this report are the PLD controller shown temperature.

4.1.2 Procedure of fabricating thin films by PLD

In the present study, LSMO and PZT films were deposited using the PLD system just described. The KrF excimer laser running at the repetition rate of 10Hz was used throughout the film fabricating process. Films were grown on (001) LAO substrate under different deposition conditions. The laser beam was focused on the targets and the plasma plume was aligned with the centre of substrate holder. The laser fluences used were estimated to be 6 J/cm^2 and 4 J/cm^2 for LSMO and PZT targets, respectively. Before gluing onto the holder face plate, the substrates were cleaned ultrasonically and rinsed in deionized water for several times. For fabricating the PZT/LSMO structure, the substrate was pattern-masked before deposition. This masking process will be discussed in chapter 6. The thickness of the films under the said fluences was 20 – 80 nm for LSMO and 500 nm for PZT in the PZT/LSMO structure. For single layer characterization the LSMO film was, however, 200 nm thick. The substrate temperature for growing LSMO films varied from 450° to 700°C while that for PZT films was kept at 620°C. The ambient oxygen pressure during the LSMO films fabrication changed over a wide range from 0.1 to 200 mTorr for detail studies of electrical properties as a function of oxygen content of the films. After deposition of each LSMO film, the films

were annealed under the same deposition temperature for 1 to 60 minutes, releasing the stress in the grown film to improve the crystallinity. On the other hand, the oxygen pressure used in the PZT films fabrication was fixed at 200 mTorr. The PZT films were cooled down to room temperature under one atmosphere oxygen pressure without any post-annealing. The lead and the lead oxides in the films are volatile under such high temperature. Prolong heating may cause severe lost of Pb and is detrimental to the structural and electrical properties of the films. The grown films were characterized by the following discussed techniques and the electrical measurements were also carried out followed by coating of gold as electrodes.

4.2 Sample characterizations and measurements

4.2.1 Structural characterizations

4.2.1.1 X-ray diffractometry (XRD)

X-ray diffractometry (XRD) is a common non-destructive method for determining the information about crystal structure and atom location of various materials in bulk solids, powders or thin films. It was used to investigate the quality of our targets and epitaxial multi-layer thin films. The XRD system involved was a Philip X'pert system operating in four-circle mode. The CuK_{α} radiation with a wavelength λ of 1.54 Å, was used. The radiation from K_{β} line was filtered out by a Ni filter.

The X-ray radiation from the X-ray source interacts with the electronic dipoles

and is scattered in all directions. The radiation scattered from one atom interacts destructively with radiation from other atoms except in certain directions like figure 4.2. In these directions, the scattered radiation is reinforced rather than destroyed. From the diagram, the constructive interference happens when

$$AB + BC = n\lambda \text{, n=1,2,3,...}$$

and because AB = BC = d sinθ, it follows Bragg's Law

$$2d\sin\theta = n\lambda \text{, n=1,2,3,...}$$

where n is the order of the intensity maximum, λ is the X-ray wavelength, d is the interplanar spacing, and θ is the angle of incident of X-ray beam.

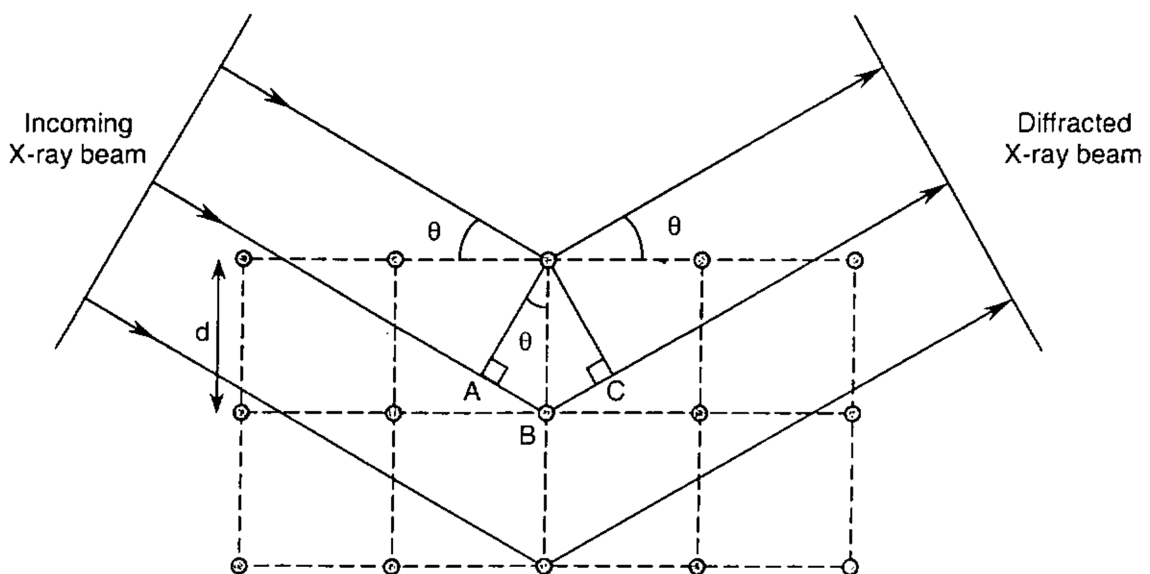

Figure 4.2 Bragg diffraction of X-rays from successive planes of atoms. Constructive interference occurs for ABC equal to an integral number of wavelengths.

The interplanar spacing for a simple cubic structure can be determined by the following equation

$$d = \frac{a}{\sqrt{h^2 + k^2 + l^2}},$$

where a is the lattice constant of the crystal structure and h, k and l are the reciprocal lattice indices for a, b, c axis respectively.

The experimental geometry of X-ray diffractometer (XRD) is illustrated in figure 4.3. It shows the X-ray source, different kinds of slits, monochromator and detector. Also, there are four rotating axes of θ (ω), 2θ, χ and ϕ for different scan modes. We will use the θ-2θ, ω and ϕ scans to confirm the epitaxy of our thin films.

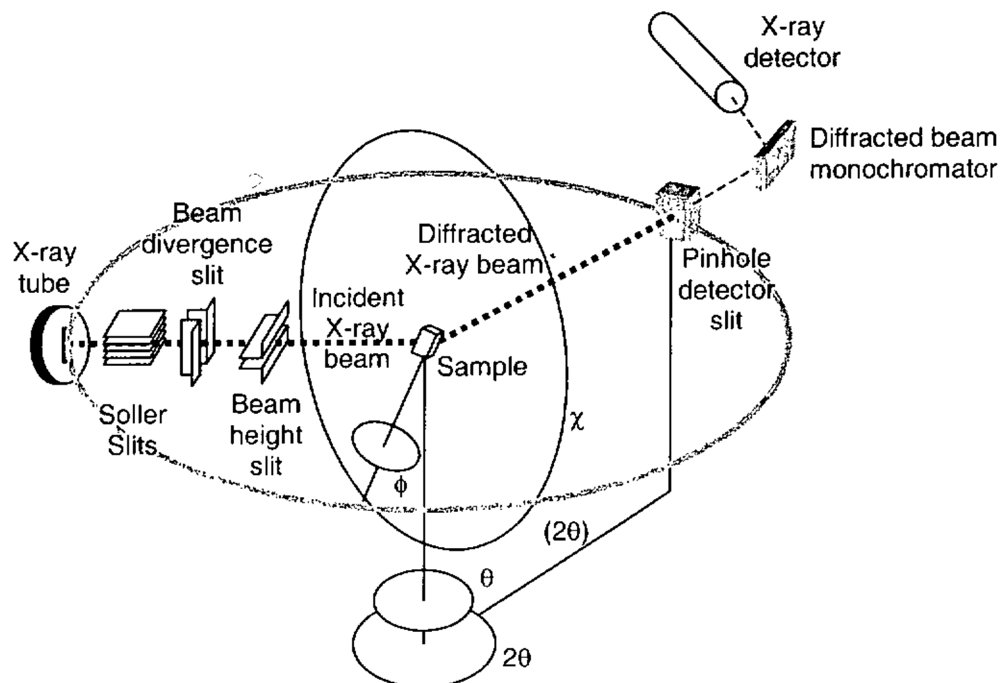

Figure 4.3 Experimental geometry, showing four primary axes of goniometer, X-ray tube, detector and slits

In the θ-2θ scan, the X-ray source is fixed at a position. While the sample rotates a certain angle with respect to the X-ray beam axis, the detector rotates twice of that angle as shown in figure 4.4. It allows the detector to follow the reflected ray and to receive the strongest signals from the zeroth order diffraction. The constructive diffraction lines reflect the crystal structure of the materials under investigation. With appropriate calculation information like the crystalline phases and orientations can be determined.

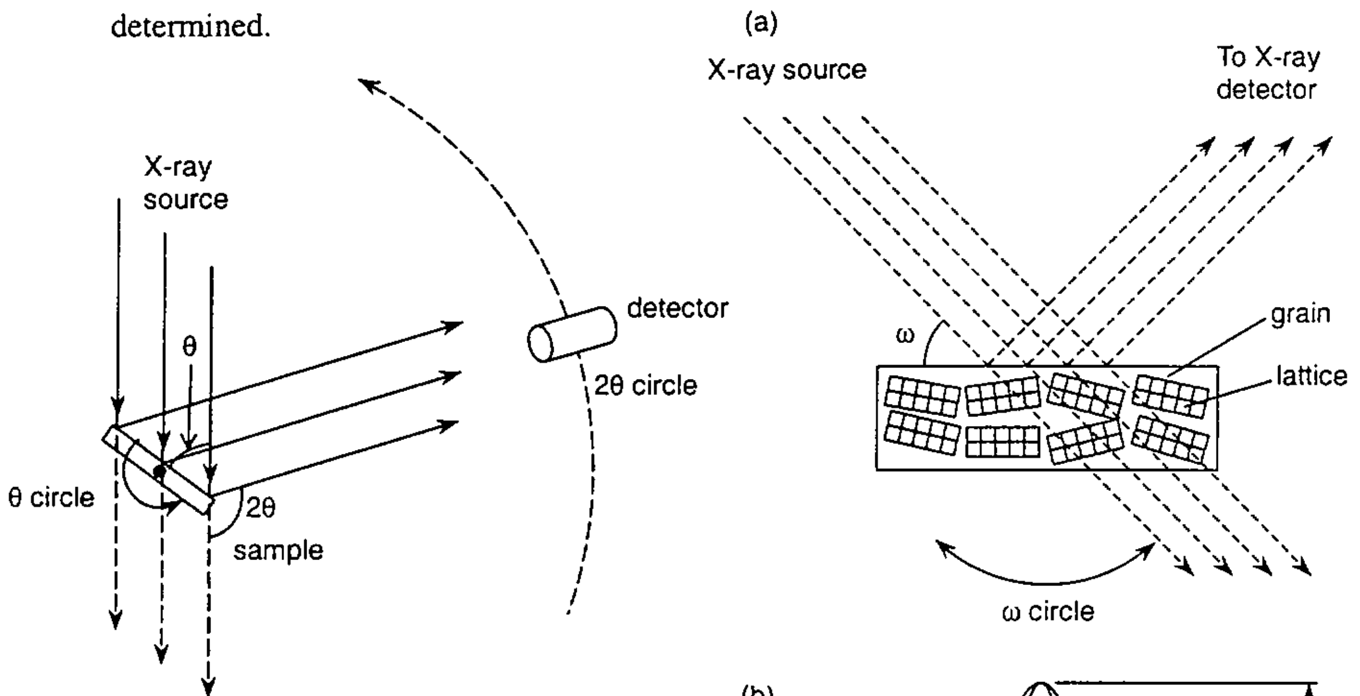

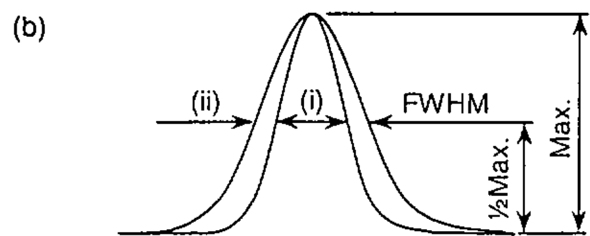

Figure 4.4 The schematic diagram of θ-2θ scan, it shows the moving angle of detector is twice of that of the sample.

Figure 4.5 (a) The FWHM of ω scan reflects the alignment of different polycrystalline at a particular orientation. (b) The FWHM of broad and narrow rocking curves.

The θ-2θ scan, however, yields only the information on the out-of-plane crystalline orientations of the film but cannot give quantitative measurements of the orientations, i.e. the degree of alignment of the crystal grains with each other in the films. ω scan, on the other hand, supplies us with this information. Grains with different orientations in a thin film examined by ω scan mode are shown in figure 4.5a. The X-ray source and detector are fixed at certain θ angle for a particular orientation crystal plane reflection the sample is rocked along the ω axis. The constructive diffraction occurs only when a grain is aligned at the angle according to Bragg's Law. Therefore, a broad profile will be obtained if the grains are not well aligned in the same direction. Conversely, a very narrow profile will be observed if the grains are perfectly aligned. Often the ω scan profile is referred as rocking curve. The full width at half maximum (FWHM) of the rocking curve is used as a parameter to determine the quality of the film orientation, which is shown in figure 4.5b. The narrow profile (i) smaller FWHM means a better film quality in orientation. The broad profile (ii) suggests a bad film quality. For the FWHM of the rocking curve is less than or around 1°, the film can be considered as highly oriented. The FWHM of ω scan of single crystal like LAO or silicon is about 0.2° by our XRD characterization.

In order to confirm the epitaxy of the films, we need yet another scanning technique called ϕ scan. For a simple cubic structure as shown in figure 4.6, the X-ray source and the detector are fixed at an angle for, say, the (001) plane. Tilting the χ axis to an angle of 45° (not shown), the ϕ axis is then rotated from 0° to 360°. Within the

360°, there are four diffraction lines at 90° apart corresponding to (011), (101), $(01\bar{1})$ and $(10\bar{1})$ planes reflection. It thus reflects geometrical four-fold symmetry of the cubic structure. Other structures like tetragonal, it also shows the four-fold symmetry characteristic, but the tilting angle of the χ axis is different and depends on the arc-tangent of the ratio of the out-of-plane lattice constant, c and the in-plane lattice constant, a. For a more complex structural system such as hexagonal, in which a six-fold symmetry is observed, it needs to calculate the tilting angle of χ before carrying out the ϕ scan. In our studies, however, the LSMO and PZT are both perovskites with pseudo-cubic structures. We can simply regard this structure as simple cubic in performing the ϕ scan operation.

The interface of the substrate and the epitaxial thin film is shown in figure 4.7. By fixing the angle of the X-ray source and the detector to the diffraction angle of (011) plane, for example, for both substrate and film. If the two plots of ϕ scan show four-fold symmetry and the diffraction lines of corresponding planes are at the same angle. The film is said to be cube-on-cube epitaxially grown on the substrate. In our case higher order (022) planes were used due their stronger signal and higher resolution.

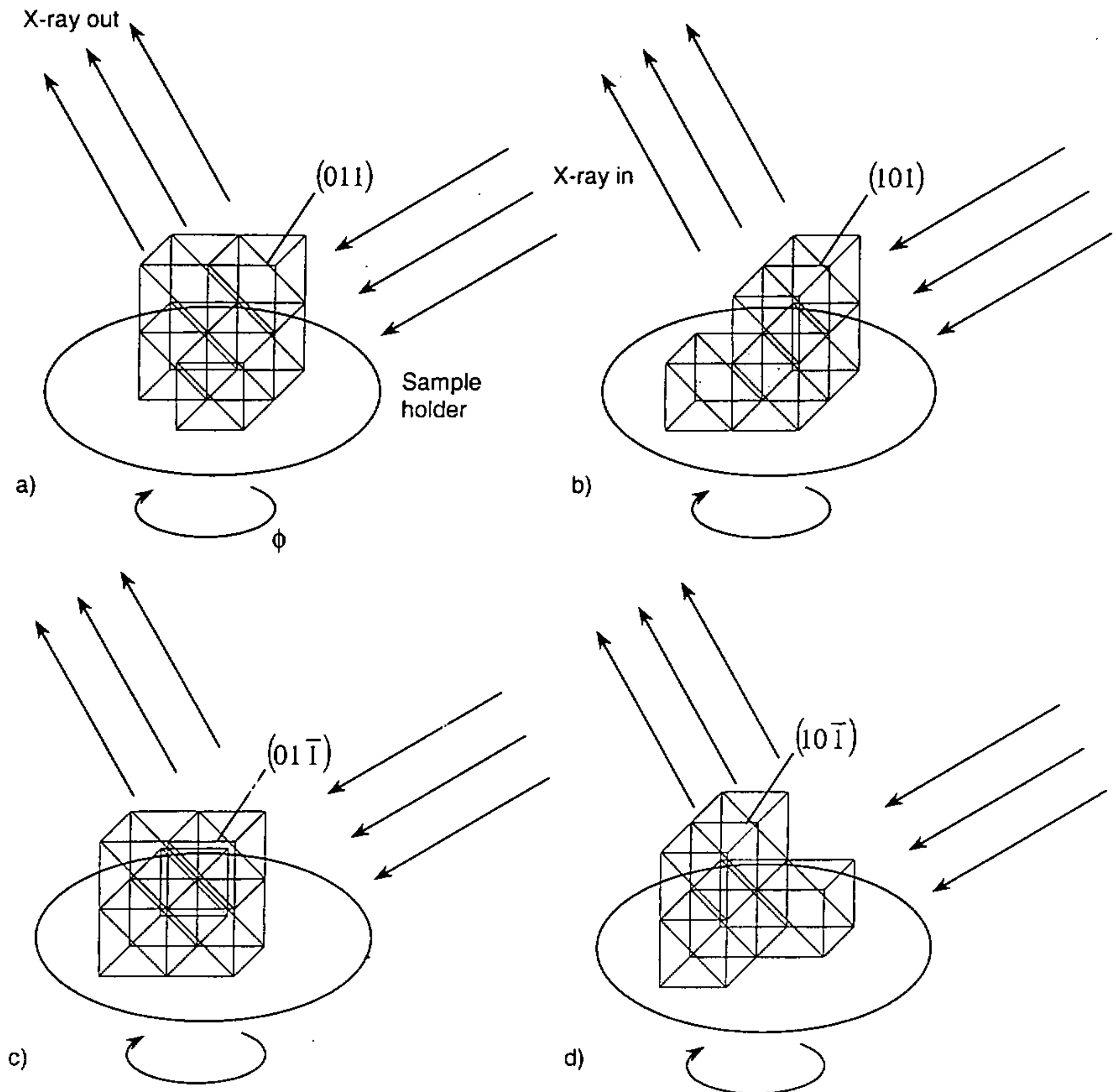

Figure 4.6 The illustrations of ϕ scan for the ϕ angles of 0°, 90°, 180° and 270° show the planes of (011), (101), $(01\bar{1})$ and $(10\bar{1})$ (not show the tilting angle χ).

In conclusion, the above three scanning techniques can provide detail structural characterization of the grown film and verification of cube-on-cube epitaxy.

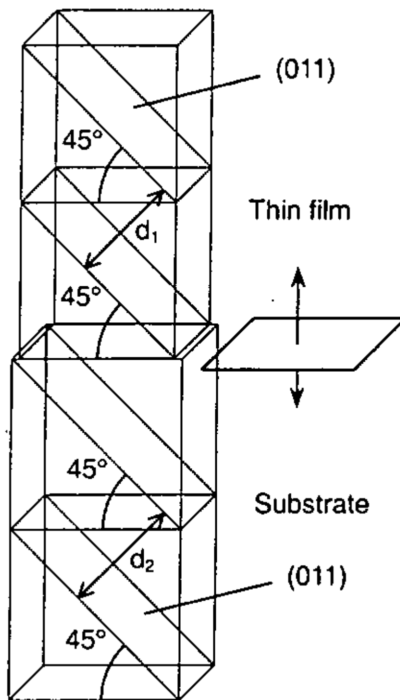

Figure 4.7 Cube-on-cube epitaxial thin film. d_1 and d_2 are the interplanar spacing between the two (011) planes of the film and substrate, respectively.

4.2.1.2 Scanning electron microscope (SEM)

Apart from the X-ray differentometry characterization of crystal structure, the surface morphology of thin films was investigated by scanning electron microscopy. The model of scanning electron microscope (SEM) used in our thin film characterization is a Leica stereoscan 440. Its principle maximum amplification is 300,000. The grains in the size of 20-30 nm can just be resolved under this amplification.

The idea of electron microscopy is that in using energetic electron beam, which have a shorter wavelength λ (about 0.1 nm), instead of the light photons ($\lambda \approx$ 400-700 nm) in optical microscope, better resolution images are obtained. In SEM, the detector collects the electrons that are knocked out of the specimen atoms by the electron beam. The signal from detector is then amplified by circuitry and synchronised with the scan

generator to produce the image. The schematic diagram of SEM is shown in the following figure. Electrons are generated from the cathode, a heated sharply pointed rod of lanthanum hexaboride. After leaving the cathode and shield, they are accelerated towards the anode. If the stabilization of the high voltage is adequate, electrons pass through the central aperture at a constant energy. The intensity and angular aperture of the beam are controlled by the condenser lens system between the gun and specimen. The beam after being minimized is deflected to scan over the region to be investigated in a raster pattern of lines by the magnetic field of the scanning deflection coil. The deflected beam is finally focused on the specimen by the objective lens through the correction elements of astigmatism, stigmator.

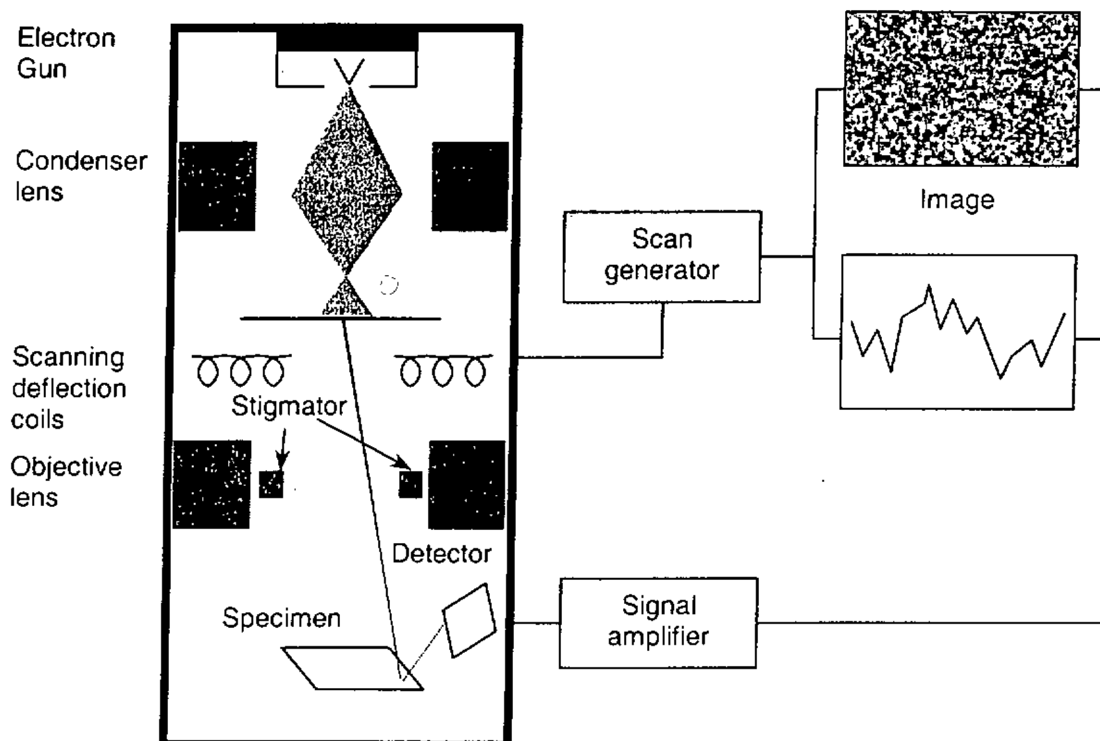

Figure 4.8 The simplified schematic diagram of scanning electron microscope.

The electrons that escape from the specimen basically are divided into backscattered electrons and secondary electrons. They are classified according to their energy. The energy for backscattered electrons is more than 50 eV while for secondary electrons is less than 50 eV. The backscattered electrons are generated by the elastic collision of the incident electron beam and the nucleus of the specimen. In the collision the direction of the beam electron is changed but the energy exchange is very small and less than 1 eV. On the contrary, the secondary electrons come from the inelastic collision of electron. The interaction in this inelastic collision results in the transfer of a few electron volts of energy to the conduction band electrons. Because of a large difference between escape depth of them, for backscattered electron the escape depth is sub-micron while for secondary electron it is in the order of 10 nanometres, they are collected and reconstructed as image with high topographic contrast. For smooth specimen surfaces shown in figure 4.9, they have the escape zones for both electrons uniformly deep in the specimen, resulting in minimal escape of electrons from the specimen per unit area. Rough surfaces have escape zone of both electrons thrown off the horizontal, producing more volume of escape zone per unit area and resulting in the escape of more electrons during bombardment by the electron beam. Besides, the number backscattered electrons is strongly depended on atomic number. The higher the atomic number the emitted backscattered electron increases more. It is so-called atomic number contrast of scanning electron microscope. Also the quality of reconstructed image can be improve by the noise reduction process, in which the scanning rate is slow and the number of raster line is increased. For non-conductive sample like our PZT

films, a sharper image can be obtained by a thin gold-coating surface (generally 10 – 20 nm thick). This is due to the increase emission of secondary and backscattered electron, reduction of thermal damages as well as the elimination of specimen charging. Thus details of surface morphology of the deposited thin films can be obtained by investigating the high resolution and high contrast SEM images.

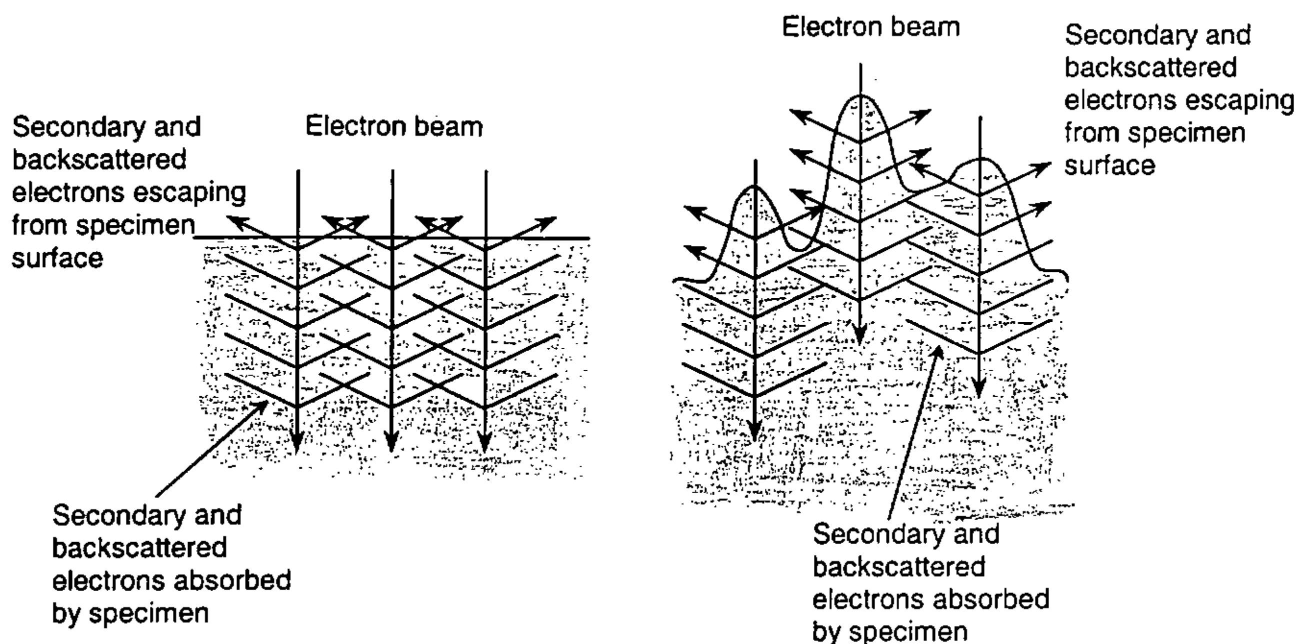

Figure 4.9 Topographic contrast. More backscattered and secondary electrons escape from a rough surface than from a smooth.

4.2.1.2 Thickness measurement

The thickness of the thin films can be determined by examining the SEM image of cross-section of the film. Film thickness measurement can be obtained by using Alpha-step profiler (Tencor Instrument, model P-7). A sharp edge is needed to carry out this measurement. For this reason, a mask should be placed to produce an edge during the

deposition. The idea of Alpha-step is to move a very fine needle across the step, detecting the thickness profile of the film like the following figure. The highest resolution of this instrument is less than 1 nm.

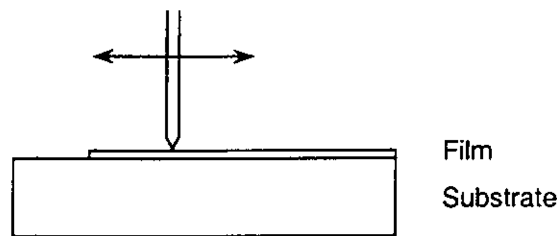

Figure 4.10 Film thickness measurement by Alpha-step.

4.2.2 Electrical properties analysis

4.2.2.1 Resistivity-Temperature measurement

The electrical conductive properties of materials can be revealed by the resistivity-temperature (R-T) measurement. The R-T profile does not only show the transition temperature of materials, but some other electrical transport properties are also displayed. We used this measurement to characterize our LSMO films fabricating under different deposition conditions. The following figure is a schematic diagram of our R-T measurement set-up. Four-point probe technique is used as a part of the resistance measurement. A platinum wire, in which the potential difference between the wire terminals at constant current is linearly proportional to the temperature, is used as the temperature sensor. The four-point probe signal of the sample and the platinum wire

signal are collected by a commercial interface card of national instrument (NI) and are processed by a programme written in a graphical programme language, Labview. A temperature control from room temperature to the liquid nitrogen temperature is achieved by a cryostat. The R-T profiles are displayed in the monitor screen during the measurement and the output to plotter using other software like origin or excel.

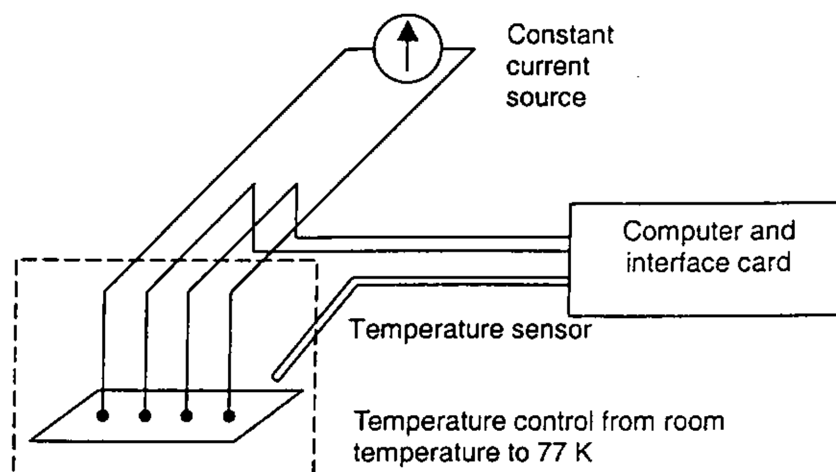

Figure 4.11 The schematic diagram of resistivity-temperature measurement, including the four-point probe, temperature sensor, temperature control system and computer with data acquisition card.

Four-point probe is a precise electrical measurement of the materials because it eliminates the contact resistance between the sample and the probes by the clever arrangement of the probes as illustrated in figure 4.12.

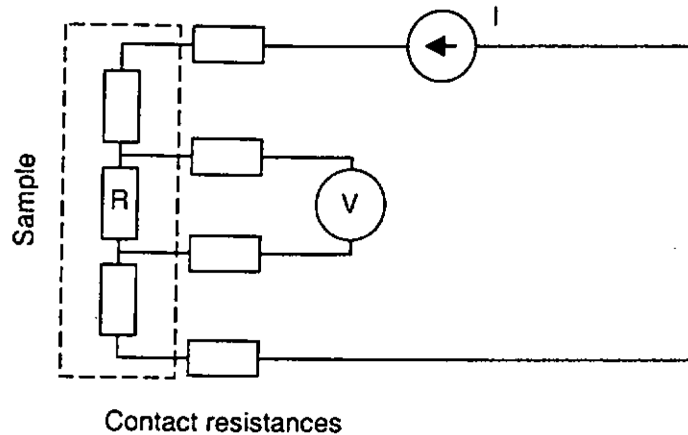

Figure 4.12 An equivalent circuit diagram of the resistance measurement using the four-point probe technique.

A constant current, I, passing through the outer two probes flows through the resistance R, of the sample resulting in a voltage drop V between the inner two probes. This potential difference is measured by a high input impedance voltmeter, in which there is no current flowing through the two inner probes for an ideal case. Therefore the resistance R is obtained simply by applying the Ohm's law, $V \times I$. Besides, the use of four-point measurement is more convenient to convert the resistance into resistivity by a simple calculation as follows.

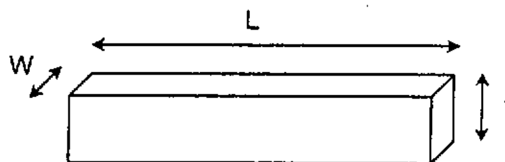

Figure 4.13

The resistance of the above rectangular block, R is proportional to the resistivity of the material, ρ, and the length, L, and inversely proportional to the cross-sectional area, A, which is the width W, multiplying the thickness t.

$$R = \rho \frac{L}{A} = \rho \frac{L}{W \cdot t},$$

However the sheet resistance (sometimes called the sheet resistivity), R_S is defined by the resistance of the block, if the length L, is equal to its width w.

$$\because L = w$$
$$\therefore R_S = \frac{\rho}{t},$$

where R_S is in the unit of ohm per unit area (Ω/□).

On the other hand, the sheet resistance of thin film, R_S is given by

$$R_S = \frac{V}{I} C.F.,$$

where V is the dc voltage across the inner probes (voltage probes); I is the constant dc current passing through the outer probes (current probes) and C.F. is the correction factor.

The correction factors for different geometry can have a change of factor of 2 or 3.

It depends on the ratio of the width of the sample and the spacing between two neighbouring probes, and also the ratio of the width and length of the sample. The correction factors of circular and rectangular samples are shown in Table 4.1.

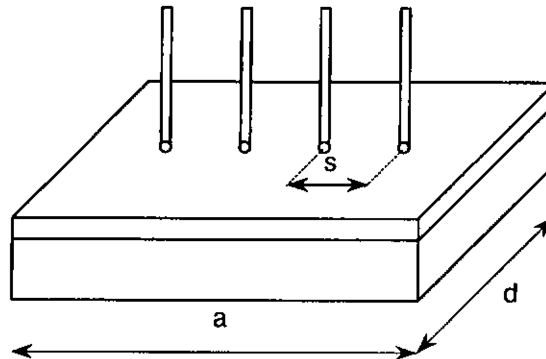

Figure 4.14 The four probes on the sample, a, d and s are the length, width and the distance between two nearest probes, respectively.

Table 4.1 Correction factor C.F. for the measurement of sheet resistances with the four-point probe (abstract from VLSI Technology, S.M. Sze)

		Square	Rectangle		
d/s	Circle	a/d = 1	a/d = 2	a/d = 3	a/d ≥ 4
1.0				0.9988	0.9994
1.25				1.2467	1.2248
1.5			1.4788	1.4893	1.4893
1.75			1.7196	1.7238	1.7238
2.0			1.9475	1.9475	1.9475
2.5			2.3532	2.3541	2.3541
3.0	2.2662	2.4575	2.7000	2.7005	2.7005
4.0	2.9289	3.1127	3.2246	3.2248	3.2248
5.0	3.3625	3.5098	3.5749	3.5750	3.5750
7.5	3.9273	4.0095	4.0361	4.0362	4.0362
10.0	4.1716	4.2209	4.2357	4.2357	4.2357
15.0	4.3646	4.3882	4.3947	4.3947	4.3947
20.0	4.4364	4.4516	4.4553	4.4553	4.4553
40.0	4.5076	4.5120	4.5129	4.5129	4.5129

The d/s and a/d ratios of our LSMO films are about 2.5 and 2 so the correction factor of 2.3532 was chosen. The resistivity become

$$\rho = R_S \times t = \frac{V}{I} C.F \times t = 2.3532 \frac{Vt}{I}.$$

The constant current is achieved by an inverting amplifier, which is constructed by operational amplifier LM 324 with a couple of resistors shown in figure 4.15, and the constant current is given by

$$I = \frac{V_i}{R} = -\frac{V_O}{R_S}.$$

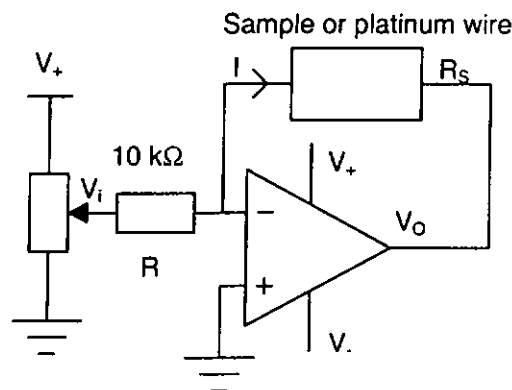

Figure 4.15 A simplified circuit diagram of the inverting amplifier

Due to the fix value of the ratio of V_i and R, the circuit can act as a constant current source to supply the current I through the sample or temperature sensor R_S. In our case, a resistor of 10 kΩ is selected as R while the input voltage V_i is 10 V. Thus a constant current of 1 mA can be obtained.

By this automation system of the R-T measurement, the R-T profile of the thin film can be obtained easily.

4.2.2.2 Hall effect measurement

Other electrical transport properties of LSMO films are obtained by Hall effect measurement, from which the sheet resistivity, carrier concentrations and mobilities can be assessed. Our LSMO films were measured by the Bio-Rad Microscience HL5500 Hall system at room temperature. The films were patterned as square shape. The four terminals were then probed on the corners of the film, two for giving a current while others applying the Hall voltage across the film. The illustration of Hall effect is shown in figure 4.16. A rectangular sample is placed in a magnetic field B_z. An electric field Ex applied across the end electrodes causes an electric current density j_x to flow down the rod. The drift velocity of the electrodes immediately after the electric field is applied. The deflection in the y direction is caused by the magnetic field. Electrons accumulate on one face of the rod and a positi 'e ion excess is established on the opposite face until the transverse electric field E_y just cancels the force due to the magnetic field.

A quantity called the Hall coefficient R_H can be deduced as

$$R_H = \frac{E_y}{j_x B},$$

also Hall coefficient is also written as

$$R_H = -\frac{1}{ne},$$

where n is carrier concentration and e is charge of electron. Besides, the mobility μ for hole is

$$\mu = \frac{R_H}{\rho},$$

ρ is resistivity of the sample. Therefore, carrier concentrations and mobilities of the samples can be easily obtained.

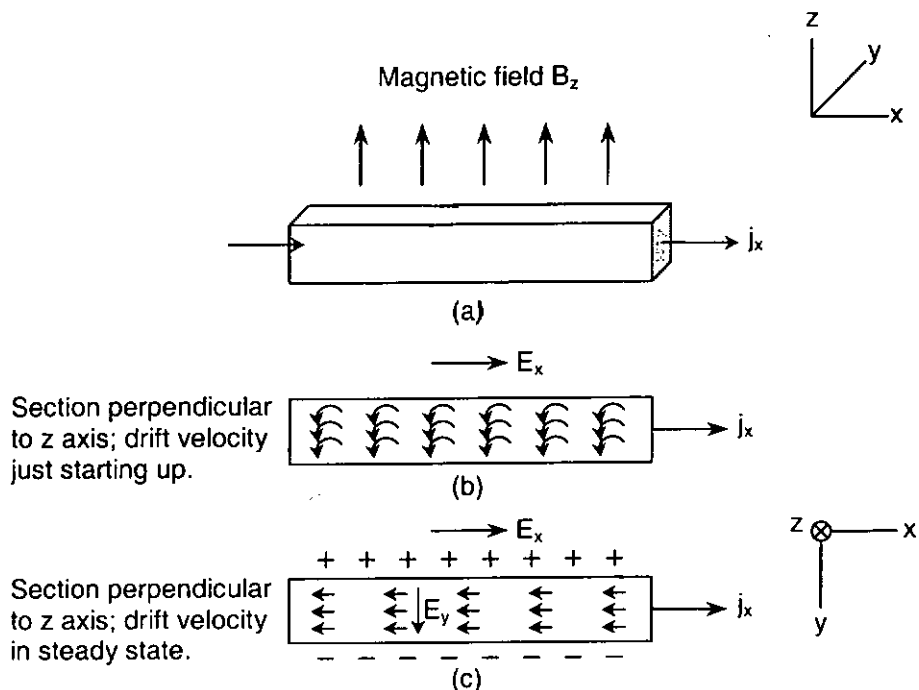

Figure 4.16 Schematic diagram to illustrate the Hall effect. (a) A external magnetic field B_z is applied to the sample. (b) The deflection of the drift current is caused by the magnetic field. (c) Transverse electric field E_y is applied to counteract the deflection.

4.2.2.3 Leakage current measurement

Other than the electrical measurement of the oxide films, the leakage current across the ferroelectric layer needs to be measured also. The leakage determines the polarization retention in the ferroelectric films. The leakage current for the ferroelectric films, say PZT film with the thickness of 500 nm, is in the order of 10^{-10} A under the driving voltage of 1 V. Most ammeters are not suitable for current lower than microampere. A digital electrometer, Advantest TR8652, is used in our studies to measure such small current. This is a 4-1/2 digit electrometer which employs a DC amplifier with an input impedance of 10^{13} Ω and the maximum resolution for current measurement is 10 fA.

By putting the two terminals of the meter across the top and bottom electrodes of the ferroelectric layer and setting the driving voltage, the leakage current can be measured. To increase the driving voltage gradually, the V-I characteristic of the ferroelectric layer can be obtained.

4.2.2.3 Polarization-Voltage measurement, fatigue and retention test

Polarization-voltage (P-V) or polarization-electric field (P-E) loop measurement is a mean to determine the electrical properties of ferroelectrics. In this measurement, we used a commercial test kit, a Radiant technologies RT66A standardized ferroelectric test system under virtual ground mode, to carry out P-V or P-E measurement. The drive and return terminals are connected to the top and bottom electrodes, respectively. While the

kit drives the ferroelectric material with a triangular voltage profile, it measures the polarization of the ferroelectric material simultaneously. After one cycle of the driving voltage, a hysteresis loop of P-V or P-E is shown, from which the saturation and remnant polarizations for both positive and negative poling as well as the coercive voltage or electric field can be determined.

Polarization switching fatigue is a prime concern for ferroelectrics like PZT. Other than that, we performed another test by RT66A that was the fatigue test. The fatigue test is to gauge the endurance of the ferroelectric materials against switching fatigue after many poling cycles. The ferroelectric material is poled continuously by a series of positive and negative pulses. Remnant polarization is measured just after the poling. Generally for a ferroelectric films with epitaxial oxide electrodes, fa igue-free operation up to 10^{11} cycles is possible. In our studies the multi-function RT66A was used in such tests for our PZT films.

The retention is another important parameter in ferroelectric material. This refers to the time duration for the ferroelectric material to retain the remnant polarization. The retention is strongly dependent on the quality of the ferroelectric material and the leakage current. It can be determined by the continuous measurement of the polarization after the ferroelectric material being poled.

4.2.2.5 Modulation

Modulation is a crucial factor that determines the performance of the FET. In an ideal FET it is better for the channel resistance to be short-circuited at a low state while open-circuited for a high state. However, such device is impossible to fabricate in practice. Instead, device with a high enough modulation depth is preferred. A typical circuit for measuring the FET modulation is illustrated in figure 4.17. The circuit consists of a bipolar voltage pulse source, a dc power source and an ammeter. The modulated current is measured after either positive or negative poling. In order to eliminate the erroneous signal due to leakage current through the ferroelectric layer, the pulse source is disconnected from the sample during the resistance measurement.

The modulation in FeFET is given by $\frac{R_{max} - R_{min}}{R_{min}} \times 100\%$.

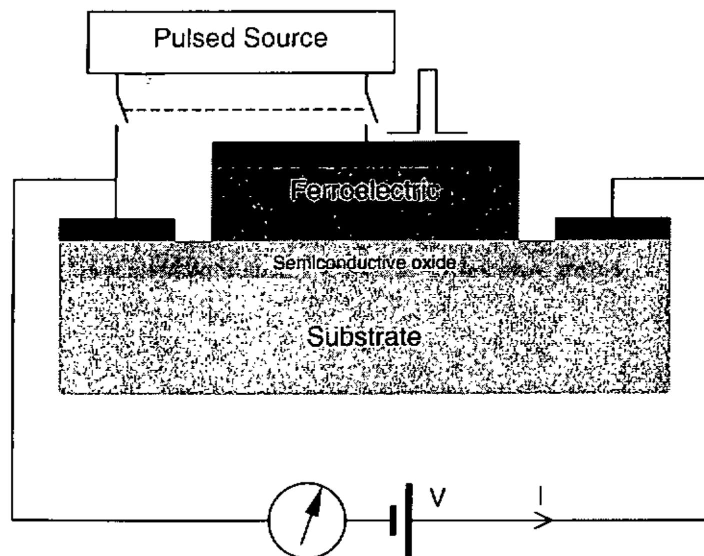

Figure 4.17 Electrical circuit arrangement for FeFET modulation measurements.

CHAPTER 5

FABRICATION AND STRUCTURAL CHARACTERIZATION OF LSMO/LAO AND PZT/LSMO/LAO HETEROSTRUCTURES

The aim of the present study is to fabricate an epitaxial PZT/LSMO heterostructures for potential use in ferroelectric field effect transistor. As the film's quality is primarily governed by their structural properties, epitaxial crystalline films are therefore needed in high performance device. The structural characterization of the thin films is of fundamental importance. In this chapter, we will present the results of LSMO and PZT/LSMO thin films structural characterization by XRD and SEM. As both the PZT and LSMO ablation targets are made by ourselves, we begin, however, with the description of target fabrication and characterization.

5.1 Target fabrication and characterization

Both PZT and LSMO targets were fabricated by the standard solid state reaction method. The PZT and LSMO target composition were examined by energy-dispersive X-ray spectrometer (EDX) and were determined to be $PbZr_{0.52}Ti_{0.48}O_3$ and $La_{0.7}Sr_{0.3}MnO_3$, respectively. The crystalline structure of the PZT and LSMO targets was then characterized by XRD. The XRD diffraction lines of the targets are defined and shown in figure 5.1.

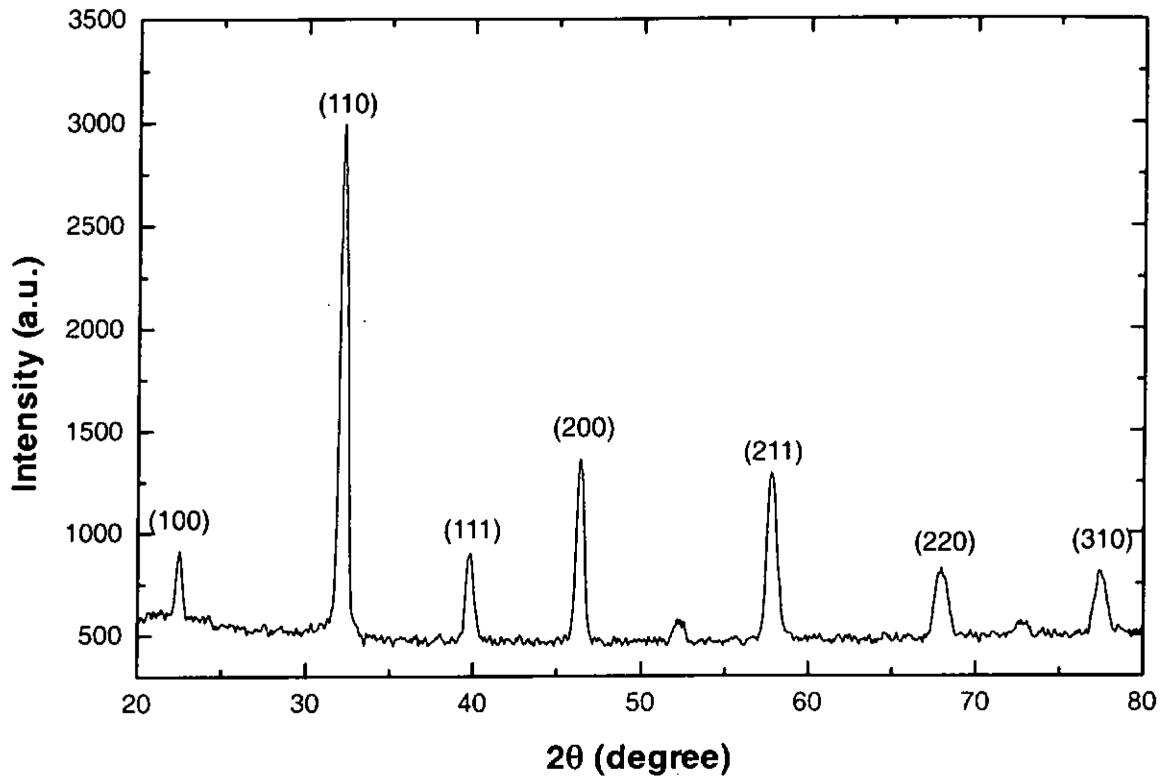

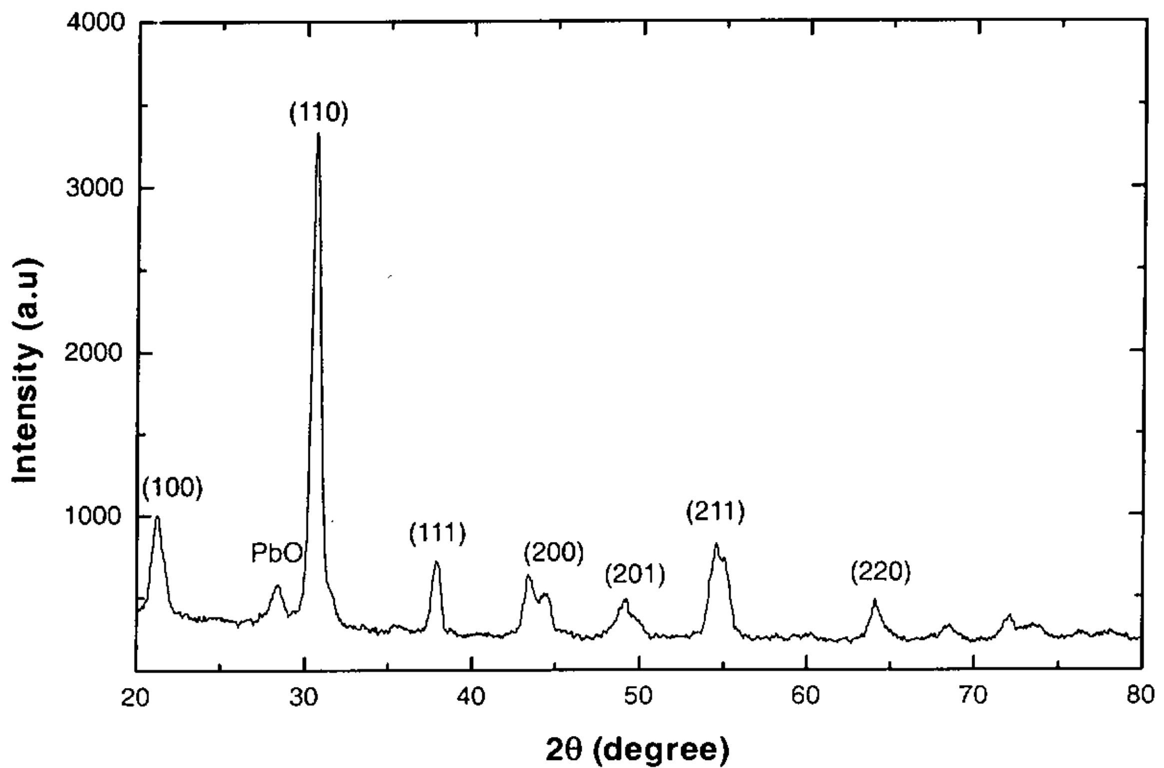

Figure 5.1 The XRD patterns of the LSMO and PZT perovskite oxide target.

5.2 Structural analysis of $La_{0.7}Sr_{0.3}MnO_3$ thin films and $PbZr_{0.52}Ti_{0.48}O_3/La_{0.7}Sr_{0.3}MnO_3$ heterostructures

5.2.1 Substrate temperature dependence

It is well known that the substrate temperature during film growth has prominent effect on the crystal structure of the ceramic thin film [62]. The thickness of LSMO thin films discussed in the following sections was about 200 – 250 nm. The relatively large fluctuation may be caused by the variation in optics alignments and the different ambient pressure during deposition. In our PLD set-up the laser beam is focused onto the curve surface instead of a flat one. The direction of the ejected plume is therefore very sensitive to the beam alignment. The laser fluence was kept at 6 J/cm^2. A laser pulse repetition rate of 10 Hz was used throughout. Under the above condition the films were grown for 10 minutes so the thickness per pulse can be estimated as 0.33 – 0.42 Å. The substrate temperature in this series of experiments was varied from 450°C to 700°C. The deposition ambient oxygen pressure was 200 mTorr. The X-ray diffraction patterns of the film grown in this temperature range are shown in figure 5.2. Strong (001) family peaks of LSMO film and LAO substrate are clearly seen. No other diffraction lines can be observed throughout the θ-2θ scans for the films grown at substrate temperature from 500°C to 700°C. The overlapped diffraction lines of (001)LSMO and (001)LAO are due to the small lattice mismatch between them (< 3%). Their (002) diffraction lines can be resolved and are found at around 47° - 48°. A small peak due to residue CuK$_\beta$ radiation is present at 43°. From the figure, it is observed that crystalline LSMO film cannot be

grown at temperature under 450°C. The films grown at 500°C or above, however, have good crystalline structures. The calculated out-of-plane lattice constants from the reflection angles for the LSMO films and LAO are 3.86 Å and 3.78 Å respectively. They deviate slightly from the lattice constants of LSMO (3.88Å) and LAO (3.79Å) as previously report [63]. It may be the distortion due to the contraction force at the interface arisen in small lattice mismatched heterostructures.

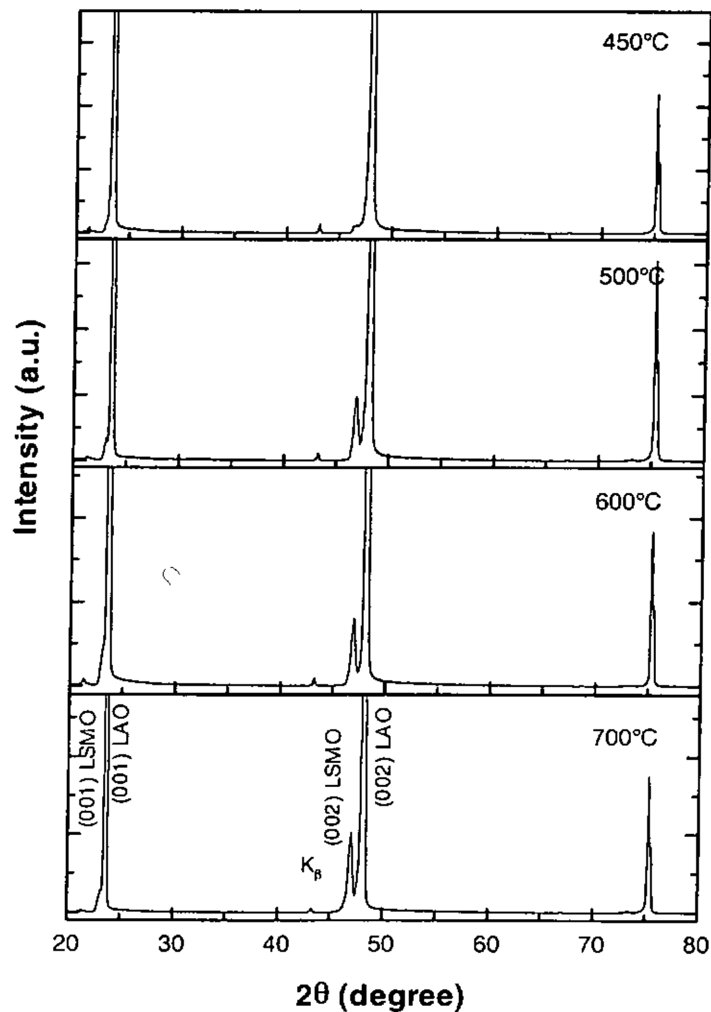

Figure 5.2 The θ-2θ scans of the LSMO films at deposition temperature from 450°C to 700°C.

The good crystalline quality of the deposited films is further confirmed by the rocking curve in ω scan. The rocking curves of the films grown at 500°C and 700°C display FWHM of 1.15° and 0.85° respectively and are illustrated in figure 5.3. It suggests the grown films have very good crystalline orientation and the crystallinity improves as the substrate temperature. Our present results on processing temperature is lower than the previous reports for $La_{0.7}Ca_{0.3}MnO_3$ (LCMO) and LSMO films, in which the growth temperatures are 650°C [64] and 700°C [65], respectively.

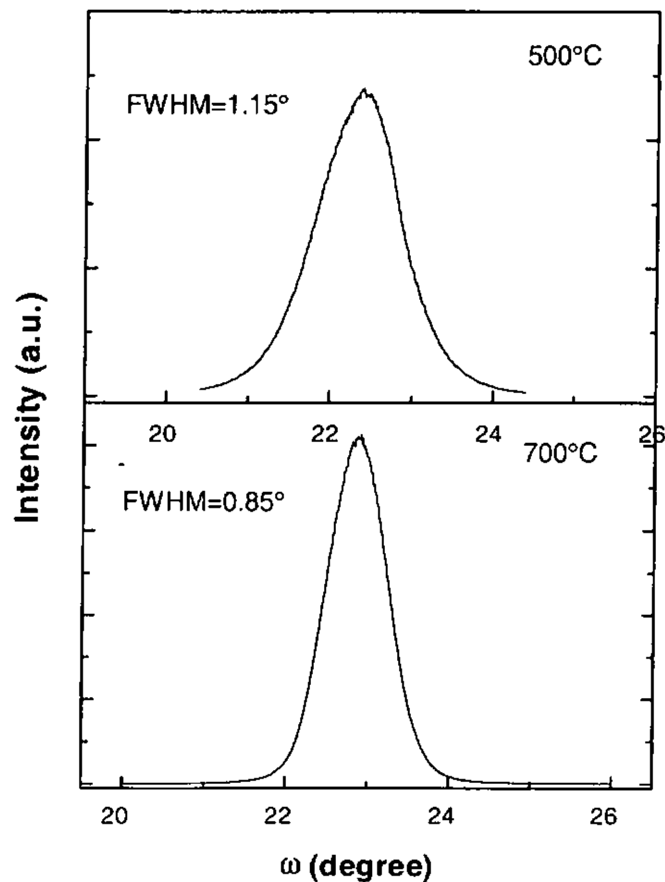

Figure 5.3 The rocking curves of the LSMO films grown at 500°C and 700°C.

The sharp and intense peaks in the normal θ-2θ scans and the value of FWHM of rocking curve in ω scans only give measures on the degree of orientation of the polycrystals of the films normal to the film surface. It is not enough to determine the epitaxy of the thin film. In order to further confirm the epitaxy of the films, 360° ϕ scans of the (220)LSMO and (220)LAO were carried out. Figure 5.4 shows the ϕ scans of the (220)LSMO and (220)LAO for the film grown at 500°C. As mention in chapter 4, this scan technique is used to confirm the in-plane alignment of the lattices between the film and substrate. From this figure, there are four peaks located at 90° apart showing the characteristic of four-fold symmetry. It reflects the cubic structure of both the LSMO film and the LAO substrate. The coincidence of these 2 sets of peaks suggests that the LSMO film is cube-on-cube sitting on the lattices of the LAO substrate. With the results from the previous θ-2θ and ω scans, the LSMO film are confirmed to be an epitaxial film grown on LAO substrate. Certainly, similar results for films grown at above 500°C are also obtained.

To conclude, epitaxial (001)LSMO film can be grown on (001)LAO substrate at the temperature as low as 500°C. This processing temperature is low enough to be compatible with Si processing technology. Our work has suggested that LSMO is potentially a suitable oxide material for integration devices. In general the crystallinity of LSMO improves with increasing processing temperature.

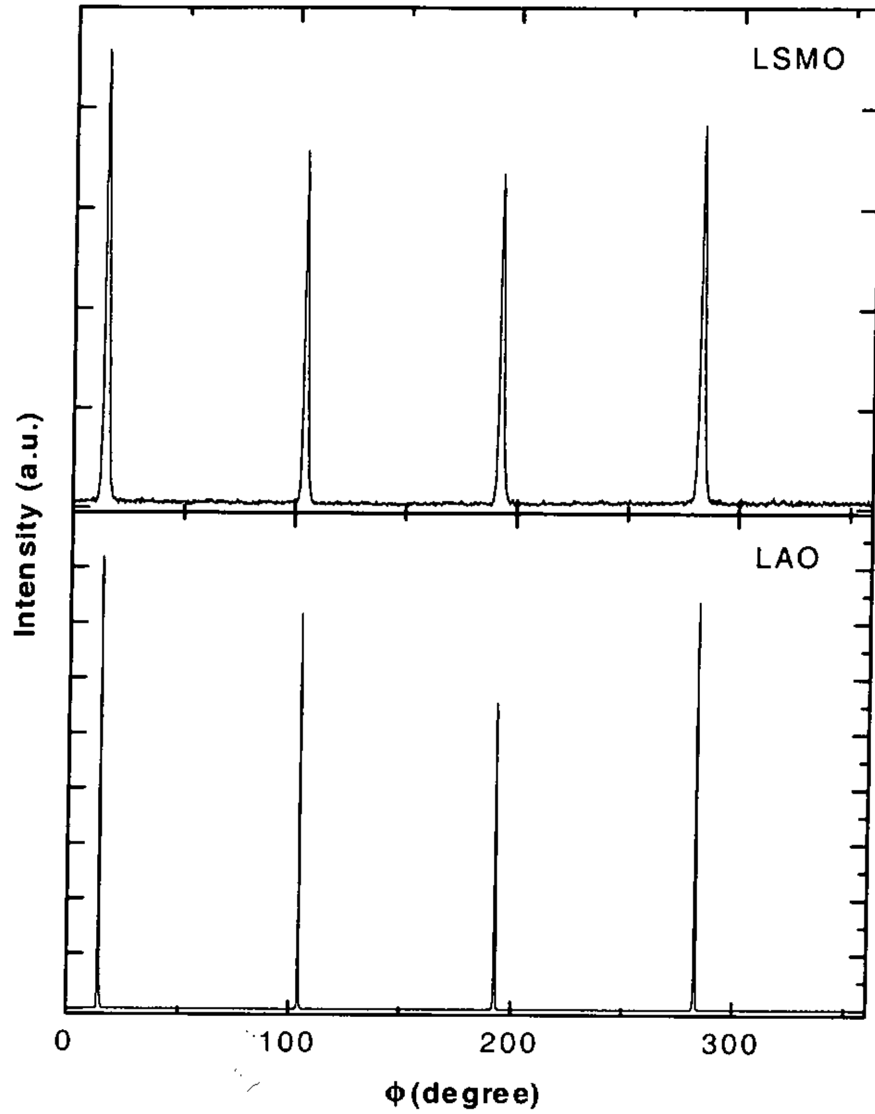

Figure 5.4 The φ scans of the (220) LSMO and (220) LAO for the film grown at 500°C

5.2.2 Deposition oxygen pressure dependence

The deposition oxygen pressure has a marked effect on the out-of-plane lattice constant of the LSMO films. Films grown under the deposition pressure from 0.1 to 200 mTorr at 700°C were investigated by the XRD. The θ-2θ scan results are shown in figure 5.5. It is clearly observed that the (001) diffraction lines of LSMO films and LAO substrate are resolved except for the film grown at 200 mTorr. There is a clear shift of (002)LSMO peak from 46.18° to 46.99° for films deposited at 0.1 mTorr and 200 mTorr respectively. The corresponding out-of-plane lattice constants change from 3.93Å to 3.86Å. The lattice constants are all deviated from the normal relaxed value of 3.88Å. This suggests that the lattice constant of LSMO films changes with oxygen content [66].

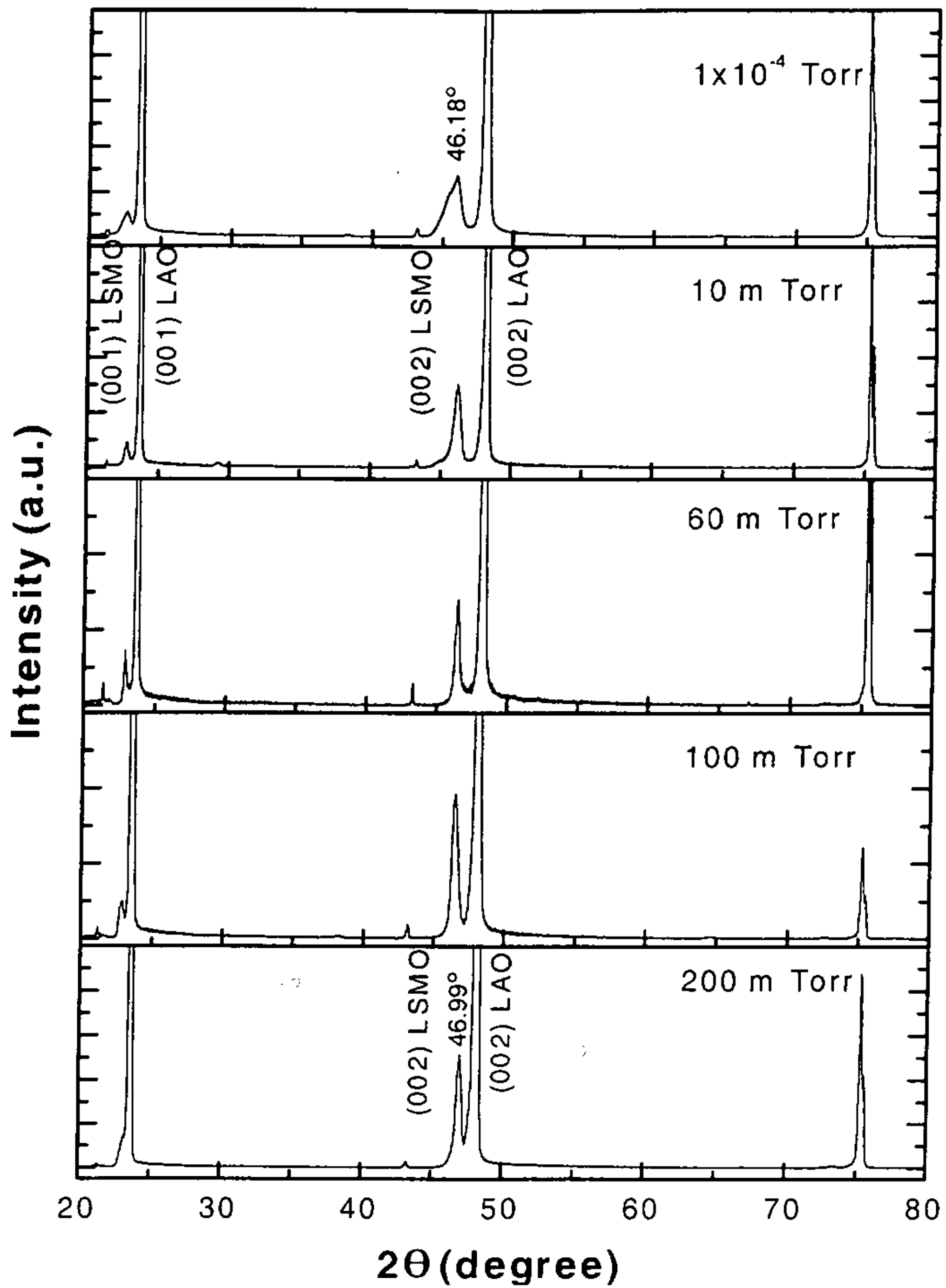

Figure 5.5 The θ-2θ scans of the LSMO films deposited under the oxygen pressure from 0.1 to 200 mTorr at 700°C.

5.2.3 Post-annealing temperature effect

In this series of experiments, the as-grown films were post-annealed under various ambient oxygen pressure from 4×10^{-6} Torr to 10 Torr at the same deposition temperature of 700°C for one hour. The θ-2θ scans of the film deposited under the oxygen pressure of 4×10^{-6} Torr, 10 Torr and the as-grown are shown in figure 5.6. Similar XRD structural characterization results were found. The (002) LSMO peak position remains basically unchanged by the annealing process. The FWHM of (002) reflection line in ω scan for those films were 0.87°, 0.86° and 0.85°, respectively. No substantial reduction of the FWHM was observed. It suggests that the grown LSMO films are not affected by further thermal.

From the results of the XRD structural characterizations, highly oriented crystalline LSMO films with good epitaxy have been grown on LAO substrate over a wide temperature range from 500°C to 700°C. The out-of-plane lattice constant and the corresponding oxygen content of the film can be tuned and decided during the film growth process. Once the crystalline LSMO films have been grown, it is highly stable against any subsequent thermal treatment. This last feature of LSMO makes it a highly desirable material for use in multi-layer device structure. Any subsequent deposition at different growth conditions will not affect the structural of the previously laid down LSMO layer.

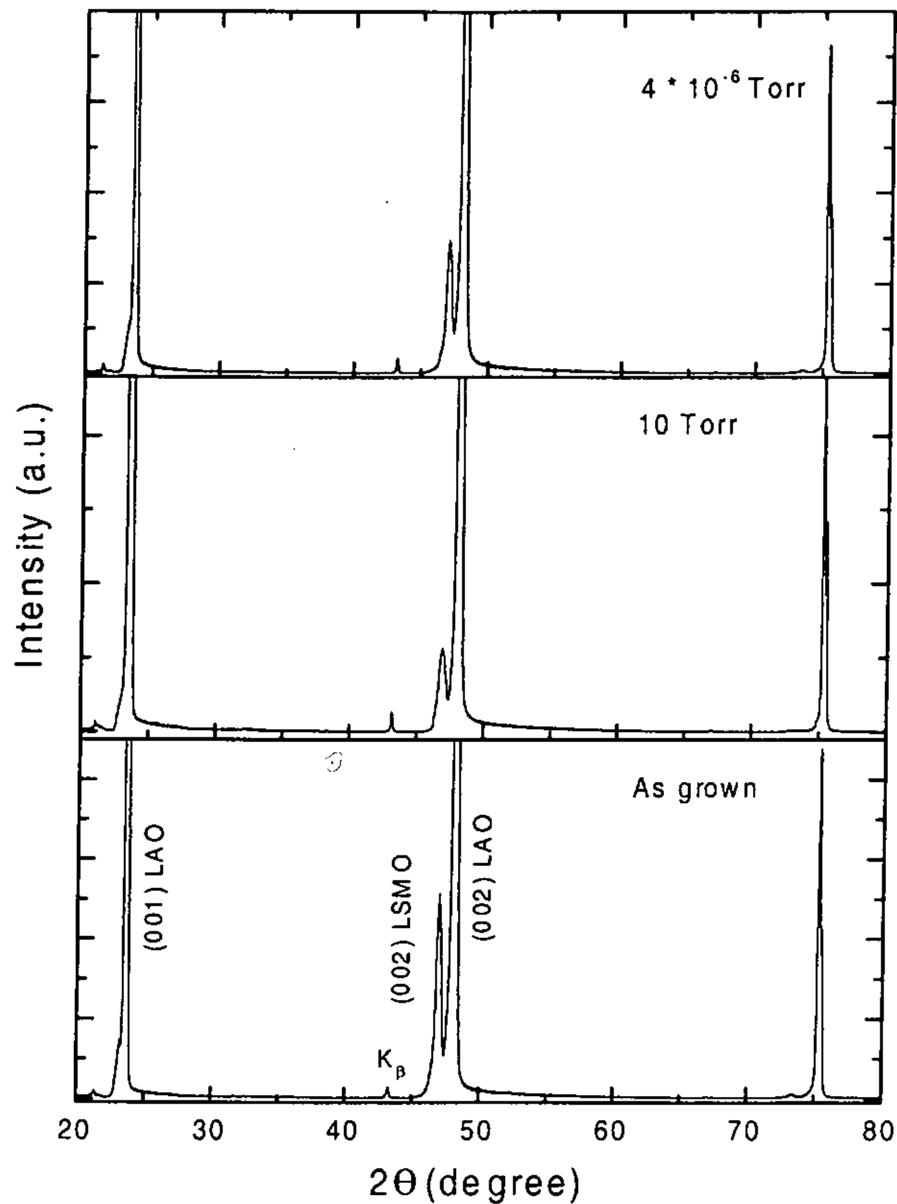

Figure 5.6 The θ-2θ scans of the LSMO films annealed under 4×10^{-6} Torr and 10 Torr at 700°C for 1 hour as well as the as-grown film.

5.3 Structural characterization of PZT/LSMO heterostructures

Based on the LSMO films grown at 700°C, PZT films were then in situ grown on top of it forming the PZT/LSMO heterostructures. The PZT films in this case were deposited under an ambient oxygen of 250 mTorr at 620°C and cooled down to room temperature at 760 mTorr oxygen pressure. The laser fluence was kept at 4 J/cm^2. The thickness of PZT was estimated to be about 500 nm. This PZT film thickness is comparable to the film thickness (400 nm) used in the FeFET fabricated by S. Mathews *et al.* [3]. In order to show that the grown PZT films is of pure single phase, a log scale of the θ-2θ scan of PZT/LSMO heterostructures is plotted as shown in figure 5.7. No trace of other PZT reflections was observed except the (001) family. The small peaks appeared around 40° and 42° are the reflections of K_β radiation of (002)PZT and (002)LSMO, respectively. The out-of-plane lattice constant of PZT is calculated to be 4.08 Å. The ω scans show that the FWHM of the (002)PZT reflection is 0.85°. It is smaller than the FWHM of the (002)LSMO, which is 1.08°. Furthermore, the epitaxy of PZT films are determined by the three ϕ scans on (202)PZT, (202)LSMO and (202)LAO reflections shown in figure 5.8.

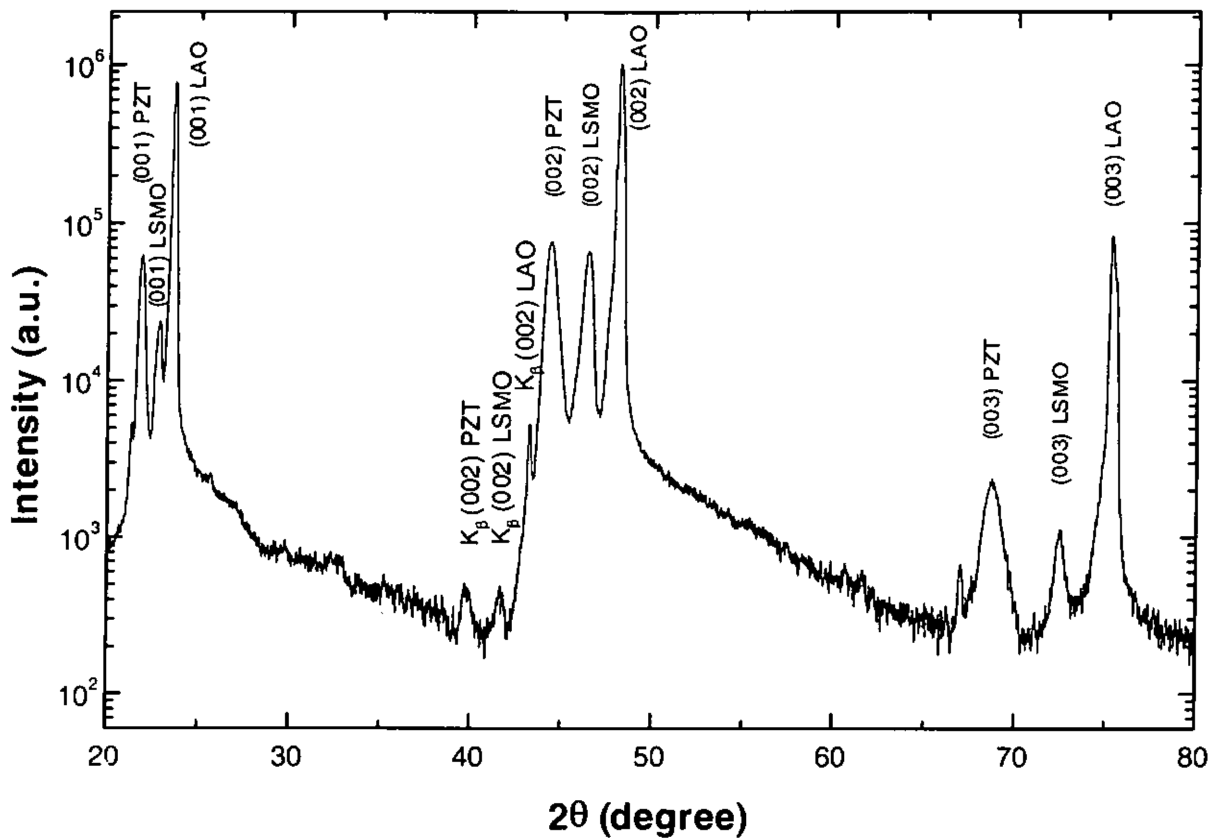

Figure 5.7 XRD specular θ-2θ scan from the PZT/LSMO/(001)LAO heterostructures. The PZT layer was deposited at 250 mTorr.

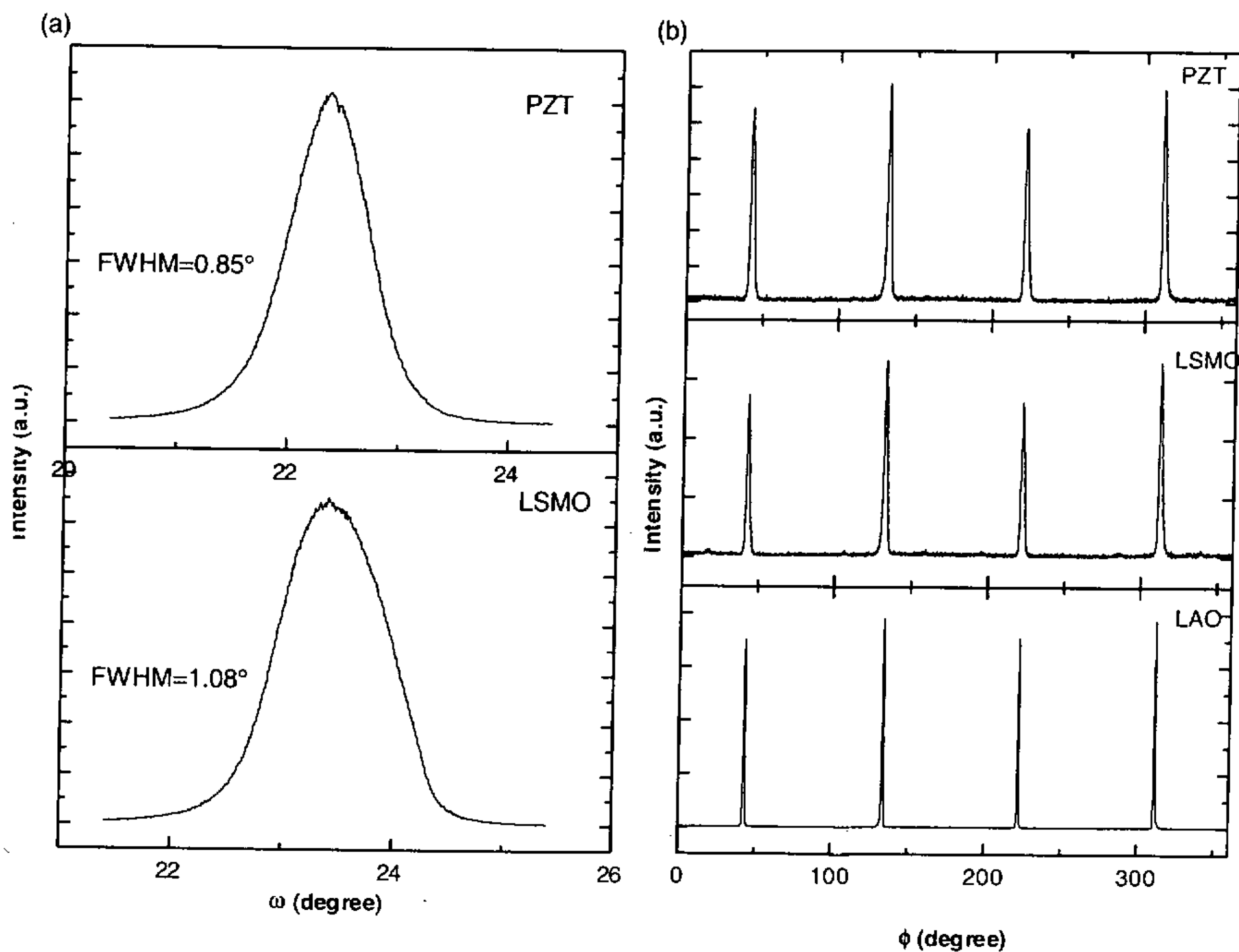

Figure 5.8 (a) ω scan rocking curves on the (002)PZT and (002) LSMO, (b) φ scans on the (202)PZT, (202)LSMO and (002)LAO reflection.

The thickness of the semiconducting LSMO films is a crucial factor in achieving high modulation in the FeFET since field effect may penetrate only into a shallow region in LSMO. PZT films grown on different thickness of LSMO templates were fabricated. The log scale of θ-2θ scans for the LSMO films grown at the thickness of 30, 40 and 55 nm are illustrated in figure 5.9. A clear (002)LSMO reflection is only observed of the film grown with thickness of 55 nm at 46.44°. There is a small peak of PbO reflection at 29° in figure 5.9b. It is properly due to the presence of particulate during this scan. Non-obvious PbO peak are observed in the other two scans. This PbO reflection also exists in the XRD pattern of the target as shown in figure 5.1, and is the result of excessive PbO added during target fabrication. The insets in the figure show ω scan rocking curve on (002) PZT and (002) LSMO reflections. The FWHM of the observable LSMO is 0.51°. It is because the nucleation of the film is layer-by-layer. The quality of epitaxy decreases with thickness. For the FWHM of (002)PZT on LSMO (55 nm) is 0.96° and decreases to 0.92° and 0.82° for the LSMO of 40 nm and 30 nm, respectively.

In conclusion, PZT film can be epitaxially grown on LSMO/LAO, and the thickness of LSMO film has an influence on the quality of PZT film and LSMO film itself. The film orientation increases with decreasing film thickness decreases. These results are useful for our design of FeFET to achieve large field effect modulation.

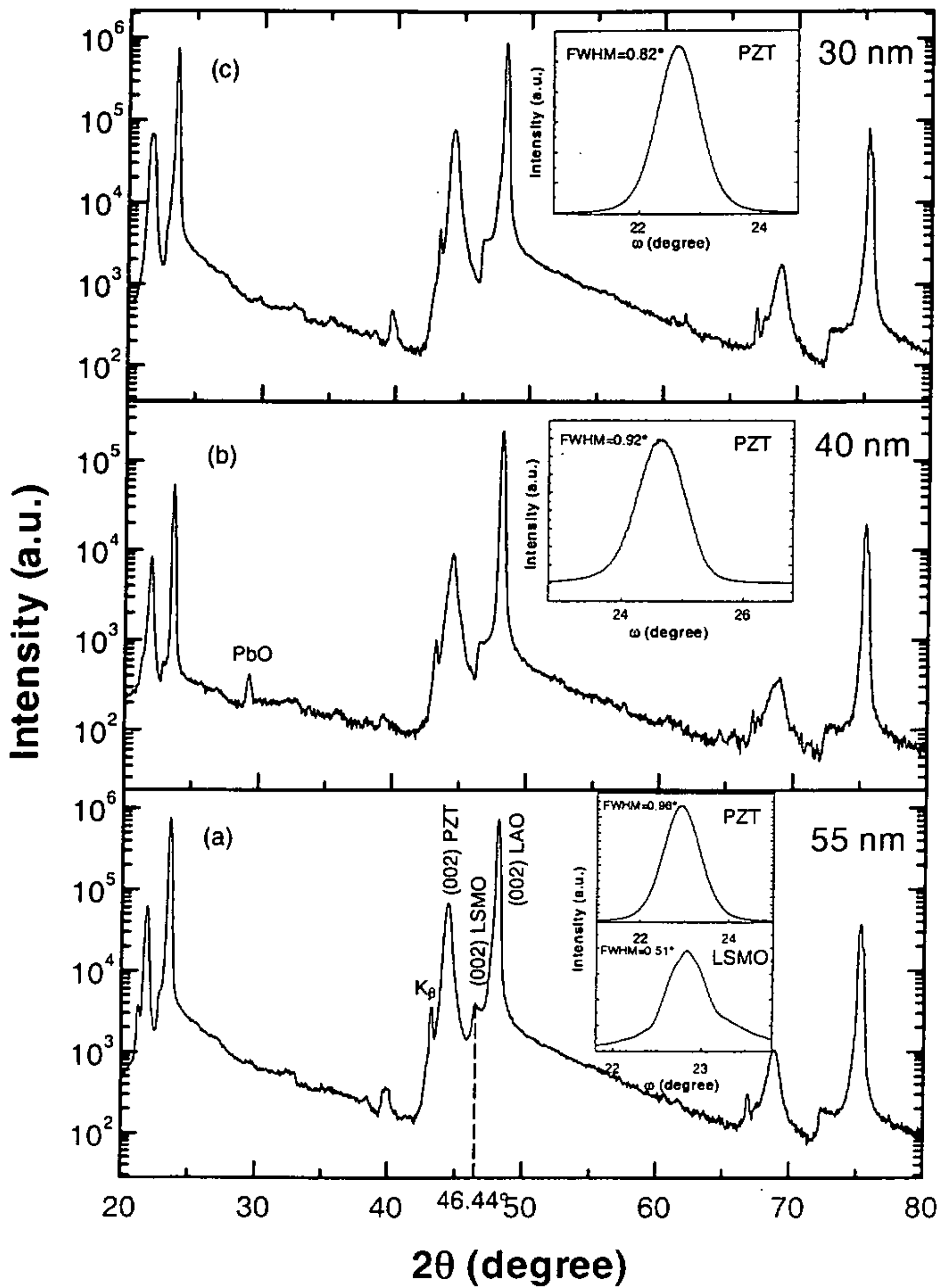

Figure 5.9 The XRD specular linear scans from PZT/LSMO/(001)LAO heterostructures with different thickness of LSMO (a) 55 nm, (b) 40 nm and (c) 30 nm. The insets in each plot show the ω scan rocking curve on (002)PZT as well as (002)LSMO in (a).

5.4 Surface Morphology analysis of PZT/LSMO heterostructures

XRD characterization provides only an average information of crystal structure in the thin film. The diffraction angle of θ-2θ scan and the FWHM of rocking curve reflect the macroscopic phenomenon of the region of film interacting with X-ray radiation. In order to obtain microscopic analysis, we used the scanning electron microscopy (SEM) to investigate the surface of thin film. The surface morphology of thin films is an important factor to determine the performance in electronic devices. Pinholes in ferroelectric films will cause severe leakage. The ferroelectric films will breakdown easily under electric field. It also shortens the retention of ferroelectric device.

The SEM images shown in figure 5.10 are the surfaces of 200 nm thick LSMO films grown under 200 mTorr, 40 mTorr and 3×10^{-4} Torr. The smooth surface with crack-free and fine grains is obtained under these deposition pressures. However, the outgrowths in the film of 200 mTorr are clearly observed. These outgrowths form during the recrystallization process when the substrate is placed inside the visible energetic plume [67]. As the deposition pressure is reduced, the visible plume expands and is in direct contact with the substrate. The image in figure 5.10b and c do not show out-growths at all.

(a)

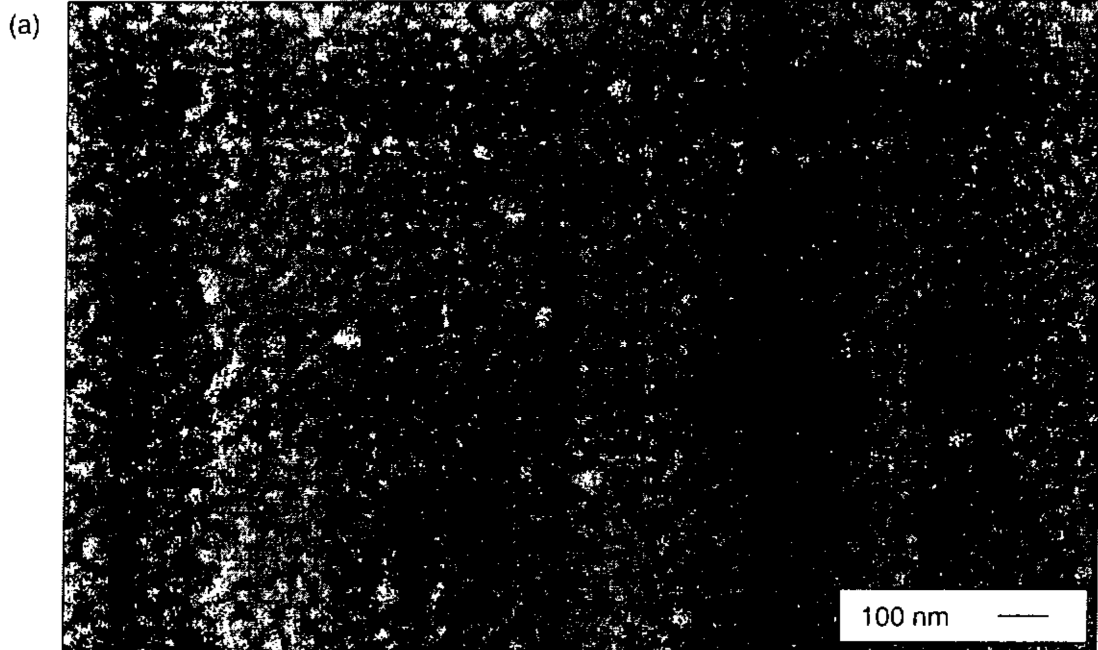

(b)

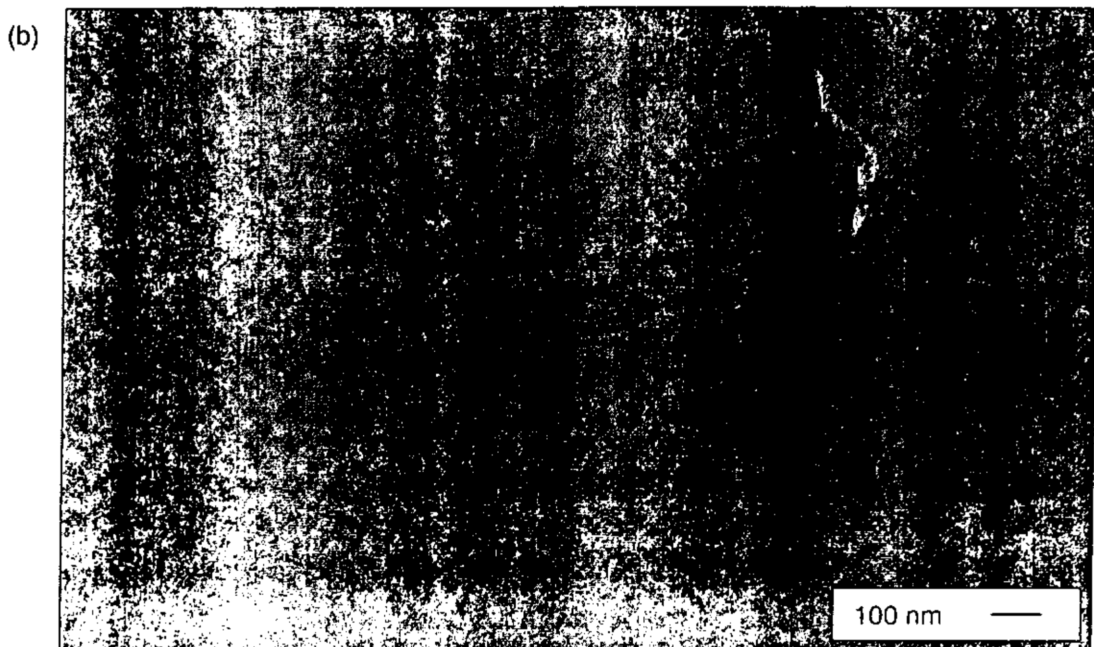

(c)

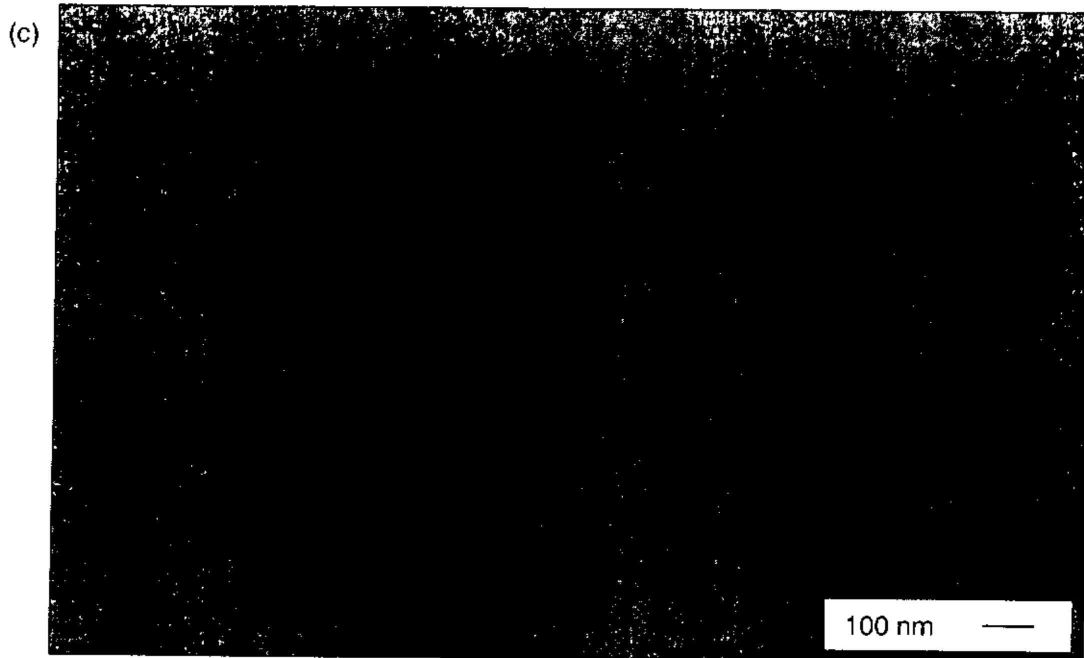

Figure 5.10 The SEM images of LSMO films deposited under (a) 200 mTorr, (b) 40 mTorr and (c) 3×10^{-4} Torr.

The SEM image of PZT is shown in figure 5.11. The surface is again smooth and crack-free. A little droplet with spherical shape is observed. The ball-shaped features are clearly the droplet directly from the target. It can be avoided by inserting a little shadow mask between the target and substrate during deposition. Figure 5.12 shows a cross-sectional SEM image of the PZT/LSMO/LAO heterostructures. Sharp interfaces of PZT/LSMO and LSMO/LAO are observed. The thickness of PZT and LSMO films is estimated to be about 600 nm and 40 nm, respectively.

In conclusion, smooth surfaces of LSMO and PZT films are obtained. No interdiffusion of PZT and LSMO are observed. From these results, the LSMO/LAO heterostructures have been characterized as good crystal structure, good surface

morphology and sharp interfaces. It can be achieved a good performance FeFET.

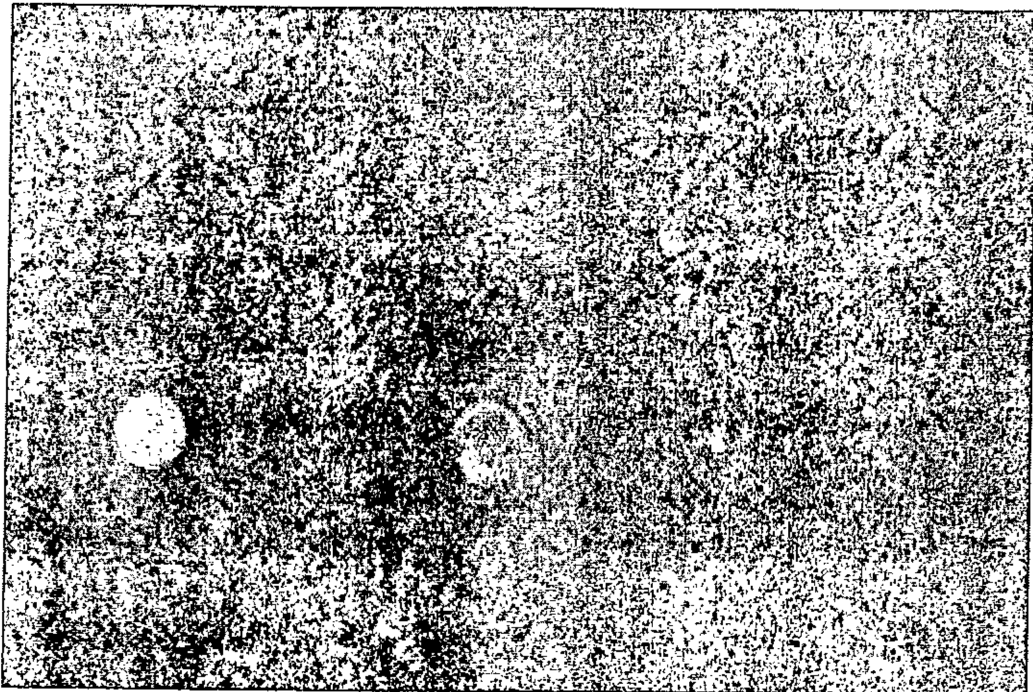

Figure 5.11 The surface morphology of PZT film.

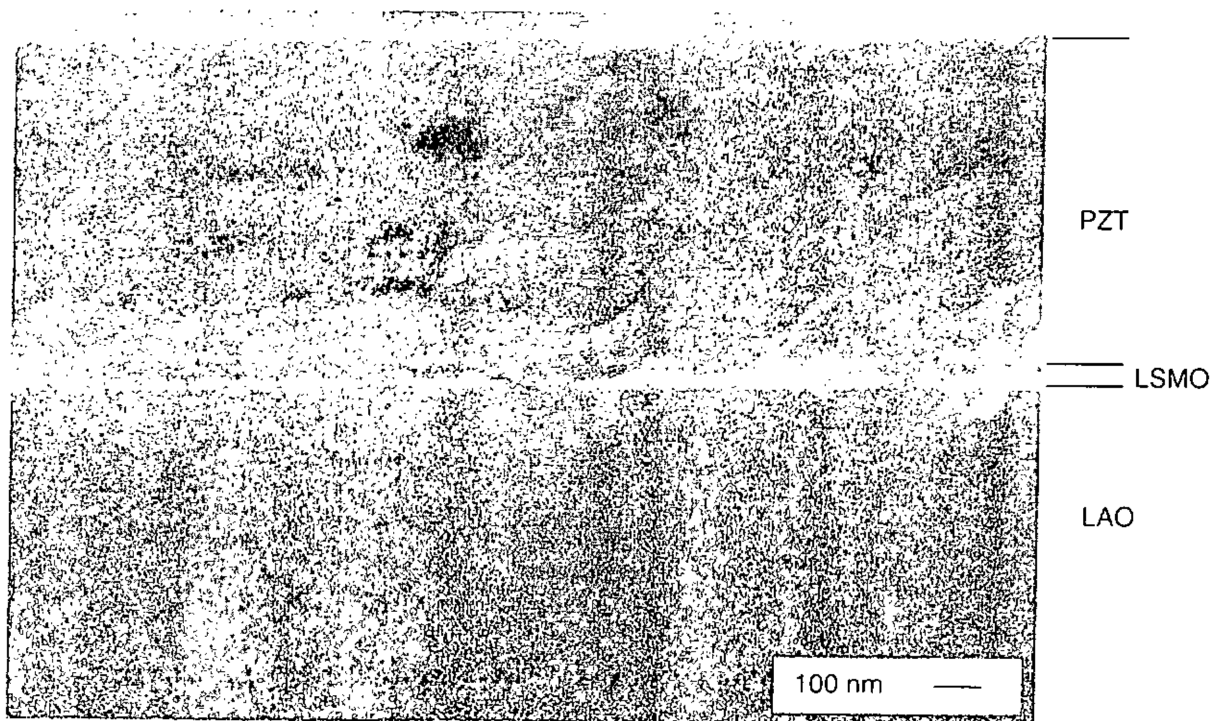

Figure 5.12 The cross sectional SEM image of PZT(600 nm)/LSMO(40 nm).

CHAPTER 6

ELECTRICAL MEASUREMENTS OF LSMO/LAO AND PZT/LSMO/LAO HETEROSTRUCTURES

For an effective FeFET operation, the remnant polarization of the ferroelectric layer should be maximized in order to provide a high enough electric field to control the conduction of the semiconductive layer after the external electric field is removed. In addition the ferroelectric film should also possess high resistance against switching fatigue and long charge retention time for registering and retaining the memory states. From the structural analysis discussed in the last chapter, the heteroepitaxial growth of the structure PZT/LSMO on LAO substrates has been verified. In this chapter, we will focus on the electrical characterization of the LSMO films with different growing conditions. The ferroelectric properties of PZT films and other electrical properties of the PZT/LSMO heterostructures will be included.

6.1 Electrical transport properties of LSMO films

LSMO films deposited at 500°C and 700°C under the ambient oxygen of pressure 200 mTorr exhibit vast difference in their resistivity. Both films are about 200 nm thick. The resistivity – temperature (R-T) from room temperature to 77 K is plotted as shown in figure 6.1. Both of these LSMO films display metallic like electrical behaviour. The resistivities at 300 K for films grown at 500°C and 700°C are $1.63\times10^{-4}\,\Omega m$ and $7.8\times10^{-6}\,\Omega m$, respectively. This is almost two orders of magnitude difference. It can be ascribed

to the poorer crystallinity of the films grown at 500°C than that grown at 700°C. The grains in the film is not well aligned, for the FWHM of (002) reflection for the LSMO film grown at 500°C is 1.15°. It causes large grain boundary in the film, resulting in a larger potential barrier between two grains. On the other hand, the crystallinity of the film grown at 700°C is better and the FWHM of (002) reflection is only 0.85°. Therefore, we used 700°C as the deposition temperature for all subsequent LSMO films growth.

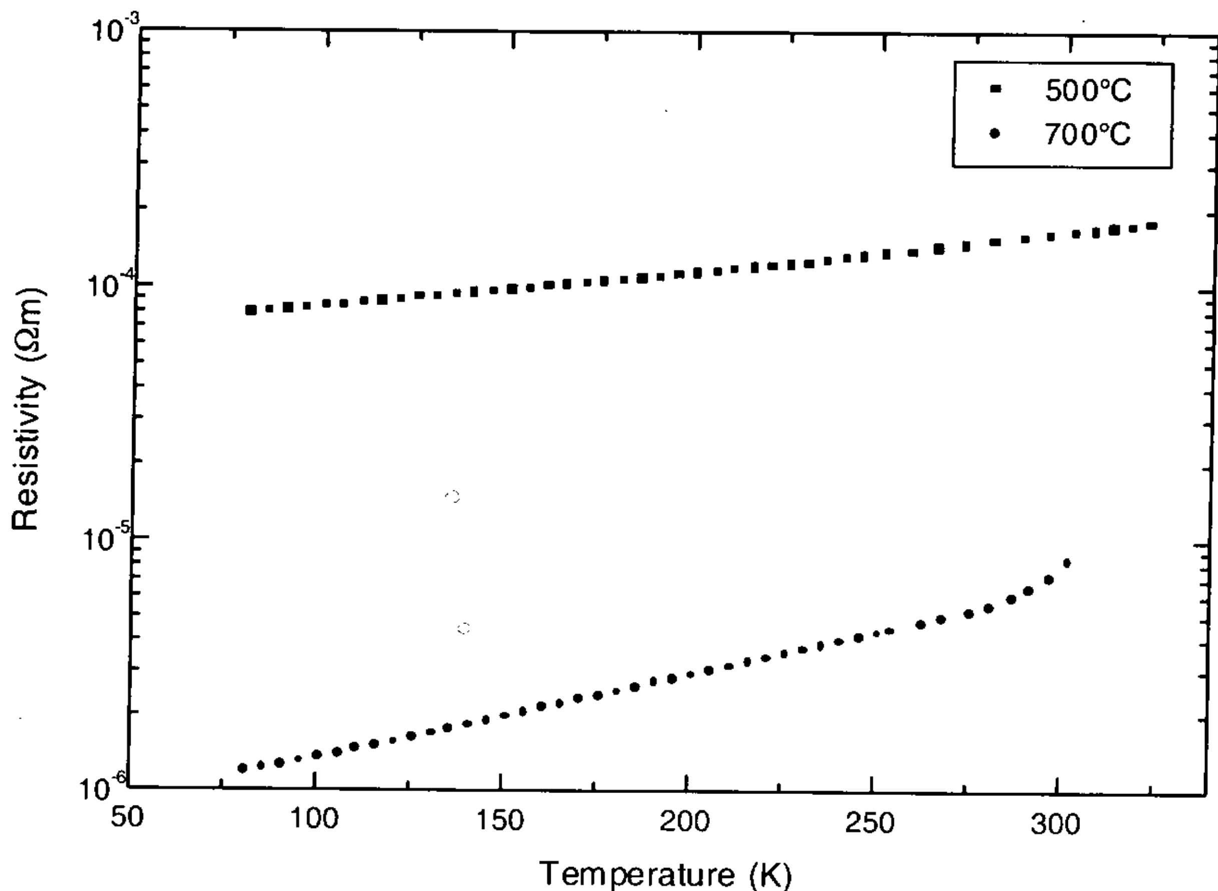

Figure 6.1 Resistivity vs temperature of LSMO films deposited at 500°C and 700°C under the ambient oxygen pressure of 200 mTorr.

A series of LSMO films were grown at 700°C under a wide range of ambient oxygen pressure from 0.1 mTorr to 200 mTorr. The film thickness for these LSMO films was estimated to be 200 nm. The oxygen content in the epitaxial LSMO films can be well controlled during PLD process by varying the deposition oxygen pressure. Similar effect has been reported for the $La_{0.7}Ca_{0.3}MnO_3$ system [68]. The resistivity of LSMO films displays an oxygen content dependence as shown in figure 6.2. The films grown at above 60 mTorr are all metallic like at room temperature. The metal-semiconductor transition temperature is down shifted to about 260 K for the film grown at 0.1 mTorr. The resistivity at 300K for the film grown at 0.1 mTorr is 6.23×10^{-4} Ωm. It is much bigger than that of film grown at 200 mTorr. It can be attributed to the decrease in oxygen content and hence the decrease in Mn^{4+} concentration [69]. The decrease of oxygen content can also be reflected in the change of carrier concentration. Hall measurement was carried out to obtain carrier concentration of the LSMO films. Since LSMO is well known for its colossal magnetoresistance (CMR), the electrical transport properties of LSMO films is strongly affected by the applied magnetic field during the Hall measurement. However, the maximum magnetoresistance (MR) of LSMO occurs at the metal-semiconductor transition and is only 4-6% for a magnetic field of 0.32 T. Such a magnetic field strength is used in the typical Hall measurement and therefore the CMR has no significance on our results. The carrier density of the oxygen stoichoimetric film deposited at 200 mTorr is about 1×10^{22} cm^{-3} and the oxygen deficient film deposited at 0.1 mTorr has been reduced to 3×10^{19} cm^{-3}. As mentioned before, the increase of charge carrier is only achieved by negative poling at the gate

terminal. Therefore, an oxygen deficient LSMO film with high electrical resistance should be chosen for use as the semiconducting layer in order to obtain a large field effect modulation in the FeFET.

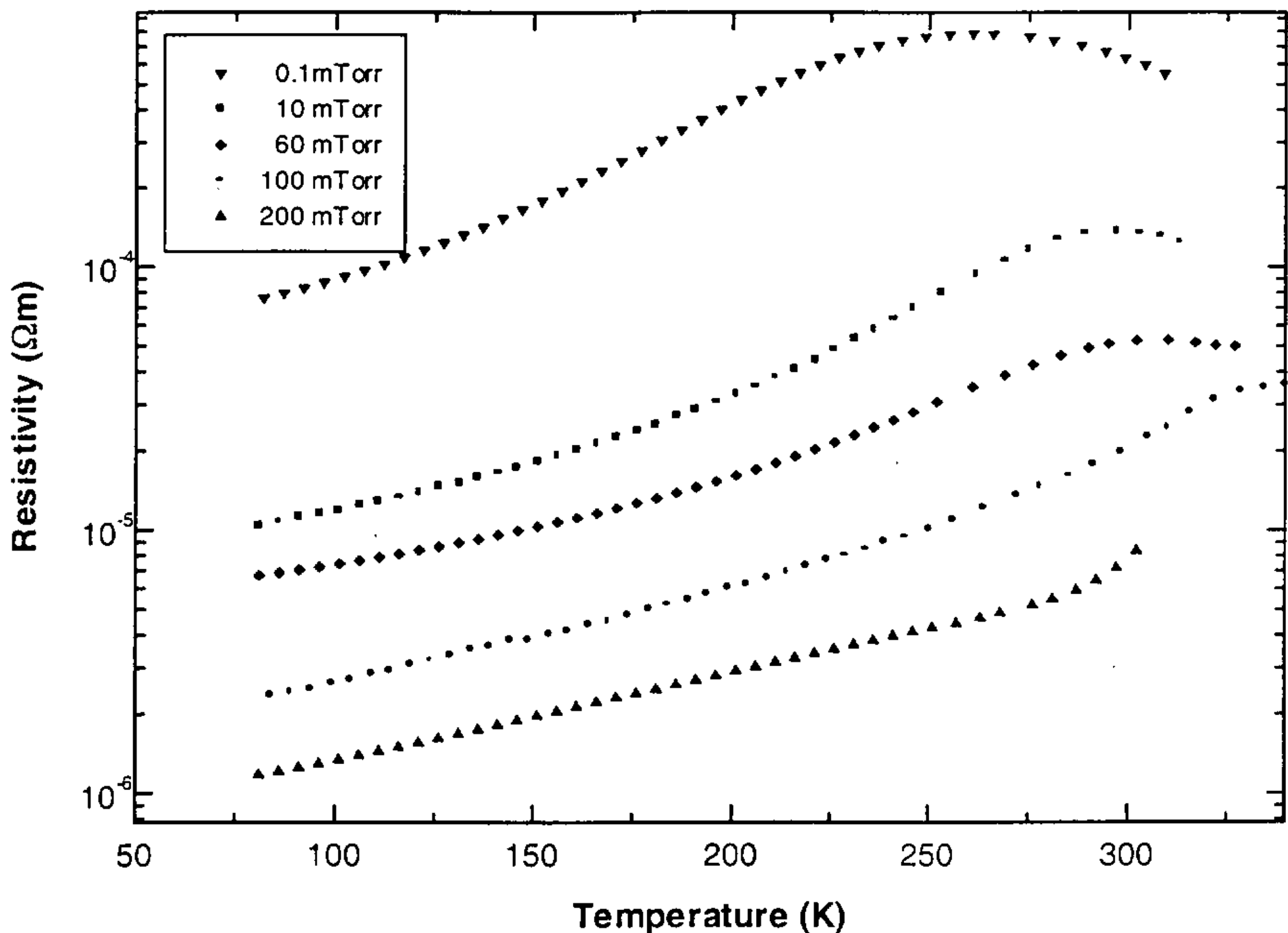

Figure 6.2 Resistivity vs temperature of LSMO films deposited at 700°C under the ambient oxygen pressure from 0.1 mTorr to 200 mTorr.

Many oxide films are very sensitive to the deposition oxygen background. For example, the resistivity of epitaxial LSCO films [70] at room temperature varies over by ten orders of magnitude. When the as-grown LSCO film are cooled down to room temperature at ambient oxygen pressure of 760 Torr and 10^{-4} Torr, the resistivities are 47 and 2.4×10^{10} $\mu\Omega$ cm, respectively. Other oxides such as LCMO and NSMO films [68] require post-annealing in oxygen background to obtain properties close to that of the bulk. LSMO films, however, have different response to the oxygen partial pressure during the annealing process. The XRD linear scans of LSMO films annealed under the oxygen pressure from 4×10^{-6} Torr to 10 Torr for 1 hour and an as-grown films have been shown in the last chapter. The 2θ angle of (002)LSMO diffraction lines of these films at around 47° seem unchanged. Apparently the oxygen content of the as-grown films does not changed with different annealing ambient pressure. The R-T curves of these films are shown in figure 6.3. It is noted that the resistivity of the films follows the same profile over a wide temperature range. It can be concluded that the LSMO film is highly stable against further post-annealing process.

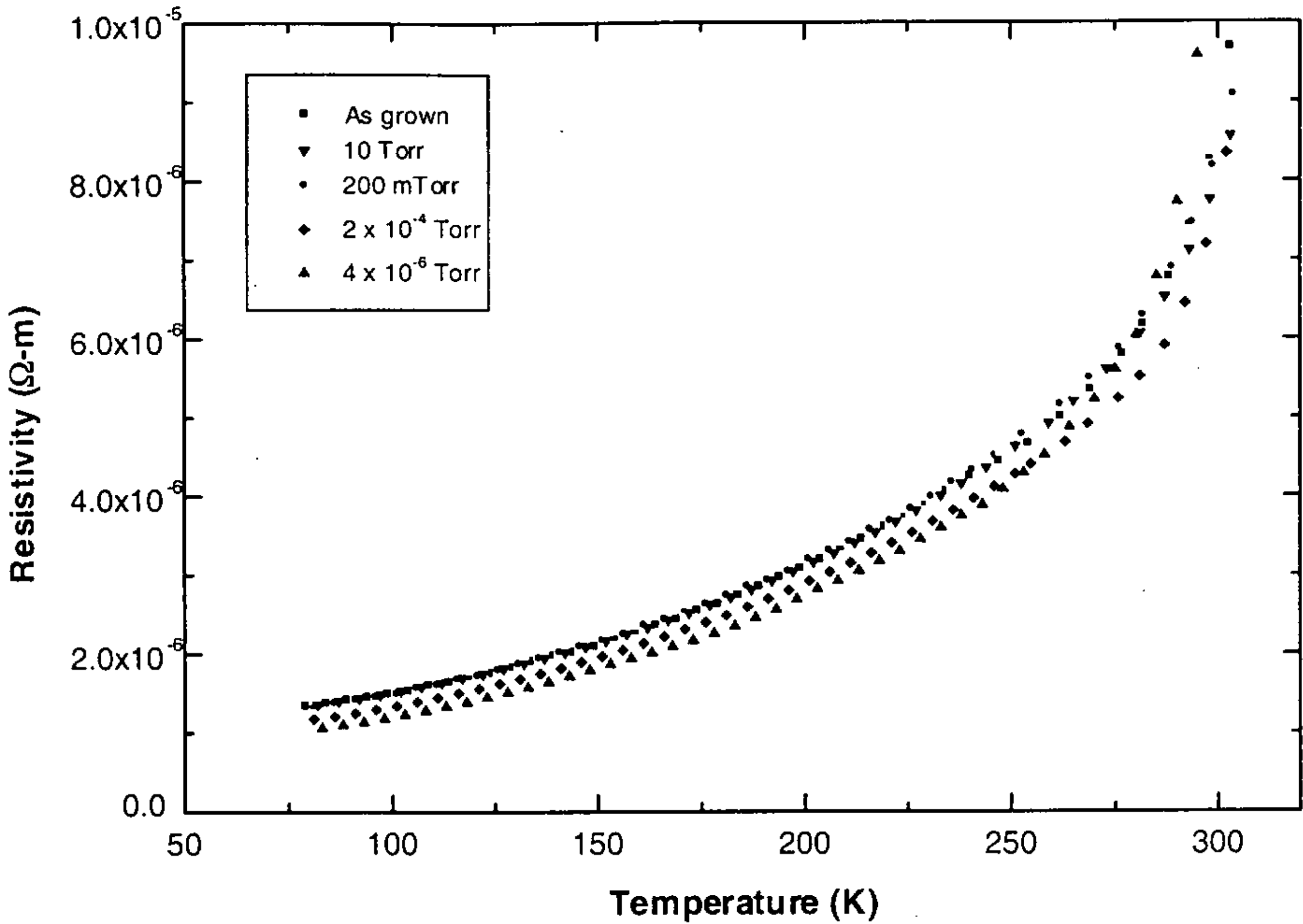

Figure 6.3 The R-T curves of LSMO films deposited at 700°C under a wide annealing oxygen pressure range from 4×10^{-6} Torr to 10 Torr, and a as-grown films.

Indeed the thermal stability of the resistivity of LSMO is further confirmed by measuring the resistivity of LSMO in the PZT/LSMO heterostructures. We used a more convenient two-point resistance measurement to compare the film resistance as shown in figure 6.4. The two LSMO films with thickness of about 200 nm were prepared simultaneously by the PLD process under the oxygen pressure of 30 mTorr. After that, one film was removed. The other was proceeded with the PZT deposition at the oxygen pressure of 200 mTorr. The as-deposited PZT film was then cooled down at 1 atm. oxygen pressure. The thickness of PZT was measured to be about 500 nm. The two R-T curves are shown in figure 6.5a. It is noted that except for the small shift of the metal-semiconductor transition temperature from 235 K to 249 K, the two profiles are essentially the same. In order to clarify the influence of the top PZT layer on the thin LSMO film, another set of measurement of LSMO and PZT/LSMO was carried out. The LSMO films here were grown at 0.3 mTorr oxygen ambient and hence were oxygen deficient. This LSMO film was estimated to be about 40 nm thick. The other deposition conditions were remained unchanged. The results of R-T measurement is shown in figure 6.5b. Although the metal-semiconductor transition cannot be observed in the measured temperature range, an up-shifted profile for the PZT/LSMO is clearly observed. The resistance in the LSMO film at room temperature is about twice of that in PZT/LSMO heterostructures. Both sets of measurements show that the oxygen deficient LSMO films became more "metallic like" after depositing oxygen stoichiometric PZT films on top.

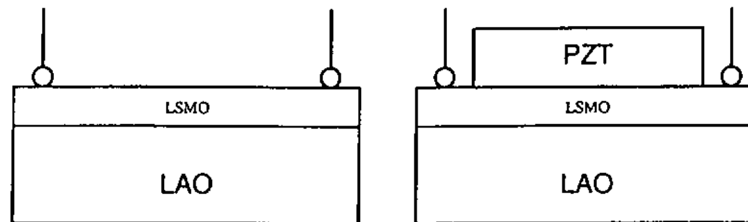

Figure 6.4 The schematic diagrams of two-point resistance measurement.

From the above results, it is clear that the oxygen content in LSMO films is mainly controlled by the oxygen pressure during deposition and is not affected by in situ annealing process, even though the in situ annealing pressure varies widely from 4×10^{-6} to 10 Torr. After depositing the PZT film onto the LSMO template at oxygen pressure of 200 mTorr and annealing at 1 atm. oxygen pressure, however, oxygen gain of the LSMO is evidenced by the resistivity measurements. It is a result similar to the previous report of Wu *et al.* [66], in which oxygen is lost from the oxygen stoichiometric LNSMO film after depositing a STO film in high vacuum below 2×10^{-4} mTorr. It causes a higher metallic-semiconductor transition temperature. This small increase, however, does not affect the film's electrical properties significantly. With careful control of the deposition pressure, desirable and stable electrical transport properties of semiconducting LSMO films may be obtained for FeFET application.

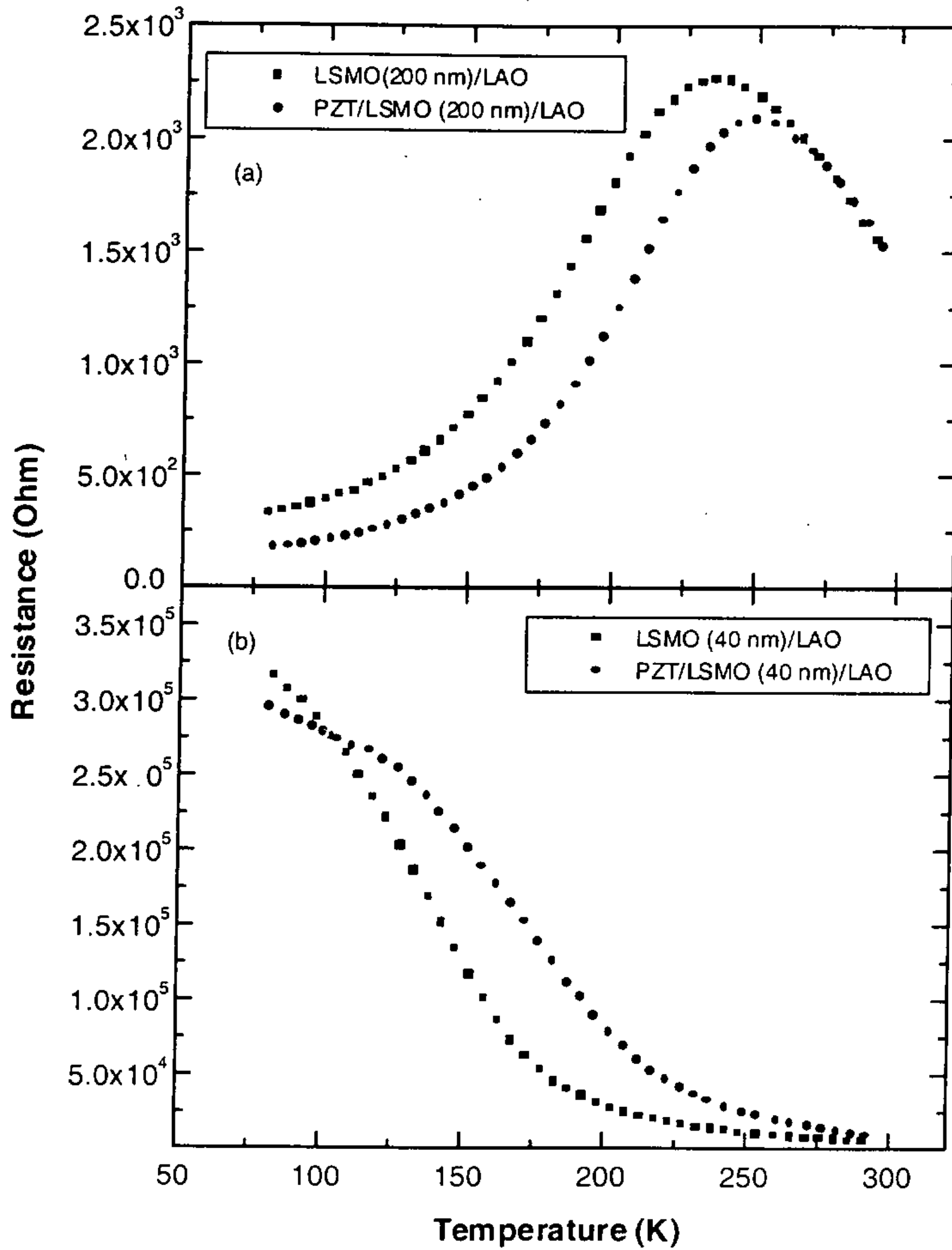

Figure 6.5 The R-T curves of LSMO films and PZT/LSMO heterostructures (a) for LSMO film with 200 nm thick deposited at 30 mTorr and (b) for LSMO film with 40 nm thick deposited 3×10^{-4} Torr films.

6.2 Ferroelectric properties of the Au/PZT/LSMO heterostructures

A non-volatile FeFET utilizes the ferroelectric properties of the ferroelectric layer to sustain the field effect in the semiconducting layer even after the external electric field is removed. For a high performance FeFET the ferroelectrics should have a high remnant polarization, a relatively small coercive voltage, a good resistance against fatigue and a long retention time. In this section, we will describe the fabrication process and the ferroelectric properties of Au/PZT/LSMO heterostructures.

6.2.1 Fabrication of Au/PZT/LSMO on LAO

Patterned layers of LSMO, PZT and Au were deposited on LAO substrate in succession forming a few Au/PZT/LSMO heterostructures on the same sample. The top Au electrodes were deliberately made small to minimize the chance of covering pinholes and large particulates, which were scattered randomly on the films' surface. Three top electrode configurations shown in figure 6.6 were used in our electrical measurement. In figure 6.6a, the LSMO and PZT layers were deposited by PLD technique. Gold electrodes with 0.2 mm diameter were ex-situ sputtered on top. This patterned heterostructures was used for ferroelectric measurement. For the pattern shown in figure 6.6b, LSMO film was fabricated into a double V shape and the channel conductance came mainly from the middle section. Narrow strips of PZT and Au were then deposited orthogonally across LSMO at this middle section. In this way we can reduce the ratio of channel resistance to parasitic resistances of source and drain. It will therefore enhance the modulation signal.

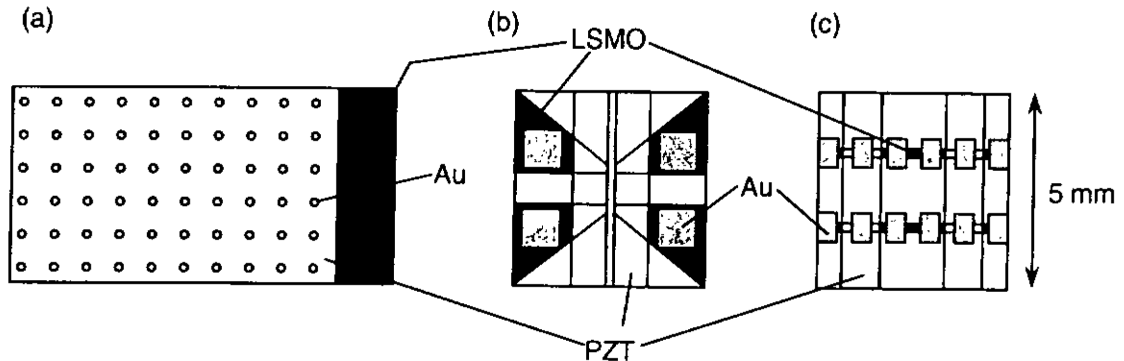

Figure 6.6 The patterns of Au/PZT/LSMO on LAO used for ferroelectric measurement and modulation test.

6.2.2 Ferroelectric properties measurement

PZT/LSMO heterostructures were fabricated on the LAO substrates with different patterns as described before. The LSMO films were grown at 700°C under an ambient oxygen pressure of 3×10^{-4} Torr. The PZT films were deposited at 200 mTorr oxygen pressure and at 620°C. They were then cooled down to room temperature under 1 atm. oxygen pressure. The PZT and LSMO films were estimated to have thicknesses of 500 nm and 40 nm, respectively. The top gold electrodes with 60 nm thick were then sputtered on top. The ferroelectric properties of these films were then characterized by the RT66A ferroelectric test system.

Figure 7 shows typical P-E loops measured from the Au/PZT/LSMO capacitor. It is seen that the capacitor display an almost square hysteresis loops. The five loops were obtained with driving voltage of 3, 4, 5, 6 and 7 V. The exact area of the top electrode was observed by a travelling microscope. The measured value is about 1.5×10^{-4} cm^2.

The remnant polarization (P_r) is about 48 μC/cm^2 and -P_r. is about –46 μC/cm^2. The coercive electric field (E_c) is about 57 kV/cm while -E_c is about -47 kV/cm. P_r saturates and a relatively low voltage of 4 V. It was noted that the capacitor has a larger positive coercive field than the negative one. It can be also observed in other samples for the LSMO films grown at higher oxygen pressures (not shown).

The asymmetry in the hysteresis loops, which could further cause the imprint failure, implies the existence of an internal electric field inside the PZT layer. However, the cause of the internal field in thin film ferroelectrics and the imprint are yet to be understood.

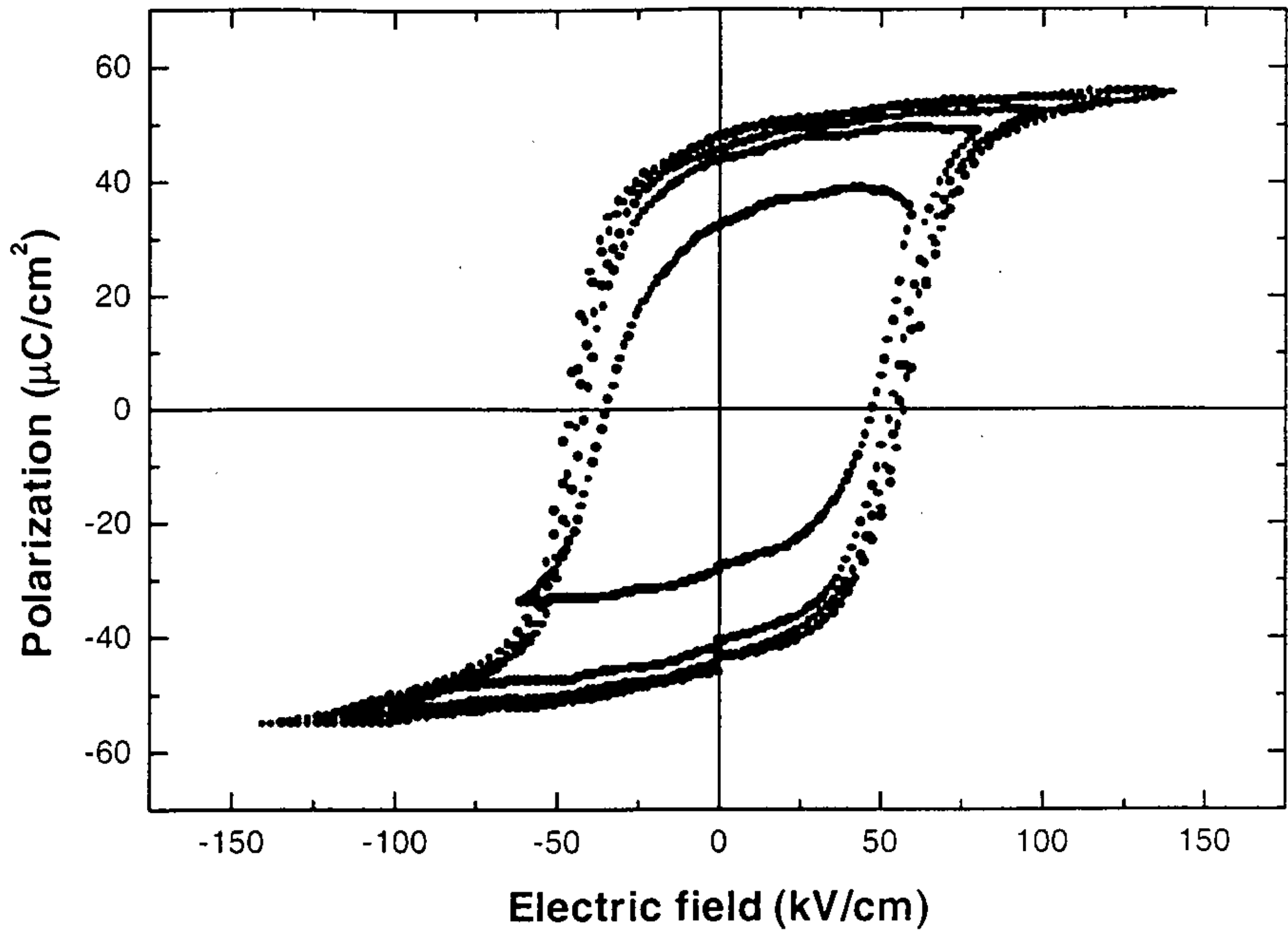

Figure 6.6 Typical polarization-electric field hysteresis loops of Au/PZT/LSMO capacitors with the maximum voltages of 3, 4, 5, 6 and 7 V.

It has been reported that for PZT and PLZT thin film capacitors the asymmetric loops were due to some process variables and the electrode configurations [71, 72]. It has also been demonstrated that after cooling at reduced oxygen ambient, epitaxial LSCO/PZT/LSCO capacitors develop more asymmetry in the hysteresis loops and a more preferred polarization stated directed towards the top electrode. The reduced oxygen pressure may induce more oxygen vacancies and the related deflect-dipole complexes in the PZT films, and these effects were suggested to cause the imprint. Wu et al. [73], on the other hand, reported the PZT films on LSMO templates at various deposition pressures. They observed no change in the E_c, and the voltage asymmetry of the loops for these pressures was the same.

The fatigue behavior and the degradation of ferroelectric properties due to polarization switching were tested at 60 kHz with a pulse width of 8.6 μs from the switching voltages of ±3 V to ±7 V. Figure 6.7 shows the fatigue behavior of Au/PZT/LSMO heterostructures. It is observed that the positive and negative polarization is quite symmetric. The PZT films showed only 8% polarization loss after 2×10^9 switching cycles at ±7 V. The larger polarization loss was obtained for low switching voltage. Figure 6.8 shows the P-E loops before and after fatigue test for the maximum voltages of 3 V and 7 V. The results in figure 6.8 agree with the results from the fatigue tests. At the test voltage of ±3 V, P_r changes from 31.91 to 15.49 μC/cm^2. It represents a 50% reduction. On the other hand, P_r only drops by <8% after fatigue test at 7V. It is believed that some charges may be trapped at the interface and a small field

cannot fully switch all the electric dipoles. It causes a rather flat P-E loop and substantial change in P_r.

The Au/PZT/LSMO heterostructures fabricated by us in the present studies show better fatigue test results than those reported by Wu *et al.* [73]. They used platinum (Pt) as top electrodes and a large polarization loss of over 70% was observed at about 10^7 cycles [7]. A further improvement in fatigue-free operation at low driving voltage is required. It is envisage that a smaller polarization loss can be obtained by making use of LSMO as the top electrode. It has been also reported that by increasing the switching frequency to 1 MHz, the polarization degradation decreases [28, 74]. Therefore a better understanding of the switching fatigue mechanisms is need in order to design a fast switching and high performance non-volatile FeFET.

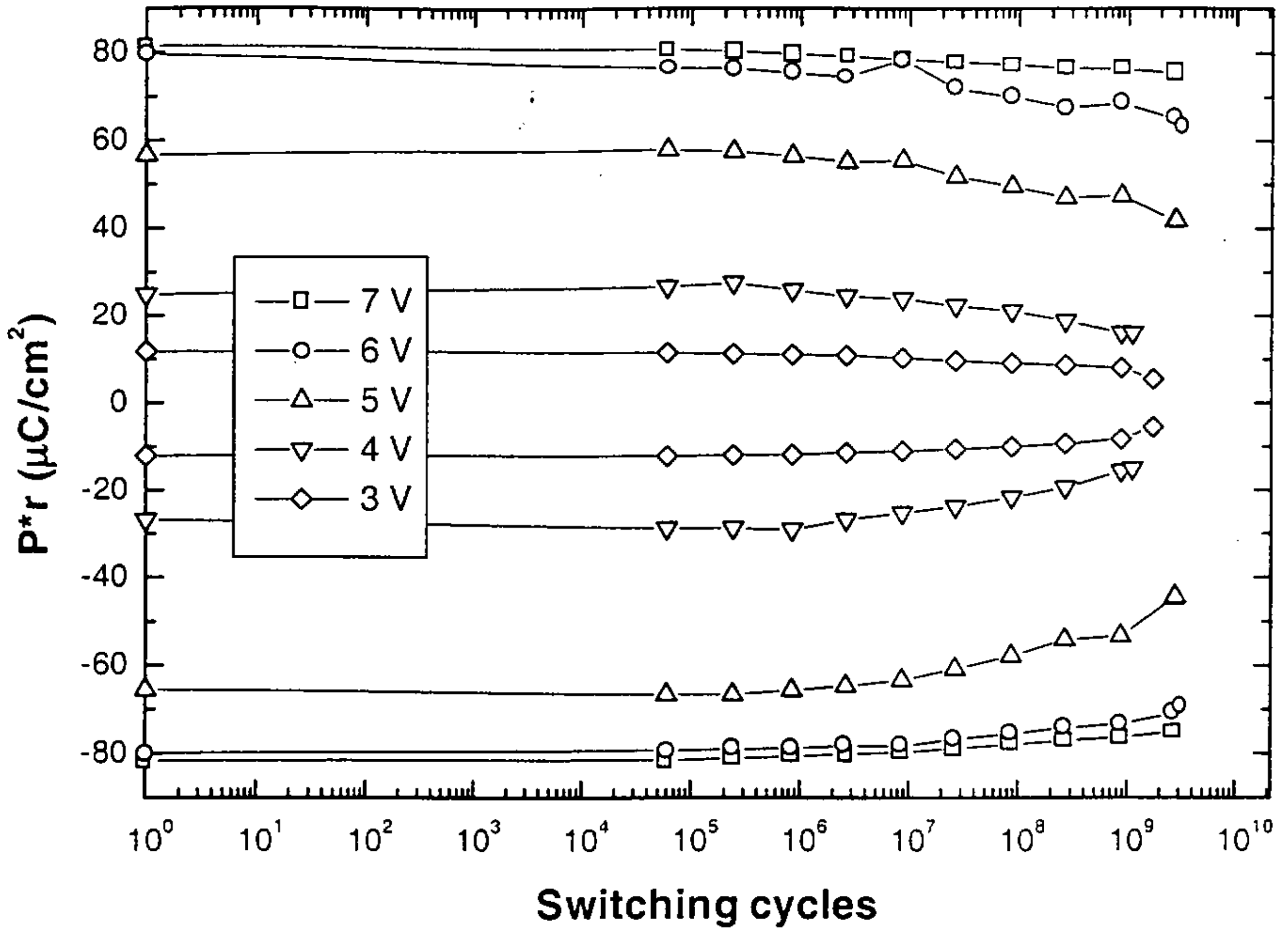

Figure 6.7 Fatigue properties of the Au/PZT/LSMO heterostructures for LSMO grown at 0.3 mTorr with thickness of 40 nm. The switching voltages are from 3 V to 7 V.

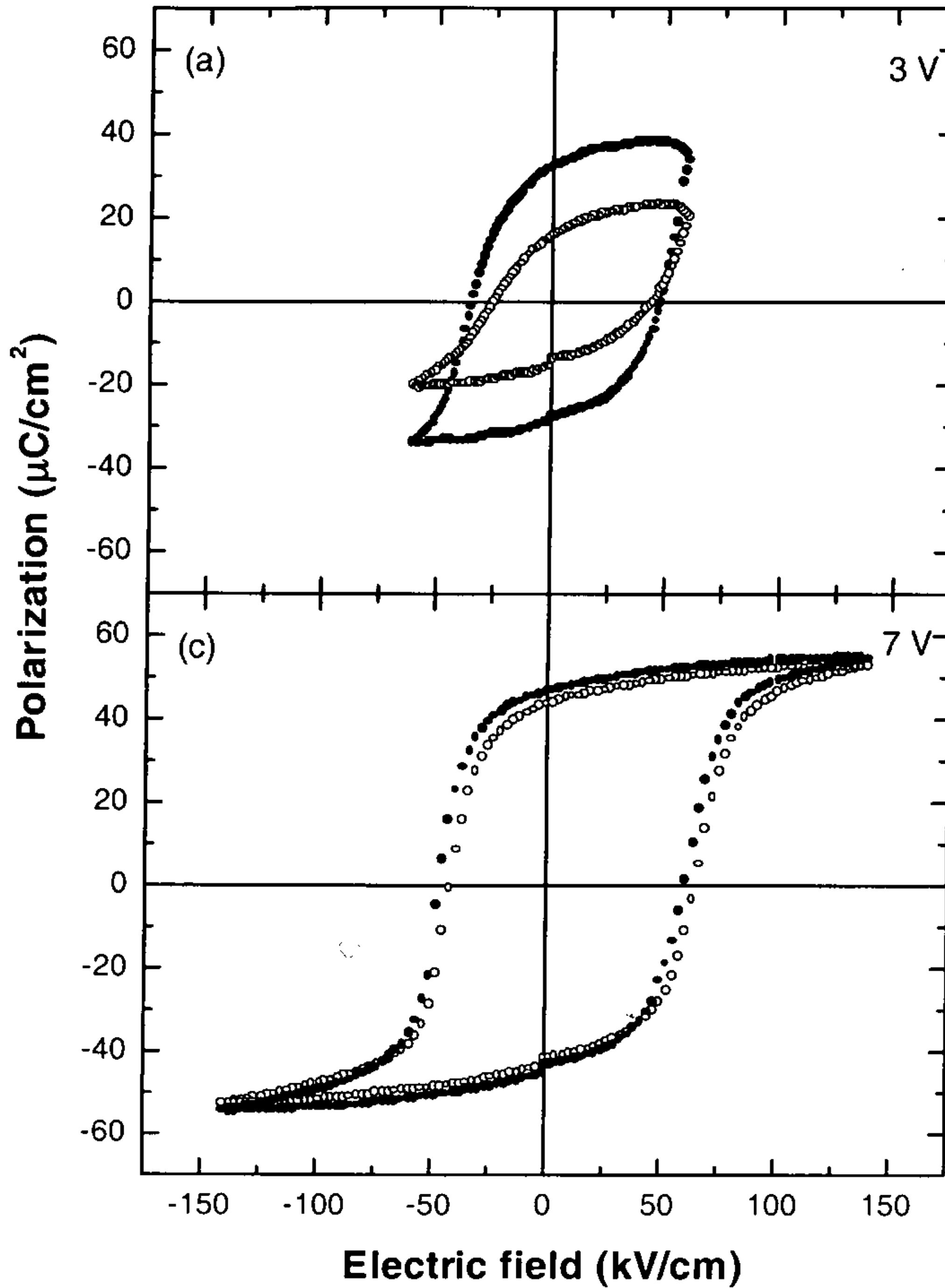

Figure 6.8 P-E loops just before and after the fatigue test of 3 V and 7 V for the switching cycle of 1.7×10^9 and 2.7×10^9, respectively.

The tests on the retention characteristics of the Au/PZT/LSMO heterostructures were also carried out by using the RT66A system. The Au/PZT/LSMO was written with a rectangular pulse of –7 V with pulse width of 8.6 μs and then read by two rectangular pulses of –7 V and 7 V, respectively. The pulse width was 2 ms. The time delay between the write pulse and the first read pulse is the retention time. The retention characteristics of the Au/PZT/LSMO is plotted in figure 6.9. The Au/PZT/LSMO heterostructures retained 91.9% of its initial polarization value after 1×10^5 s. The result was comparable to the result of Yin et al. [74], in which the LSCO/PLZT/LSCO retained 92.6%.

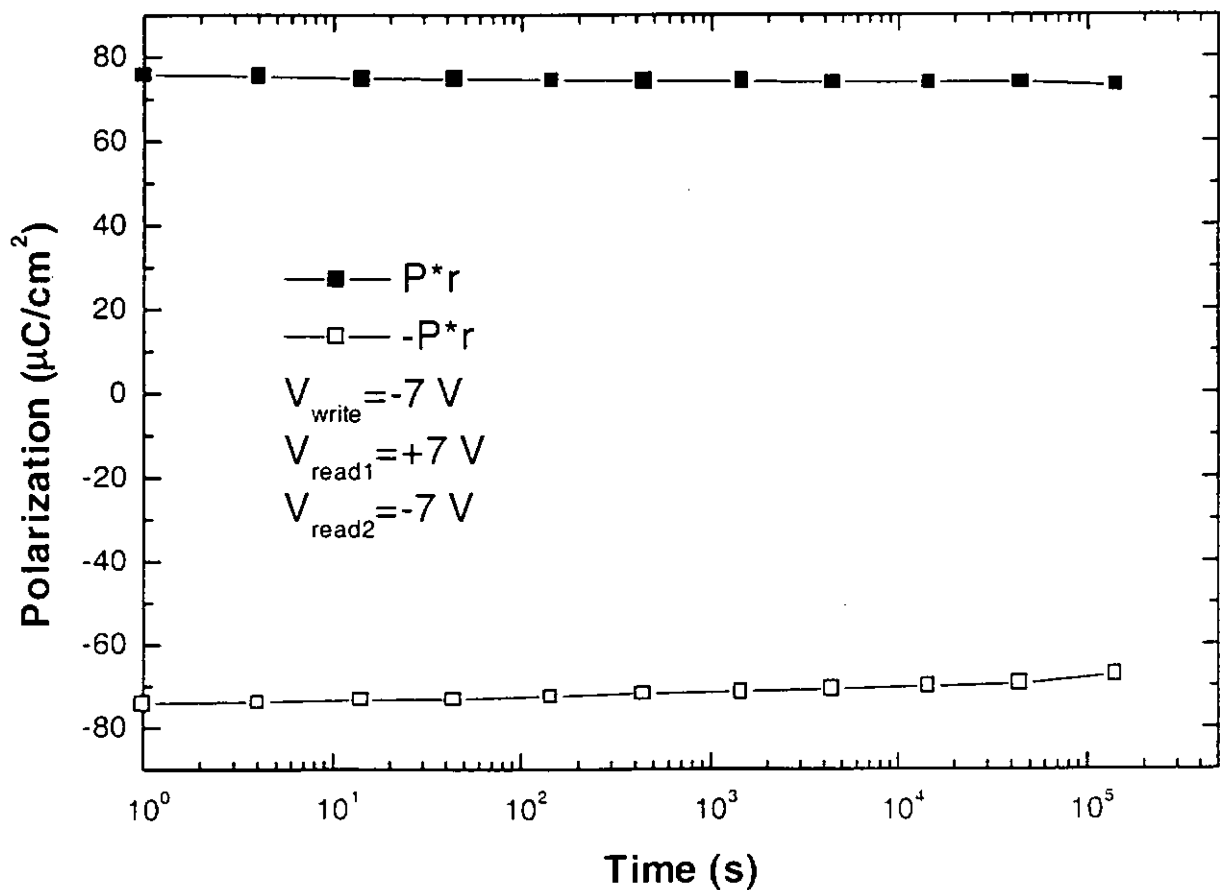

Figure 6.9 Retention characteristics of the FeFET Au/PZT/LSMO.

6.2.3 Other electrical properties of Au/PZT/LSMO heterostructures

Figure 6.10 shows the V-I characteristics of PZT film with cell area of 1.5×10^{-4} cm^2. Leakage current is less than 10^{-9} A at 7 V d.c.. It suggests a reasonably high dielectric breakdown voltage in our PZT film. The leakage current density at 1 V is estimated < 5×10^{-7} A/cm^2.

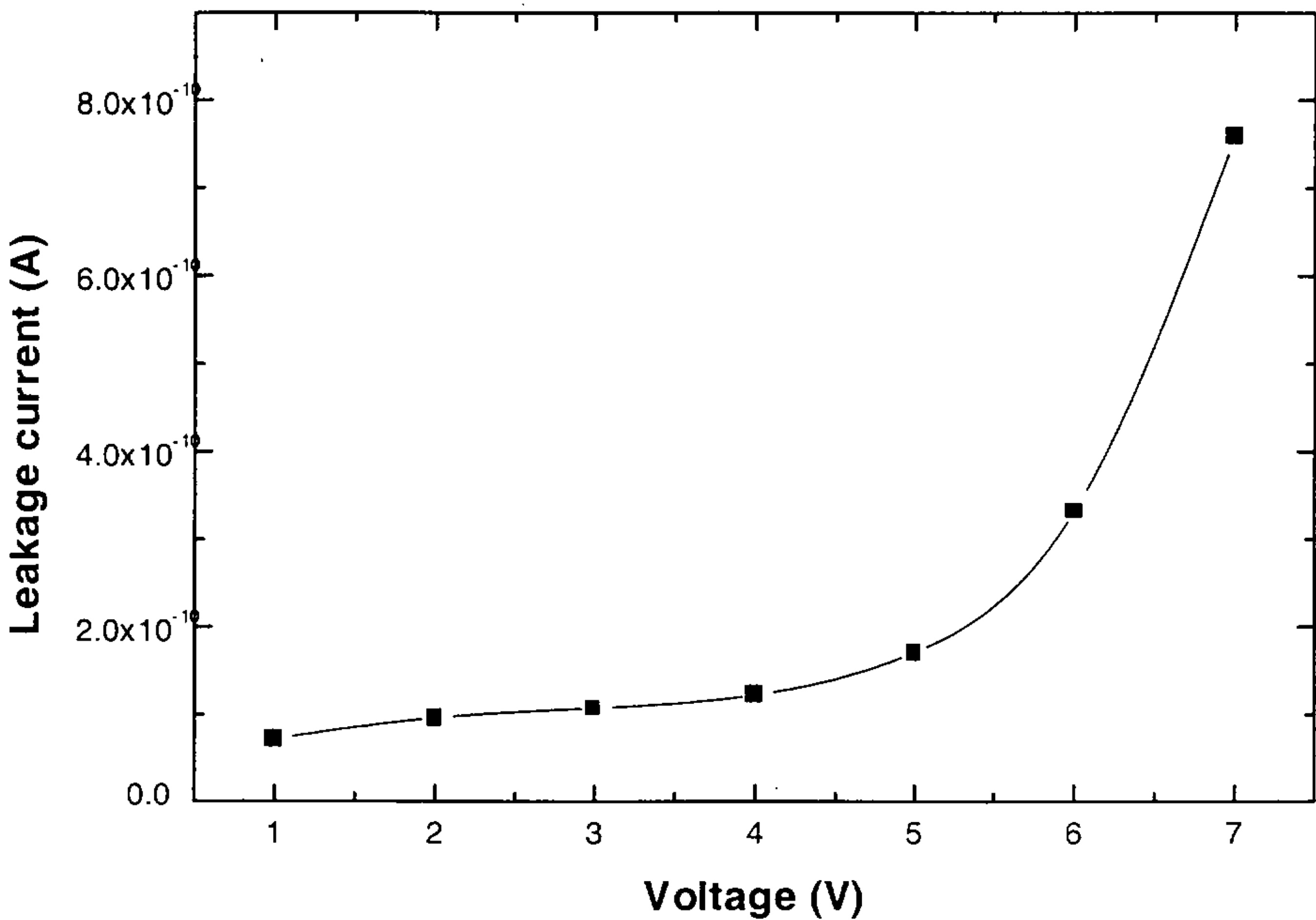

Figure 6.10 The V-I characteristics of PZT film with 1.5×10^{-4} cm^2 Au electrode.

As a last experiment in our present studies we have examined the field effect modulation in one of our Au/PZT/LSMO sample. In order to distinguish the contribution due to leakage current from the actual field effect modulation we have used an external power source to pole the PZT (either positively or negatively) as shown in figure 4.17. After poling we disconnect the power source from the sample altogether. In this way there will be absolutely no leakage current in the measuring circuit. The change in the measured signal can only be due to field effect modulation. The modulation against gate voltage plot is shown in figure 6.11. Modulations with observable magnitude starts at ±14 V. A maximum modulation 5.6% is obtained at the poling pulses of ±18 V with 0.1 ms pulse width. The smaller modulation of 4% at ±20 V may be due to partial breakdown of the PZT layer. In the case of maximum modulation the channel resistance varies from 132 kΩ with positive bias to 125 kΩ with negative bias and sustains this value of resistance for over 15 minutes. The need of large gate voltage and small modulation in our sample may be due to improper configurations and patterns. It causes the change of modulated-channel resistance small compared with the parasitic resistances between the source/drain and gate. A short retention time reflects a large leakage current in our sample.

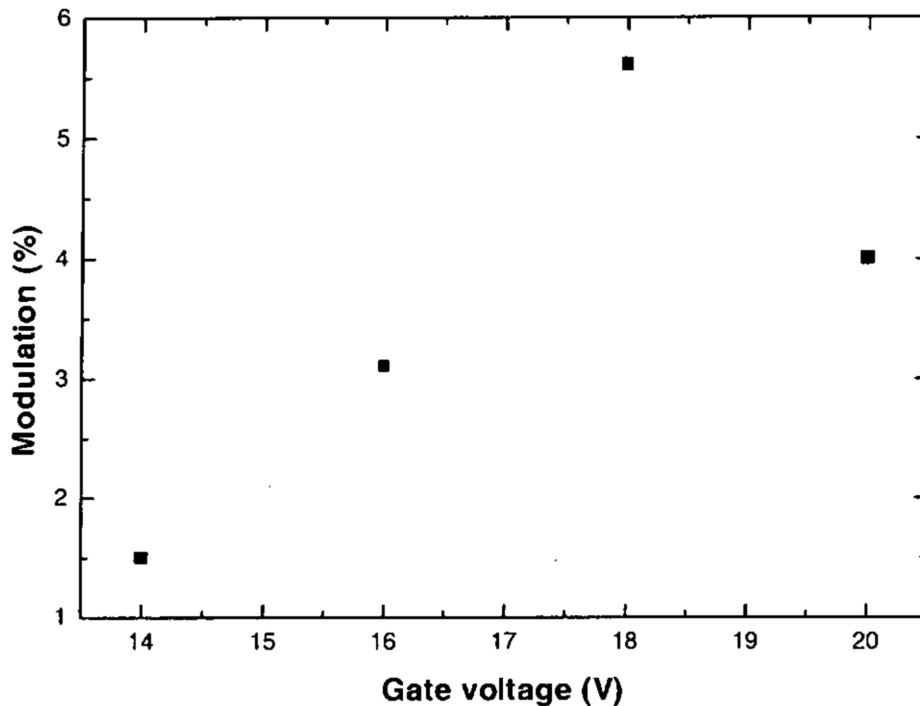

Figure 6.11 Modulation vs gate voltage for the Au/PZT/LSMO FeFET.

In conclusion, the Au/PZT/LSMO heterostructures has been fabricated on LAO substrate. The electrical transport properties of LSMO were characterized. The results of the R-T measurement agree with the XRD characterization. The conducting characteristics of the LSMO films can be controlled by tuning the oxygen content during deposition. It is insensitive to the post-annealing process. LSMO films, therefore, can be used as the semiconductor channel of FeFET. On the other hand, the ferroelectric properties of PZT films on semiconducting LSMO films were fully characterized. The PZT films reveal high remnant polarization, good fatigue property as well as long retention. A small remnant field effect modulation (5.6%) has been recorded. Our studies have shown that the Au/PZT/LSMO heterostructures can be used as FeFET for memory storage.

CHAPTER 7

CONCLUSIONS AND FUTURE WORK

In the present experimental investigation, excellent quality epitaxial LSMO and PZT/LSMO heterostructures have been successfully fabricated by the PLD method on (001)LAO single crystal substrate. The structural and electrical properties of both LSMO and PZT/LSMO films are characterized for potential use in FeFET.

The resistivity-temperature and Hall effect measurements show evidence that the conducting characteristics of the LSMO films can be controlled by tuning the oxygen content during the deposition. Post-deposition annealing has no effect on both the structural and electrical transport properties of the LSMO films – not even after they have been annealed at 10 Torr oxygen pressure for 1 hour. The electrical transport properties of LSMO films are slightly changed only after the PZT films growth. This change, however, has no substantial on the overall electrical properties of PZT/LSMO heterostructures. High quality LSMO films are also obtained at the temperature as low as 500°C. This low growth temperature of LSMO is compatible with the processing technology used in silicon industry. High quality LSMO films are therefore suitable materials for potential integrated device applications.

Epitaxial ferroelectric PZT films have been grown on LSMO templates. The crystallinity of the PZT films improves with decreasing LSMO film thickness. LSMO

thin films as thin as 30 nm have been fabricated. In this thickness the LSMO is expected to have larger field effect modulation.

A near square-shape P-E loop is obtained for the PZT/LSMO heterostructures with small sputtered Au electrodes. A large remnant polarization 48 $\mu C/cm^2$ and small coercive electric field 57 kV/cm are obtained at the maximum voltage of 7 V. A small leakage current of 5×10^{-7} A/cm^2 at 1 V is also recorded. In addition, polarization fatigue-free operation at up to and beyond 10^9 switching cycles and long charge retention time (91.9% in 10^5 sec.) were achieved. These results suggest that our films are of very good quality and can be used in FeFET. Indeed in the carefully designed and patterned Au/PZT/LSMO structure we did observe a semiconducting channel modulation of about 5.6%. This, of course, is too small for any practical uses. Optimizations of the PZT and LSMO layers are needed. Parameters such as PZT layer capacitance and charge concentration in LSMO matching requires fine adjustment. The effect of LSMO film thickness and its control demand further investigation.

In conclusion, LSMO films have been verified to be a better candidate than other oxides for used in FeFET. Its electrical characteriztics can be easily tuned during deposition. It has a relatively high thermal stability and can be grown at such a low temperature that is compatible with silicon technology. A novel all-perovskite FeFET structure using LSMO as the semiconducting channel was fabricated and characterized. The PZT films in the FeFET display good ferroelectric properties. Small leakage

current was measured. Remnant field effect modulation was also obtained.

It was noted that our PZT films tend to have relatively large leakage current and low permittivity. Such undesirable features can be ascribed to the PLD produced particulates littered on thin film's surface. In order to improve the electrical properties of these films, particulates can be eliminated by inserting a shadow mask between target and substrate during film growth. Besides, the trapped charges at the interface of Au/PZT should be minimized to reduce the polarization loss. In this respect, conducting oxide electrode should be used as the top electrode. Heteroepitaxial structure LSMO(metallic)/PZT/LSMO(semiconducting) will be an obvious choice and deserves serious consideration.

Other perovskite oxide films like PZT, BST and PMN have been grown epitaxially on MgO/TiN and STO/TiN buffered Si in our laboratory. LSMO has also been shown to grow epitaxially on these buffered Si at temperature as low as 580°C. Further studies should be focused on integrating PZT/LSMO FeFET on Si to form ultimate integrated non-volatile FeFET devices.

REFERENCES

1. Yukio Watanabe, *Appl. Phys. Lett.* **66**, 1770 (1995)

2. C. H Ahn, R. H. Hammond, T. H. Geballe, M. R. Beasley, J.-M. Rriscone, M. Decroux, Φ. Fischer, M. R. Beasley, *Science* **269**, 373 (1995)

3. S. Mathews, R. Ramesh, T. Venkatesan and J. Benedetto, *Science* **276**, 238 (1997)

4. S. B. Desu, H. S. Cho and P. C. Joshi, *Appl. Phys. Lett.* **70**, 1393 (1997)

5. H. M. Smith and A. F. Turner, *Applied Optics* **4**, 147 (1965)

6. W. Y Lee, J. Salem, V. Lee, T. Huang, R. Savoy, V. Deline and J. Duran, *Appl. Phys. Lett.* **52**, 2263 (1988)

7. R. G. Humphreys, J. S. Satchell, N. G. Chew. J. A. Edwards, A. G. Cullis and O. D. Dosser, *Less-Com. Metals* **151**, 271 (1989)

8. E. H. C. Parker, The Technology and Physics of Molecular Beam Epitaxy, Plenum, New York (1986)

9. S. M. Metev and V. P. Veiko, Laser Assisted Microtechnology, Springer, Berlin, Heidelberg (1994)

10. F. Breech and L. Cross, *Appl. Spect.* **16**, 59 (1962)

11. H. M. Smith and A. F. Turner, *Appl. Opt.* **4**, 147 (1965)

12. C. K. N. Patel, *Phys. Rev. Lett.* **12**, 588 (1964)

13. J. E. Geusic, H. M. Marcos and L. G. Uitert, *Appl. Phys. Lett.* **4**, 182 (1964)

14. R. F. Curl and R. E. Smalley, *Sci. Am. October*, 54 (1991)

15. J. T. Cheung, I.M. Gergis, J. James and R. E. DeWames, *Appl. Phys. Lett.* **60**, 3180

(1992)

16. J. A Greer and H. J. Van Hook, *Mater. Res. Soc. Symp. Proc.* **191**, 171 (1990)
17. A. Namiki, T. Kawai, K. Ichige, *Surf. Sci.* **166**, 129 (1986)
18. R. K. Singh, *SPIE* **2045**, 10
19. M. Hanabusa, *Mater. Res. Soc. Symp. Proc.* **285**, 447 (1993)
20. S. Metev, K. Meteva, *Appl. Surf. Sci.* **43**, 402 (1989)
21. P. Younger, "Executive Millennium Report: 1999 Roadmap: Solutions and caveats". *Solid State Technology* **43**, May (2000)
22. A. R. Srivatsa, C. L.Ygartua, S. Weinzierl, W. Johnson, T. Kaack, "Process development based on copper and low-k dielectric metrology". *Solid State Technology* **43**, August (2000)
23. D. H. Looney, *U. S. Patent* 2 791 758 (1957); W. L. Brown, *U. S. Patent* 2 791 759; I. M. Ross, *U. S. Patent* 2 791 760 (1957); J. A. Morton, *U. S. Patent* 2 791 761 (1957)
24. S. Y. Wu, *IEEE Trans. Electron Devices* **ED-21**, 499 (1974); Y. Higuma, Y. Matsui, M. Okuyama, Y. Nakagawa and Y. Hamakama, *Jpn. J. Appl. Phys. Suppl.* **17-1**, 209 (1978)
25. K. Sugibuchi, Y. Kurogi and N. Endo, *J. Appl. Phys.* **46**, 2877 (1975)
26. T. A. Rost, H. Lin and T. A. Rabson, *Appl. Phys. Lett.* **59**, 3654 (1991)
27. Subodh G. Ghonge, Edward Goo, R. Ramesh, T. Sands and V. G. Keramidas, *Appl. Phys. Lett.* **63**, 1628 (1993)
28. R. Ramesh, T. Sands, V. G. Keramidas, R. Haakenaasen and D. K. Fork, *Appl.*

Phys. Lett. **63**, 3592 (1993)

29. Takashi Nakamura, Yuichi Nakao, Akira Kamisawa and Hidemi Takasu, *Jpn. J. Appl. Phys.* **33**, 5207 (1994)

30. R. Dat, D. J. Lichtenwalner, O. Auciello and A. I. Kingon, *Appl. Phys. Lett.* **64**, 2673 (1994)

31. J. Lee, R. Ramesh, V. G. Keramidas, W. L. Warren, G. E. Pike and J. T. Evans, Jr., *Appl. Phys. Lett.* **66**, 1337 (1995)

32. H. N. Al-Shareef, B. A. Tuttle, W. L. Warren, D. Dimos, M. V. Raymond and M. A. Rodriguez, *Appl. Phys. Lett.* **68**, 272 (1996)

33. A. M. Dhote, S. Madhukar, W. Wei, T. Venkatesan, R. Ramesh, C. M. Cotell, *Appl. Phys. Lett.* **68**, 1350 (1996)

34. T. K. Song, S. \ggarwai, A. S. Prakash, B Yang, R. Ramesh, *Appl. Phys. Lett.* **71**, 2211 (1997)

35. E. L. Colla, D. V. Taylor, A. K. tagantsev and N. Setter, *Appl. Phys. Lett.* **72**, 2478 (1998)

36. E. L. Colla, Seungbum Hong, D. V. Taylor, A. K. tagantsev and N. Setter, *Appl. Phys. Lett.* **72**, 2763 (1998)

37. S. Aggarwai, A. M. Dhote, H. Li, S. Ankem and R. Ramesh, *Appl. Phys. Lett.* **74**, 230 (1999)

38. S. Aggarwai, I. G. Jenkins, B. Nagaraj, C. J. Kerr, C. Canedy, R. Ramesh, G. Velasquez, L. Boyer and J. T. Evans, Jr., *Appl. Phys. Lett.* **75**, 1787 (1999)

39. I. Stolichnov, A. Tagantsev and N. Setter, J. S. Cross and M. Tsukada, *Appl. Phys.*

Lett. **75**, 1790 (1999)

40. Yasushi Igarashi, Kouichi Tani, Masanori Kasai, Kinya Ashikaga and Toshio Ito, *Jpn. J. Appl. Phys.* **39**, 2083 (2000)

41. I. Stolichnov, A. Tagantsev, E. Colla, S. Gentil, S. Hiboux, J. Baborowski, P. Muralt and N. Setter, *J. Appl. Phys.* **88**, 2154 (2000)

42. T. K. Kundu and Joseph Ya-min Lee, *Jpn. J. Appl. Phys.* **39**, 3488 (2000)

43. Kazushi Amanuma, Sota Kobayashi, Toru Tatsumi, Yukihiko Maejima, Hiromitsu Hada, Junichi Yamada, Tohru Miwa, Hiroki Koike, Hideo Toyoshima and Takemitsu Kunio, *Jpn. J. Appl. Phys.* **39**, 2098 (2000)

44. I. Stolichnov, A. Tagantsev and N. Setter, *J. Appl. Phys.* **87**, 1925 (2000)

45. T. Friessnegg, S. Aggarwai, R. Ramesh, B. Nielsen, E. H. Poindexter and D. J. Keeble, *Appl. Phys. Lett.* **77**, 127 (2000)

46. Toyota Morimoto, Osamu Hidaka, Kouji Yamakawa, Osamu Arisumi, Hiroyuki Kanaya, Tsuyoshi Iwamoto, Yoshinori Kumura, Iwao Kunishima and Shin-ichi Tanaka, *Jpn. J. Appl. Phys.* **39**, 2110 (2000)

47. S. Aggarwai, S. R. Perusse, C. J. Kerr, R. Ramesh, D. B. Romero, J. T. Evans, Jr., L. Boyer and G. Velasquez, *Appl. Phys. Lett.* **76**, 918 (2000)

48. Wenbin Wu, K. H. Wong and C. L. Choy, *J. Vac. Sci. Tech.* **18**, 79 (2000)

49. M. W. J. Prins, K.-O Grosse-Holz, G. Müller, J.F. M. Cillessen, J. B. Giesbers, R. P. Weening and R. M. Wolf, *Appl. Phys. Lett.* **68**, 3650 (1996)

50. F. Y. Chen, Y. K. Fang, M. J. Sun, Jiann-Ruey Chen, *Appl. Phys. Lett.* **69**, 812 (1996)

Pao Yue-Kong Library
PolyU • Hong Kong

51. F. Y. Chen, Y. K. Fang, M. J. Sun, Jiann-Ruey Chen, *Appl. Phys. Lett.* **69**, 3275 (1996)

52. Jun Yu, ZhaoJian Hong, Wenli Zhou, Guangjun Cao, Jifan Xie, XingJiao Li, Shaoping Li and Zhuang Li, *Appl. Phys. Lett.* **70**, 490 (1997)

53. Nasir Abdul, Hong Koo Kim and Jean Blachere, *Appl. Phys. Lett.* **73**, 3941 (1998)

54. Y. Lin, B. R. Zhao, H. B. Peng, Z. Hao, B. Xu, Z. X. Zhao and J. S. Chen, J. *Appl. Phys.* **86**, 4467 (1999)

55. Hidki Sugiyama, Toshiyushi Kakaiso, Yuji Adachi, Minoru Noda and Masanori Okuyama, *Jpn. J. Appl. Phys.* **39**, 2131 (2000)

56. Eisuke Tokumitsu, Gen Fujii and Hiroshi Ishiwara, *Jpn. J. Appl. Phys.* **39**, 2125 (2000)

57. Sung-Min Yoon, Eisuke Tokumitsu and Hiroshi Ishiwara, *Jpn. J. Appl. Phys.* **39**, 2119 (2000)

58. W. P. Li, Y. M. Liu, R. Zhang, J. Chen, P. Cheng, X.L. Yuan, Y. G. Zhou, B. Shen, R. L. Jiang, Y. Shi, Z. G. Liu, Y. D. Zheng, *Appl. Phys. A* (2000)

59. K. Watanabe, A. J. Hartmann, J. F. Scott, *Appl. Phys. A* **70**, 243 (2000)

60. J. L. Moll and Y. Tarui, *IEEE Trans. Electron Devices* **ED-10**, 333 (1963)

61. Y. Shichi, S. Tanimoto, T. Goto, K. Kuroiwa, Y. Tarui, *Jpn. J. Appl. Phys.* **33**, 5172 (1994)

62. Gu, J. Y., Kim, K. H., Noh, T. W., and Such, K. –S., *J. Appl. Phys.* **78**, 6151 (1995)

63. V. Trtík, C. Ferrater, F. Sánchez, M. Varela, J. Fontcuberta, M. Bibes, B. Martínez,

J. Crys. Gro. **209**, 842 (2000)

64. Y. S. Leung, and K. H. Wong, *Appl. Surf. Sci.* **127-129**, 491 (1998)

65. J. Z. Sun, W. J. Gallagher, P. R. Duncombe, L. Krusin-Elbaum, R. A. Altman, A. Gupta, Yu Lu, G. Q. Gong, and Gang Xiao, *Appl. Phys. Lett.* **69,** 3266 (1996)

66. Wenbin Wu, K. H. Wong, C. L. Mak, Geoffrey Pang, C. L. Choy and Yuheng Zhang, *J. Vac. Sci. Technol. A* **18**, 2378 (2000).

67. Wenbin Wu, K. H. Wong, C. L. Choy J. Phys. D Appl. Phys. **32**, L57 (1999)

68. A. Goyal, M. Rajeswari, R. Shreekala, S. E. Lofland, S. M. Bhagat, T. Boettcher, C. Kwon, R. Ramesh and T. Venkatesan, *Appl. Phys. Lett.* **71**, 2535 (1997).

69. Zener, C., *Phys. Rev.* **82**, 403 (1951).

70. Sucharita Madhukar, S. Aggarwai, A. M. Dhote, R. Ramesh, A. Krishnan, D. Keeble, and E. Poindexter, *J. Appl. Phys.* **81**, 3543 (1997).

71. J. Lee, C. H. Choi, B. H. Park, T. W. Noh and J. K. Lee, *Appl. Phys. Lett.* **72**, 3380 (1998).

72. J. Lee, R. Ramesh, V. G. Keramidas, W. L. Warren, G. E. Pike and J. T. Evans, Jr., *Appl. Physic. Lett.* **66**, 1337 (1995).

73. Wenbin Wu, K. H. Wong, C. L. Mak, C. L. Choy and Yuheng Zhang, *J. Vac. Sci. Technol. A* **18**, 2412 (2000).

74. J. Yin, T. Zhu, Z. G. Liu and T. Yu, *Appl. Phys. Lett.* **75**, 3698 (1999)